Review article

Grain-size dependent mechanical behavior of nanocrystalline metals ☆

Eric N. Hahn, Marc A. Meyers *

University of California, San Diego, La Jolla, CA, USA

ARTICLE INFO

ABSTRACT

Grain size has a profound effect on the mechanical response of metals. Molecular dynamics continues to expand its range from a handful of atoms to grain sizes up to 50 nm, albeit commonly at strain rates generally upwards of $10^6 \, s^{-1}$. In this review we examine the most important theories of grain size dependent mechanical behavior pertaining to the nanocrystalline regime. For the sake of clarity, grain sizes d are commonly divided into three regimes: $d > 1 \, \mu m$, $1 \, \mu m < d < 100 \, nm$; and $d < 100 \, nm$. These different regimes are dominated by different mechanisms of plastic flow initiation. We focus here in the region $d < 100 \, nm$, aptly named the nanocrystalline region. An interesting and representative phenomenon at this reduced spatial scale is the inverse Hall–Petch effect observed experimentally and in MD simulations in FCC, BCC, and HCP metals. Significantly, we compare the results of molecular dynamics simulations with analytical models and mechanisms based on the contributions of Conrad and Narayan and Argon and Yip, who attribute the inverse Hall–Petch relationship to the increased contribution of grain-boundary shear as the grain size is reduced. The occurrence of twinning, more prevalent at the high strain rates enabled by shock compression, is evaluated.

© 2015 Elsevier B.V. All rights reserved.

Contents

1. Introduction

The dependence of strength on the grain size of metals has fascinated researchers since the first half of the twentieth century when Hall [1] and Petch [2] obtained the inverse dependence of grain size on strength. This subject has been treated in thousands of publications and has recently been superbly reviewed by Armstrong and Li [3,4]. However, the classic $d^{-1/2}$ relationship is an approximation which breaks down for small grains. Measurements on iron [5,6] showed in clear fashion a reduced Hall–Petch slope for grain sizes below 1 μm. Fig. 1 shows results by Abrahamson [7] and Malloy and Koch [8] for iron. There is a clear decrease in the Hall–Petch slope between 250 nm and 25 nm in the nanocrystalline regime. Consistent with this, Meyers and Ashworth [9] proposed a core-and-mantle constitutive equation that predicts a continuous decrease in slope. The grain-boundary region was assumed to have a higher flow stress (σ_{Gb}) than the grain interiors (σ_B). Thus, as the grain size increases, the fraction of grain-boundary region increases. Eq. (1) expresses the following:

$$\sigma_y = \sigma_B + 8k_{MA}(\sigma_{Gb} - \sigma_B)d^{-1/2} - 16k_{MA}^2(\sigma_{Gb} - \sigma_B)d^{-1} \qquad (1)$$

The constant k_{MA} is empirically obtained or can be extracted from finite element method calculations. Predictions from this model are shown in Fig. 1 and compared with the aforementioned experimental results. Nevertheless, the model failed to identify grain-boundary sliding or creep as critical mechanisms. It is interesting that many metals were observed to show deviation from the Hall-Petch relationship, as shown in Fig. 2 for copper, iron, nickel, and titanium. Thus, this is a general phenomenon.

Gleiter's classic work on nanocrystalline metals [10,11] was a tipping point for the global materials research community towards the exploration of ultrafine and nanocrystalline grain sizes. The breakthrough work by Chokshi et al. [12] (co-authored by H. Gleiter), reported a negative Hall–Petch slope in the nanocrystalline region for copper and palladium, and was followed by intense activity (e.g. Meyers et al. [13]). There is still considerable debate as to the soundness of the experimental data pertaining to the measurement of grain sizes and residual porosity [6,14,15], and one of the potential co-authors refused to add his name to the paper. Indeed, their specimens produced by vapor condensation followed by high-pressure compaction had residual porosity. Since the grains were increased from 6.25 nm to 15 nm by annealing, it was suggested that the reduction in porosity, and not the increase in grain size, was responsible for the increase in micro-hardness observed. Nevertheless, this paper stimulated research worldwide with some confirming and others denying the effect. With clarity and brevity, Chokshi et al. [12] attributed the effect to Coble creep, which is expressed as:

$$\dot{\gamma} = \frac{k_{CC}\Omega\mu bD_{Gb}}{kT}\left(\frac{\delta}{b}\right)\left(\frac{b}{d}\right)^3\left(\frac{\tau}{\mu}\right) \qquad (2)$$

where δ is the grain-boundary thickness, D_{Gb} is the grain-

boundary diffusion coefficient, T is the temperature, b is the Burgers vector, τ is the stress, Ω is the atomic volume, μ is the shear modulus, and d is the grain size (these symbols will be used throughout this paper). Indeed, as d increases, at a constant strain rate, so does the stress. This interpretation was later disputed since it relies on diffusion, and was replaced by a broader explanation based on grain-boundary sliding. Work by Wolf and co-workers [16] reconciled grain boundary diffusion creep and grain boundary sliding as a single deformation mechanism, that of sliding-accommodated grain boundary diffusion creep.

Nanocrystalline metals and alloys have been synthesized by a number of innovative methods [17] that include the following:

- Vapor condensation and consolidation (inert gas condensation) [10].
- Crystallization from amorphous alloys [18].
- Mechanical alloying [19].
- Severe plastic deformation (equal channel angular extrusion, high pressure torsion, cryomilling, etc.) [20,21].
- Chemical vapor deposition, physical vapor deposition, pulsed electrodeposition [22].

In this review we will highlight molecular dynamics simulations of nanocrystalline face-centered cubic (FCC), body-centered cubic (BCC), and hexagonal close-packed (HCP) metals. The number of contributions grows daily and the work done in the last decade alone is monumental. In the early 2000s, two review papers on nanocrystalline metals emphasized their unknowns, complexity, and appeal. The review by Wolf et al. [23] tackled the fundamental question of to what extent atomic simulations capture reality and, similarly, the review by Meyers et al. [13] evaluated the ability of numerous models to accurately predict
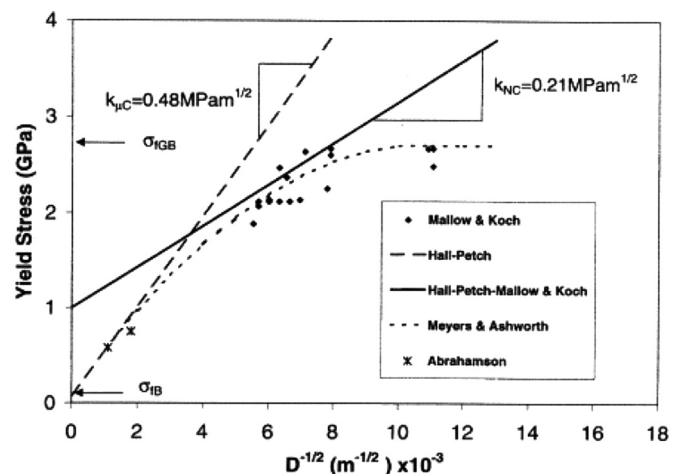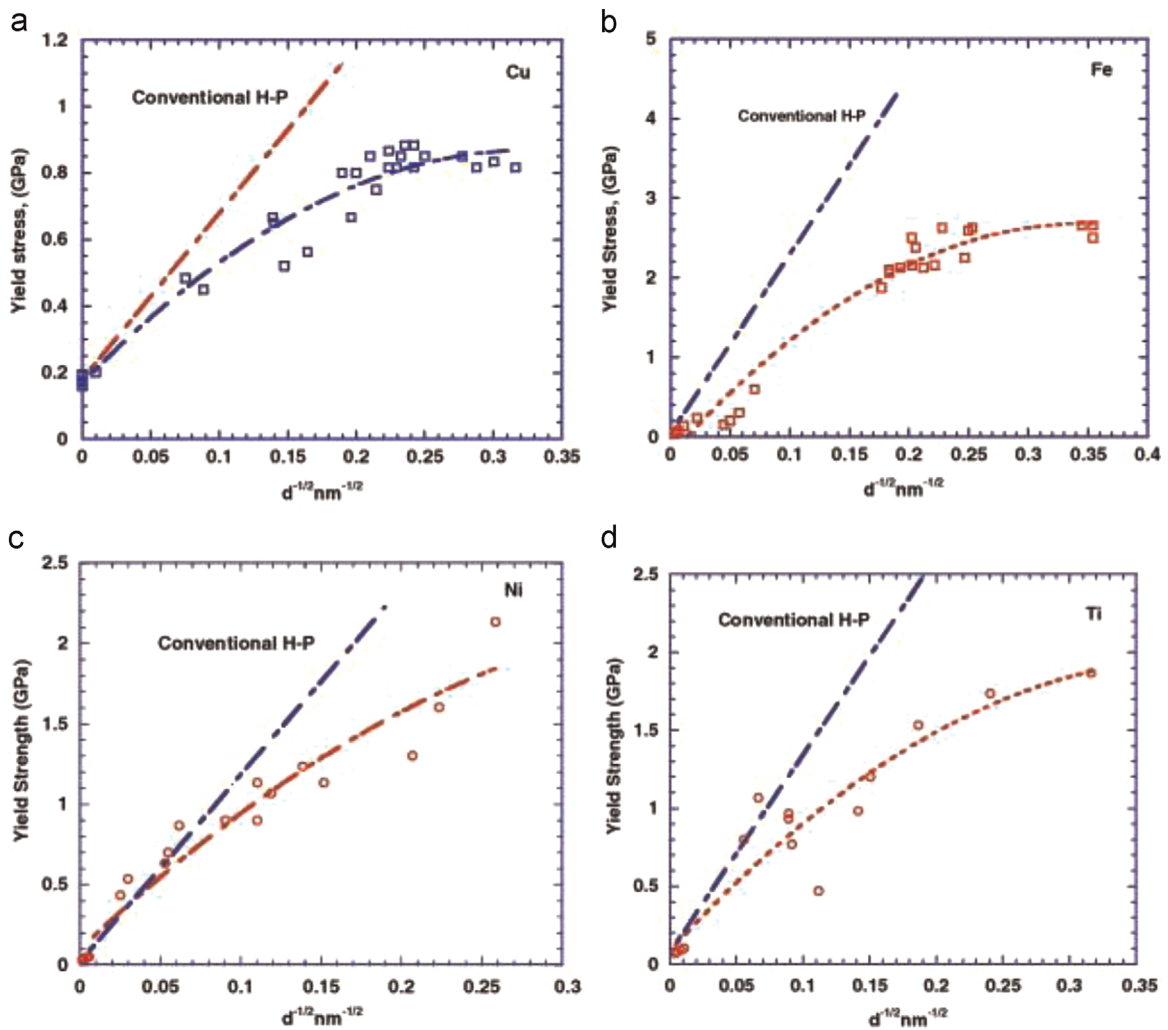

Fig. 1. Experimentally observed decrease of the Hall–Petch slope in the nanocrystalline domain and comparison with Meyers–Ashworth model [9]. Experimental results from Abrahamson [7] and Malloy and Koch [8].

Fig. 2. Plots showing the trend of yield stress with grain size for different metals as compared to the conventional Hall–Petch response: (a) copper, (b) iron, (c) nickel and (d) titanium. From Meyers et al. [13].

deformation behavior at the nanoscale. The complementary conclusions of these reviews indicate that the capacity of molecular dynamics simulations to directly visualize defects with atomic resolution provides a utility unmatched by experimental characterization, but that conclusions must be tempered by experimental results. As computation power climbs and cost plummets, it is to be expected that fundamental insights into the structure and properties of crystalline defects, as well as physical mechanisms ranging from atomic diffusion to interface migration and

grain rotation, will be made through atomic-scale simulation and modeling. Simulations deriving from atomic and quantum models extend their reach by providing valuable input criteria for multi-scale models, continuum models, and materials design [24–32] especially in iterative feedback loops [33].

In order to clarify and highlight the physical mechanisms responsible for the effects of these grain sizes, we present analytical models predicting such behavior first: Conrad and Narayan [34,35], and Argon and Yip [36]. We also discuss the equations of
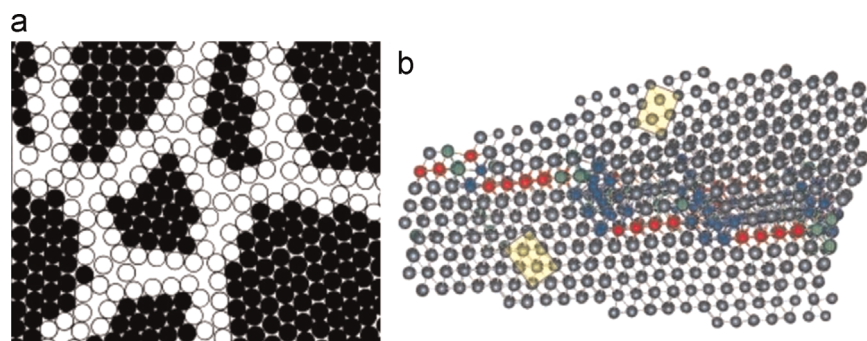
Fig. 3. (a) Model of nanostructured material showing crystals only a few nanometers or less in diameter. Boundary atoms in the two-dimensional sample are white circles (from early work of Gleiter [249]). (b) Model of grain boundary showing facets (from [250]). (For interpretation of the references to color in this figure, the reader is referred to the web version of this article.)

grain size dependent dislocations, twins, and stacking faults based on the work of Asaro and Suresh [37].

2. Physical polycrystalline models

Mechanical properties of polycrystalline metals are drastically different from those of monocrystalline metals; likewise, nanocrystalline metals behave distinctly from their large grained counterparts. Crystalline solids commonly consist of grains separated by planar interfacial defects, grain boundaries. Nanostructured materials provide us with a means to study the intrinsic nature of solid interfaces with the potential to extend structure–property relationships down to the atomic regime. Fig. 3a shows an early schematic representation of a nanocrystal in comparison with Fig. 3b, a true atomic simulation. Grain boundary atoms (indicated in white in Fig. 3a and colored atoms in Fig. 3b) divide adjacent crystals of differing orientation. Grain-boundary faceting observed in Fig. 3b is a characteristic of many interfaces. It is clear from both simulation and characterization that crystallinity extends right up to the interface and that an interface may grow or shrink during plastic deformation.

Within the last two decades it has been shown that transitions to smaller grain sizes, and thus greater grain boundary density, introduce unique mechanical deformation mechanisms. Enlargement of interfacial volume and reduction of bulk volume are responsible for causing several atomic-scale interactions, such as dislocation accumulation, to fail to manifest below a critical grain size. The volume fraction of interfaces increases to the first order as $3\delta/d$, where δ represents the interface thickness (shared by two grains) and d represents the average grain diameter. A similar relationship also exists for the volume fraction of triple junctions. Using space-filling tetrakaidecaheda, Tschopp et al. [17] produced volume fractions shown in Fig. 4, agreeing well with previous illustrations [13]. Typical interface thicknesses on the order of 2–3 atomic distances dictate that the volume fraction of grain boundary atoms is as large as 50% for 4 nm grains, 25% for 12 nm grains, 10% for 24 nm grains, and 1% for 200 nm grains. Without
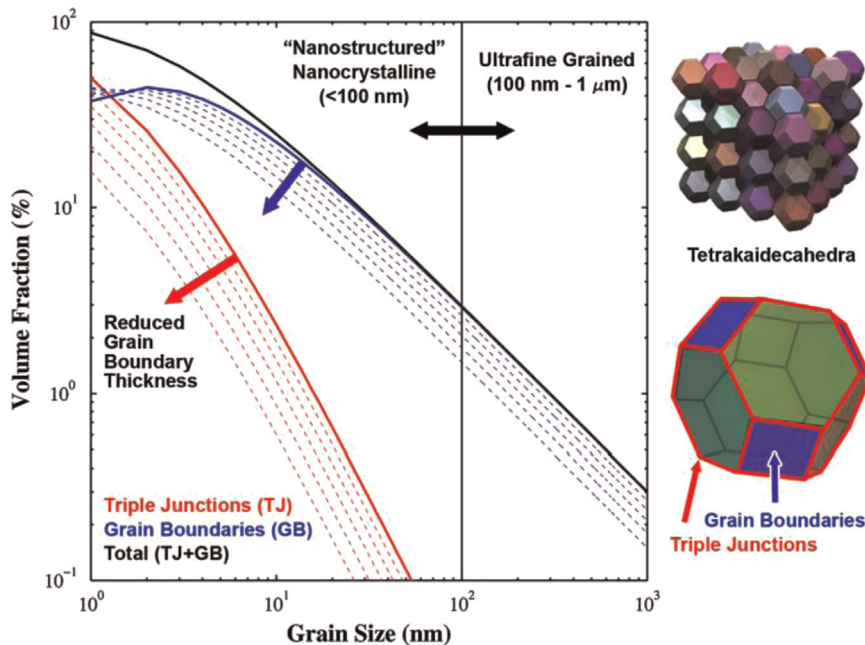

Fig. 5. The length of a simple linear chain of n dislocations as they pile up towards a fixed position x_0. The linear chain is shown in the top right where the position of the last dislocation $x_{n-1}=l$. For information on estimates refer to Szego [59] and Bilby and Entwisle [251]. Figure from Li [4].

dominating grain interior deformation, the strength of nanocrystalline metals is affected by the growing volume fraction of grain boundaries, providing a greater number of available shear/sliding points [34] and slightly increasing the effective porosity of the sample [4].

Early work by Ashby [38] approaches the problem of polycrystalline aggregates by differentiating between grain-boundary interiors and boundaries, representing polycrystals as heterogeneous materials. It is also known that grain boundaries come in a wide variety [39–45] and that many interfaces are stronger than others [46–51]. The interaction of grain boundaries with dislocations, the traditional carrier of plasticity, is of critical importance to the strength of metals [52–55].

2.1. Hall–Petch relationship

There are multiple accepted models that give rise to the classic Hall–Petch relationship. The first is dislocation pileup where an array of dislocations lies along a single slip system. Defined as

Fig. 4. The increase in the volume fraction of grain boundaries and triple junctions as a function of grain size in the nanocrystalline (< 100 nm) and ultrafine grain (100 nm to 1 μm) regimes. These plots are based on space-filling tetrakaidecahedra grains with a grain boundary thickness of 1 nm (thick line), where the dotted lines show the evolution for grain boundary thicknesses of 0.9–0.5 nm in increments of 0.1 nm. From Tschopp et al. [17].
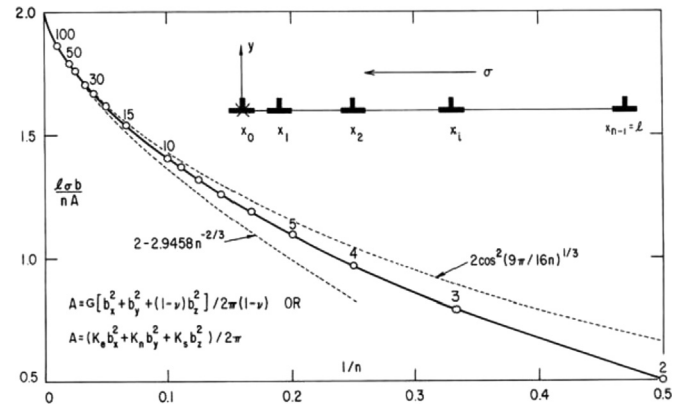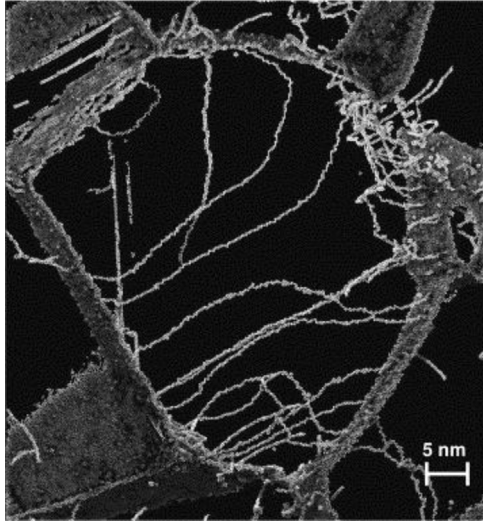
Fig. 6. A dislocation pile-up formed in a single grain. The dislocations move from top-left to bottom-right corner. A thin slice is shown and a few dislocations on nearby slip places (not part of the planar pile-up) perturb the pile-up. From Schiotz [58].

being of the same sign, the stress field resulting from a summation over all such dislocations push each toward a common grain boundary, generating a stress concentration at the "tip" of the pileup located adjacent to the grain boundary. The equilibrium positions of linear free dislocations were obtained by Eshelby et al. in 1951 [56]. Fig. 5 shows a simple pileup and estimates for relationships between the length of the pileup and dislocation density. Later, more complex arrangements of dislocations were considered by Lubarda et al. [57]. Fig. 6 demonstrates just such a complex pile-up forming in a single grain roughly 30 nm in diameter as simulated by Shiotz [58].

An upper limit to the length of the pileup is $l=2nA/\sigma b$ (refer to Sezgo [59]), where l is related to half the grain size, $d/2$. The sum of stresses at the tip, $\sigma_{tip}=n\sigma$. Taken together and assuming yielding occurs at a critical value we arrive at the classic Hall Petch relationship:

$$\sigma_y = \sigma_0 + \sqrt{\frac{4\sigma_c A}{b}}\, d^{-1/2} = \sigma_0 + kd^{-1/2},\tag{3}$$

where σ_0 is a frictional stress added as an intrinsic stress to Eq. (3) and σ_c is the critical value of σ_{tip} at which the dislocation can burst through the grain. A similar argument was made by Cottrell [60] by substituting in a locking position (which by definition must exert a balancing force) with an external force that displaces the entire pileup by a small distance δx. The force must then equal $n\sigma b\delta x$ and the stress per unit length then equals $n\sigma b$ and can be transformed into the Hall–Petch form in a similar manner as that shown above. Dislocation pileup may be a satisfactory explanation for edge dislocations, but may not hold true for screw or mixed dislocations where the tendency to cross-slip cannot be ignored. Thus a supplementary explanation is essential.

Perhaps the simplest, and more general, way of reproducing the Hall–Petch relation is through assessing grain boundaries as sources for dislocations as first considered by Li in 1963 [61]. The justification builds from the classic dislocation density dependent flow stress:

$$\sigma = \sigma_0 + \alpha G b \sqrt{\rho},\tag{4}$$

where α is a coefficient (typically on the order of $2/2\pi(1-\nu)$), G is the shear modulus, and ρ is the dislocation density. Assuming that the grain-boundary structure remains constant as grain size

decreases, the ability to emit a dislocation increases with decreasing grain size, and the density of dislocations per grain volume increases as grain volume decreases. Li [4] gives the total density of dislocations inside a given grain volume as

$$\rho = \frac{\pi d^2 m/2}{\pi d^3/6} = \frac{3m}{d}.\tag{5}$$

Here m represents the total length of dislocations emitted into each neighboring grain per unit area of grain boundary. Combining Eqs. (4) and (5) we arrive at

$$\sigma = \sigma_0 + \alpha G b \sqrt{3md^{-1}} = \sigma_0 + kd^{-1/2}.\tag{6}$$

Direct observation of dislocation emission from grain boundary ledges was reported as early as 1975 by Murr and coworkers [62], in MD simulations by van Swygenhoven in 1999 [63] and Yamakov in 2001 [64]. Numerous simulations have since shown varying degrees and parameters that affect dislocation nucleation from crystal interfaces [65,66]. The assumption that grain boundary character remains steady with increasing grain size may be valid at $d > 1$ µm, but begins to vary for nanocrystalline grain sizes. Annihilation and/or accommodation of dislocations at grain boundaries can also be expected to vary similarly with grain size.

2.2. On the exponent in the Hall–Petch relationship

Substantial deviations observed in the Hall–Petch relationship actually suggest that other relationships are prevalent. In 1956, Baldwin [67] found that in many cases the exponent -1 or $-1/3$ provided as good a fit as $-1/2$. More recent analyses, such as the one by Dunstan and Bushby [68], point to the same. Consistent with the results of Fig. 1, which show a reduction of the prefactor from 0.48 to 0.21 MPa m$^{1/2}$, Durstan and Bushby [68] report a decrease from 0.52 to 0.054–0.14 MPa m$^{1/2}$ for the nanocrystalline domain, in iron. A more general manner to plot grain size dependent strength data is in a double logarithmic form:

$$-m = \frac{\log\frac{\sigma}{\sigma_1}}{\log\frac{d}{d_1}}.\tag{7}$$

where σ_1 and d_1 are reference points on plot and m is the slope of the linear fit. Adding a frictional stress expressing the resistance of the lattice in a single crystal:

$$\sigma = \sigma_0 + \frac{\sigma_1}{d_1^{-m}} d^{-m}.\tag{8}$$

The value of m can thus be obtained independently. However, the connection of the Hall–Petch equation to the hypothesis of grain-boundary (edge) dislocation pile-ups is historically of such import that the ½ exponent is indelibly connected to the fabric of materials science. For a more detailed analysis, the reader is referred to Meyers and Chawla [69]. Interestingly, Durstan and Bushby [68] draw inspiration from the thickness-dependent strength of thin films in which the stress may be dependent as log (d)/d which introduces an apex in strength associated with an inversion of the Hall–Petch slope.

As mentioned previously, the effect of porosity, especially at grain boundaries, cannot be ignored. Porosity may arise in the form of residual porosity from fabrication methods or may be intrinsic to smaller grain sizes due to excess volume of grain boundary atoms. Excess volume has been shown to affect plasticity occurring at grain boundaries [70], especially relating to the ability to nucleate dislocations [71]. Simulations have placed excess volumes between 1–5% for special grain boundaries and as high as 80% for disordered grain boundaries [50]. Experimental measurements place excess volume near 10% [72,73]. This suggests

that grains in the nanometer regime will have at least 1% porosity for 25 nm grains and 5% effective porosity for 5 nm grains. It has also been shown that elastic modulus decreases with increasing porosity [13,74]. Li [4,75] related impurity content of the grain boundary (theorizing that impurities stabilize ledges) to porosity on the basis that equilibrium segregation decreases with increasing porosity by decreasing internal stresses. Li's equation incorporating impurity segregation and effective porosity is

$$\sigma = \sigma_0 + A\sqrt{\frac{x - (\phi - \phi_0)}{d/3KN_{\beta b}}}. \tag{9}$$

A is a fitting constant akin to the Hall–Petch slope, x is a fraction of possible impurity sites occupied (this term is grain size dependent and defined as $0 < x < 1$), K is the equilibrium constant, and $N_{\beta b}$ is a concentration of impurities per unit of grain boundary, ϕ is porosity and ϕ_0 is equilibrium porosity. For $\phi_0 = \phi$, and x approaching zero for small grain sizes, a Hall–Petch type plot will decrease in slope before plateauing in strength. This type of effect has clear experimental evidence as discussed earlier and shown in FigS. 1 and 2.

Using static values of excess porosity Li [4,75] demonstrated a turnover in strength below critical grain sizes. Carlton and Ferreira [76] produce a similar relationship including a term incorporating increased dislocation adsorption for small grain sizes. Both models imply that dislocations remain the primary carrier of plasticity down to the smallest grain sizes. Many studies indicate that dislocations continue to play an important role in small grain sizes such as strain hardening in 20 nm Ni [77] and that dislocation-mediated grain boundary rotation occurs at smaller grain sizes [78]. The former is an example of traditional intragranular plasticity while the latter is a primary example of deformation originating from intergranular sources and alternative deformation mechanisms at a reduced size.

2.3. Inverse Hall–Petch Models

The "negative" or "inverse" trend in yield strength behavior with decreasing grain size results from a scale-determined interruption of dislocation phenomenon associated with the traditional explanation for the Hall–Petch phenomenon; as grain size is reduced, the number of dislocations associated with a given grain and its boundaries is reduced and the summative contribution to the stress field is diminished. Yet, although the stress field associated with a single grain is diminished, the influence of stress fields emanating across neighboring grains provides sufficient motivation for relaxation of grain boundaries and triple junctions by grain boundary sliding [79]. A compilation of yield stress data taken by Meyers et al. [13] for FCC Cu indicates that the critical grain diameter for this transition in deformation mechanism is right under 20 nm (Fig. 7).

As mentioned earlier, the first experimental evidence of the inverse Hall–Petch response in the nanocrystalline regime was by Chokshi et al. [12] when it was reported that a negative Hall–Petch slope was observed for nanocrystalline copper (FCC) and palladium (FCC).

Conrad and Narayan [34,35], and Conrad [80] developed a model based on independent atomic shear events and related the shear rate at grain boundaries to the global strain rate. They obtained the following equation:

$$\dot{\gamma} = \frac{2\delta\nu_D}{d}\sinh\left(\frac{\nu_D\tau_e}{kT}\right)\exp\left(-\frac{\Delta G_0}{kT}\right), \tag{10}$$

where δ is the grain boundary width, taken as 3b, and $\tau_e = \tau - \tau_{cr}$. The term $\frac{2\delta\nu_D}{d}$ represents the volume of a grain boundary and the area it sweeps over during shear.

Alternatively, the shear stress τ is expressed as

$$\tau = \tau_0 + \left[\frac{kT}{V}\ln\left(\frac{\delta\nu_D}{\dot{\gamma}}\right) + \frac{\Delta F}{V}\right] + \frac{kT}{V}\ln d \tag{11}$$

The symbols not previously defined are V, the activation volume; ΔF, the Helmholtz free energy; ν_D, the vibrational frequency of an atom (Debye frequency, $\sim 10^{13}$ s^{-1}, a first order approximation can be taken as the time taken for sound waves to travel one interatomic distance), and τ_0, a frictional stress. Fig. 8a shows the prediction from the Conrad–Narayan equation together with experimental results for copper. The transition from positive to inverse HP relationship is clear and the line, which is from Eq. (11),
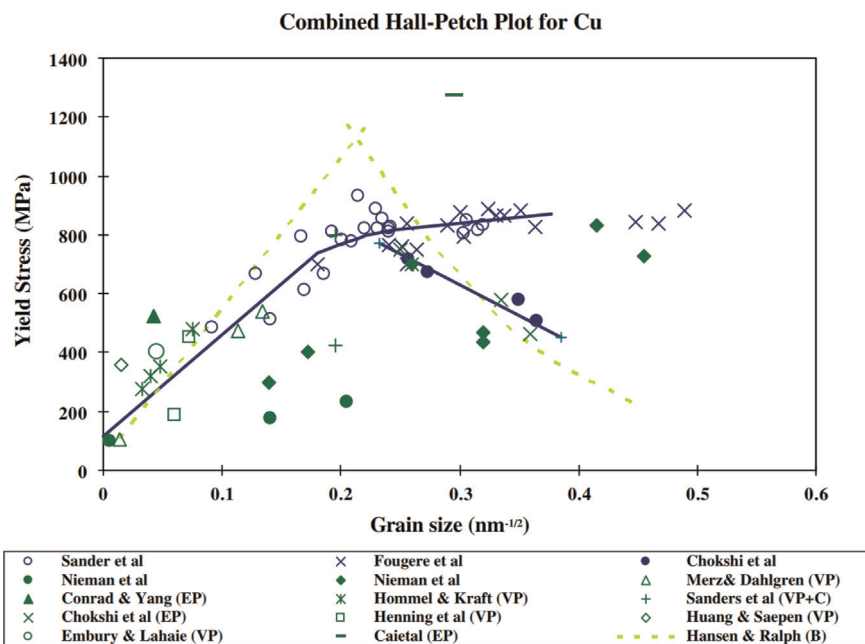

Combined Hall-Petch Plot for Cu

|					
○	Sander et al	×	Fougere et al	●	Chokshi et al
●	Nieman et al	◆	Nieman et al	△	Merz& Dahlgren (VP)
▲	Conrad & Yang (EP)	✳	Hommel & Kraft (VP)	+	Sanders et al (VP+C)
×	Chokshi et al (EP)	□	Henning et al (VP)	◇	Huang & Saepen (VP)
○	Embury & Lahaie (VP)	—	Caietal (EP)	- - -	Hansen & Ralph (B)

Fig. 7. Compilation of yield stress as a function of grain size (plotted by $d^{-1/2}$) for Cu. The plot illustrates the Hall–Petch relationship for larger grain sizes and the ambiguity near $d = 25$ nm ($d^{-1/2} = 0.2$) where some results show a plateau in strength and other results show a decrease indicative of the inverse Hall–Petch relationship [13].

a

b
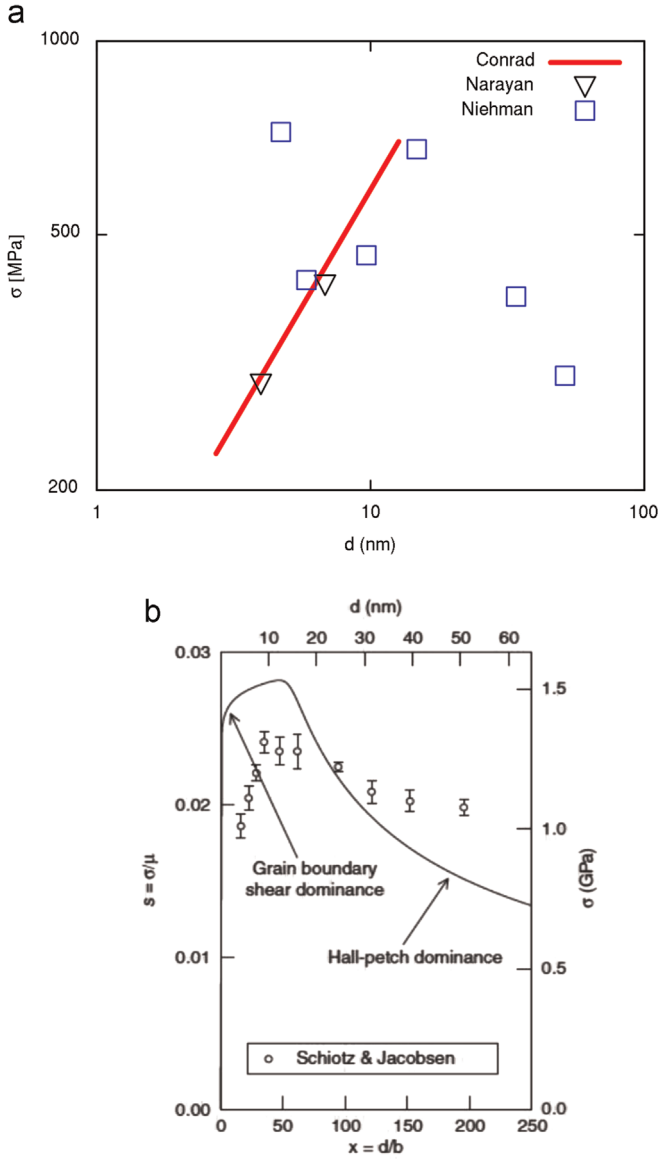
Fig. 8. (a) Experimental points for copper and Conrad-Narayan equation [34,35] applied to the inverse Hall–Petch region; data and plot adapted from Conrad [80]. (b) Comparison of analytical model by Argon and Yip [36] to the molecular dynamics simulations of a maximum in the strength of Cu by Schiotz and Jacobsen [82]. Normalized stress $s = \sigma/\mu$ and grain size $x = d/b$ are used in plot.

tracks the results well.

The Argon and Yip [36] model considers grain-boundary shear and dislocation plasticity as two operating mechanisms, each one in proportion to the volume fraction of material where they operate. The expression for grain-boundary shear is similar to the one by Conrad and Narayan [34] and the one for dislocation plasticity comes from thermally-activated dislocation motion. The activation energy for plastic flow in the boundary, Q_v, is taken as that for an amorphous phase, since the grain boundary is considered, to a very first approximation, as amorphous. Thus

$$\dot{\gamma}_{Gb} = \gamma_T \nu_D \exp\left[-\frac{Q_v}{kT}\left(1 - \frac{\tau}{\tau_{iGb}} \right) \right],$$

(12)

where γ_T is a transformation shear strain, and τ_{igb} is the ideal shear strength of the grain boundary, which they take to be equal to one half of that of the lattice. Correspondingly, the thermally-activated constitutive equation for dislocation slip, with some adjustments, takes the form:

$$\dot{\gamma}_D = \frac{b}{d} \nu_d \exp\left[-\frac{\Delta G_0}{kT}\left(1 - \frac{\tau}{\tau_0} \right) \right],$$

(13)

where τ_0 is the height of the barriers, ν_d is the dislocation vibration frequency, ΔG_0 is the energy of the barriers at 0 K, b is the Burgers vector. The vibrational frequency of a dislocation is related to its length by $\nu_d = \nu_D b/l$ and, while lengthy derivations exist, Kubin [81] offers a concise derivation within the framework of dislocation dynamics simulations. Typical values of dislocation vibration frequencies are on the order of 10^9 s^{-1}. As a dislocation length becomes confined to smaller and smaller grain sizes its vibrational frequency will increase. For 25 nm grains ν_d may be as large as 10^{11} s^{-1}.

This is the simplest form of the Seeger equation, assuming rectangular-shaped barriers. The b/d term adds a grain-size dependence and is related to the emission of dislocations at boundaries, their crossing of the entire grain, and being annihilated at the opposite boundary, generating a strain of b/d each. It is, indeed, a tortuous way to introduce a grain-size dependence. The exponential terms are replaced by more tractable power terms:

$$\dot{\gamma}_{Gb} = \gamma_T \nu_D \left(\frac{\tau}{\tau_{iGb}} \right)^m$$

(14)

$$\dot{\gamma}_D = \frac{b}{d} \nu_d \left(\frac{\tau}{\tau_0} \right)^n$$

(15)

The volume fraction of grain-boundary is approximated as, assuming spherical grains of radius, R:

$$V_f = \frac{4\pi R^2 \delta}{\frac{4}{3}\pi R^3} = \frac{3\delta}{R} = \frac{6\delta}{d}$$

(16)

The total strain rate is expressed as

$$\dot{\gamma} = \left(\frac{6\delta}{d} \right)\dot{\gamma}_{Gb} + \left(1 - \frac{6\delta}{d} \right)\dot{\gamma}_D,$$

(17)

where m and n are fitting parameters.

Combining Eqs. (14)–(17) yields an expression that relates the stress τ to the grain size d at a constant strain rate, $\dot{\gamma}$. This is shown in Fig. 8b, in comparison with MD results by Schiotz and Jacobsen [82]. We note that the volume fraction of grain boundaries is in fact closer to $3\delta/d$ bearing in mind that each grain boundary is shared by two grains and $6\delta/d$ is double counting. The resulting generalized equation is

$$\dot{\gamma} = \left(\frac{3\delta}{d} \right)\dot{\gamma}_{Gb} + \left(1 - \frac{3\delta}{d} \right)\dot{\gamma}_D$$

(18)

A number of analyses have been proposed in the literature but the two above capture the important physical phenomena and describe, quantitatively, the response in the nanocrystalline range. It is important to emphasize that the inverse Hall–Petch relationship requires grain sizes lower than 30 nm. This is indeed in the lower part of the nanocrystalline domain, corresponding to a fraction of grain-boundary atoms of ~20%.

2.4. Special dislocation configurations in nanocrystalline metals

Asaro and Suresh [37] made strides in the description of grain size dependent effects on the emission of defects from grain boundaries. Nucleation of dislocations from pre-existing grain boundary dislocations, partial dislocations, and deformation twins were analytically represented and the increased partial separation in the nanocrystalline domain was explained. The reduction of the activation volume in FCC metals from $\sim10^2 b^3$ to $\sim b^3$ was
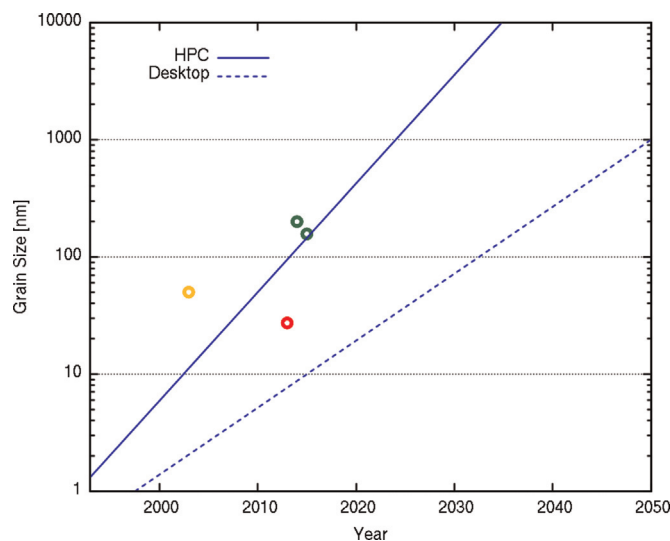
Fig. 9. Future projection of computational power of the Moore's Law type to achievable grain sizes for atomistic simulation by an empirical potential. The solid line is representative of high performance computers and is based on projections of the TOP500 List using the LINPAC benchmark. Dashed line is representative of desktop computers based on projections based on NVidia graphics cards. These lines represent simulation capability of 5 times the grain diameter in each dimension. Green circles are representative of runs completed at US National Labs [252,253], the yellow circle by one of the first systematic studies of 5–50 nm grains [82], and the red circle is a systematic study of grain sizes smaller than 27.3 nm [166] (For interpretation of the references to color in this figure legend, the reader is referred to the web version of this article.)

Fig. 10. Increasing single CPU cost of running many-body potentials in seconds per atom per time step as a function of year. The black line is indicative of computational cost doubling of the Moore's Law type similar to Fig. 3 [116] (LAMMPS molecular dynamics package, http://lammps.sandia.gov; Potential benchmarks, http://lammps.sandia.gov/bench.html#potentials.). EAM, embedded-atom method; MEAM, modified embedded-atom method; REBO, reactive empirical bond order; BOP, bond-order potential; AIREBO, adaptive intermolecular REBO; ReaxFF, reactive force field; COMB, charge optimized many-body; GAP, Gaussian approximation potential.

explained in terms of the shorter mean free path of dislocations and less interaction among them. This was also done by Jarmakani et al. [83].
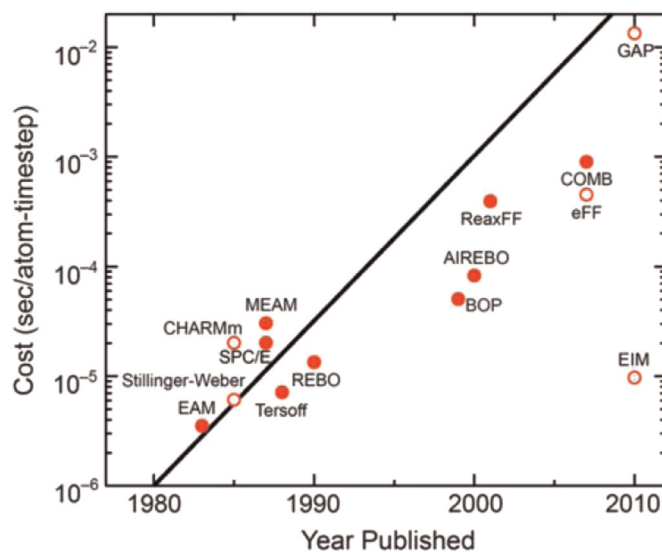
3. Molecular dynamics fundamentals

The review by Farkas [84] emphasizes that, in spite of a large gap in achievable time scales, atomistic modeling continues to serve as a unique tool for direct visualization of defects that influence microstructural evolution. This has been rendered more realistic by the continued advance, at an impressive rate, of computational power and our ability to characterize complex simulations. Spanning between 2005-2015, the power of our personal computers has reached what was capable by supercomputers 15 years earlier. The ability of high-performance computing has been demonstrated with trillion-atom molecular dynamics simulations using a simple pairwise Lennard–Jones form in 2008 [85] and billion atom simulations of many-body potentials in 2012 [86]. Approximately 10^9 atoms form, in tridimensional space, a simulation box with lateral dimensions of 10^3 atoms, approximately 200 nm. Taking a few standardized variables, such as a femtosecond timestep and nanosecond simulation time, grain sizes as large as ~50 nm can be simulated, limited largely by the number of grains in each dimension required to ensure a good measure of polycrystallinity. The current and projected capabilities of personal and high performance computers are shown in Fig. 9 using projections derived from the Top500 list for high performance computing (HPC) and NVidia graphics cards for desktop computers. The equations relating grain size to year are

$$d_{HPC} = 1.32e^{(0.214(y-1993))} \tag{19}$$

$$d_{desk} = 0.55e^{(0.132(y-1993))}. \tag{20}$$

placing the micrometer (or microsecond) regime between 2025 and 2050 respectively. Fig. 10 shows the implementation of

increasingly accurate interatomic potentials, illustrating that the desire to extend molecular dynamics to increasing length and time scales is tempered by the reality and complexity of metallic systems. Increasing complexity is also seen for analysis and visualization techniques that are presented in the following section. Another drive for realistic systems and larger number of atoms requires multiple element types, representing a push towards incorporating alloying elements as well as impurities that can strengthen or weaken grain boundaries as shown in Fig. 11.

Essentially, a key piece to furthering our understanding of phenomena in nanostructured materials is the ability to precisely observe how emission, transmission, absorption, rearrangement, accommodation, and storage of dislocations and other defects occur at grain boundaries of different dense crystal systems. It will be interesting here to compare critical grain size across various FCC, BCC, and HCP metals. Also of interest is how varying degrees of misorientation and grain size alter inter- and trans-granular dislocation interactions.

3.1. Molecular dynamics foundations

Even though molecular dynamics (MD) methods, both in their physics and numerical implementations, are complex and fascinating areas of study on their own, it is not the intention of this review to enumerate physics of MD methodology or the numerical algorithms used to implement the physical framework. It is likely that this review will fall into the hands of those already acquainted in the field of molecular dynamics simulations as well as in the hands of those interested in learning state of the art of materials science, namely the study of metallic imperfections through molecular dynamics simulations. For the latter readers, a brief overview of the available introductory literature is presented.

Although mainly oriented to the study of liquids, the early contribution by Allen and Tildesley [87] is not only a good introductory text for molecular dynamics researchers, but also a must-have reference for specialists since it covers both the physics and numerical basics of the method. The later contribution by
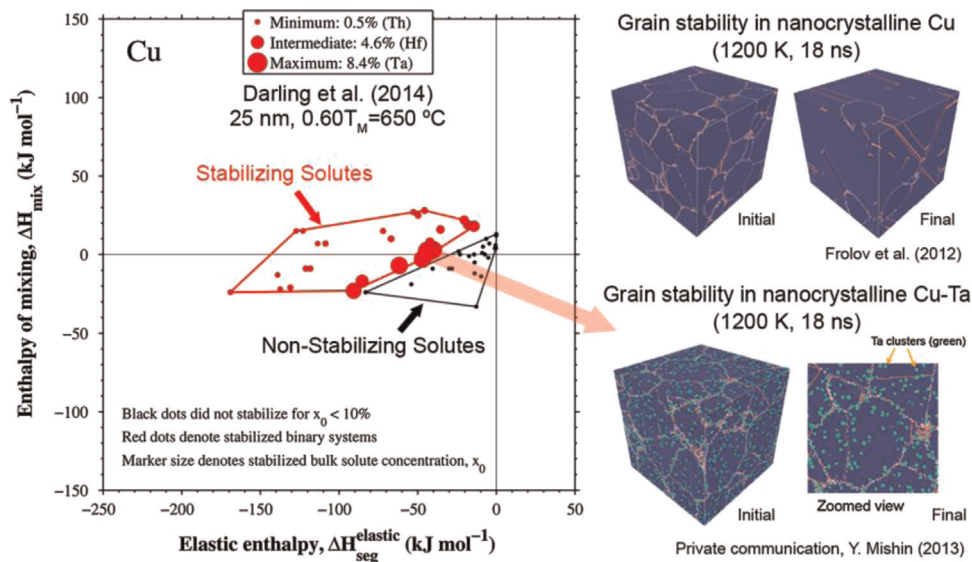
Fig. 11. (left) Thermodynamic stability map for stabilizing nanocrystalline copper at $0.6T_m$; the red and black dots indicate the stabilizing and nonstabilizing solutes with respect to the elastic enthalpy and enthalpy of mixing. (right) Molecular dynamics simulations at 1200 K indicate that nanocrystalline Cu rapidly coarsens [254] while Ta precipitates in the Cu–5%Ta sample stabilize the surrounding nanocrystalline grain size. From Tschopp [17].

Rapaport [88] extensively covers the practical applications of the method and tools available towards undertaking simulations.

The focus of this review is on the mechanical behavior of nanocrystalline metals, which is directly related to the evolution of pre-existing defects and those arising from imposed loading on the material. The fundamentals of defects in solids are very well covered in classic books on the matter [89,90] and the computer simulation of dislocations and other defects is a topic treated in an number of influential papers [91,92]. Fortunately, the book by Bulatov and Cai [93] gathers many important methods into a single text.

Non-trivially, the implementation of broadly applicable community codes for materials modeling and simulation has been a boon to the success of atomistic computational modeling as highlighted by a recent opinion article on community codes by

Plimpton and Gale [94] based on the well-received LAMMPS code developed in 1995 by Plimpton [95].

Finally, a number of techniques have surfaced over the years for simulating and evaluating nanostructured materials. A constant quest to scale up the number and diameter of grains as well as our ability to accurately model them through interatomic potentials has stimulated research in this area of computational materials science. Computational advances have principally thrust molecular dynamics simulations to growing level of importance.

3.2. Defect identification methods for crystalline materials.

As continuously enumerated, defects play a unique role in materials phenomena and, therefore, their proper identification is
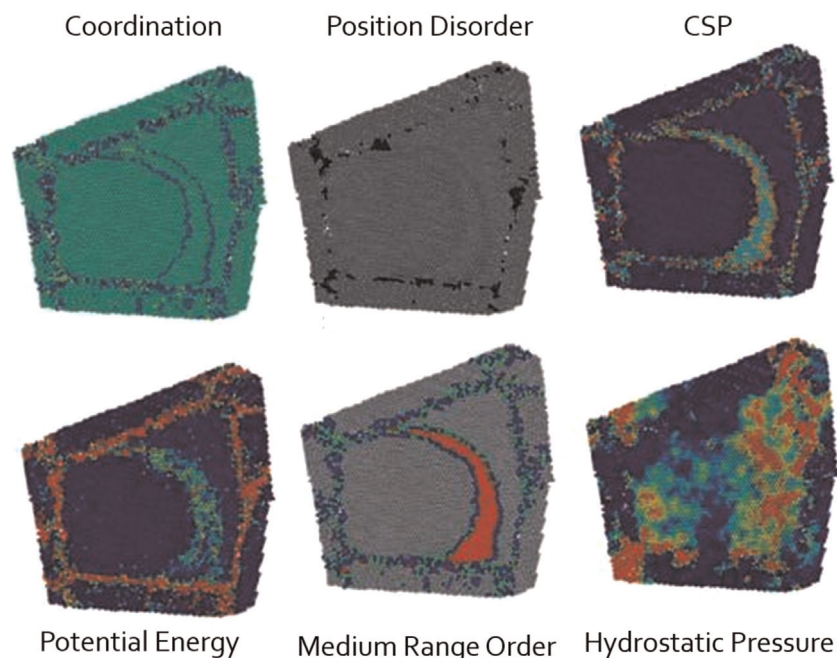
Fig. 12. Visualization of a dislocation traversing a nanocrystalline grain by six different analysis coloring schemes. From Swygenhoven [92].

a fundamental molecular dynamics tool for developing an in-depth understanding of material behavior.

The recovery of crystal defects from the complete simulation domain often involves time consuming post-processing steps that may surpass the time employed during the simulation itself. Post-processing is often unavoidable for proper interpretation of simulation results and the importance of appropriate selection tools can be shown by the different methods of evaluating the same timestep as seen in Fig. 12. Improved computational analysis methods provide greater insight into atomic level processes and inform coupling of atomistic to mesoscale simulations [96].

Here we present a succinct overview of the defect identification methods based on structural analyses that are currently used in MD studies; their appearance in this section is based on their computational cost factor, considering the first as the least expensive.

3.2.1. Centro-symmetry parameter

The centro-symmetry deviation parameter, commonly named the centrosymmetry parameter (CSP), is a robust method that relies on a characteristic that is common to simple cubic (SC), FCC and BCC structures: every atom is a center of inversion symmetry, which means that taking an atom as a center, its neighboring atoms are (centro)symmetric relative to it. This property can be used to distinguish these atoms from other structures when the local bond symmetry is not verified or it deviates from an established value.

This metric for structural identification was developed by Kelchner et al. [97] in equation form and practical applications can be found in several references [93,98].

$$CSP = \sum_{i=1}^{N/2} \left| \vec{R}_i + \vec{R}_{i+N/2} \right|^2 \tag{21}$$

Here the N nearest neighbors, specified as an input parameter, of each atom are identified such that $\vec{R}_i$ and $\vec{R}_{i+N/2}$ are the vectors from the central atom to a given pair of opposing neighbor atoms. Opposite pairs of atoms for FCC, BCC, and HCP are indicated in Fig. 13 by atoms of the same color. For an atom sitting on an expected lattice point the CSP determined by this sum will be zero. Thermal vibrations will not cause much fluctuation from 0, but defects that break symmetry will produce a larger (positive) CSP value. Fig. 14 shows a schematic representation of a central atom in FCC surrounded by 12 closest neighbors. They are diametrically opposed in pairs. Note that BCC structures have 8 neighbors (though the second shell is often considered totaling 14) and SC have 4. We would like to highlight some characteristics of CSP:

- As seen in its definition, the CSP parameter is just a scalar quantity and therefore, its applicability to oriented defective structures is limited.
- The parameter is not suitable for treatment of HCP, diamond cubic (DC) and some other structures that do not have the symmetrical characteristic described before.
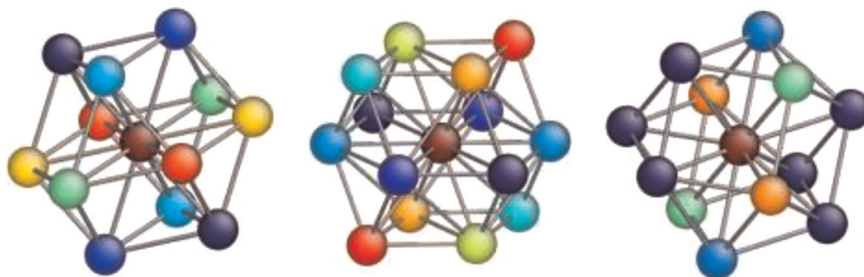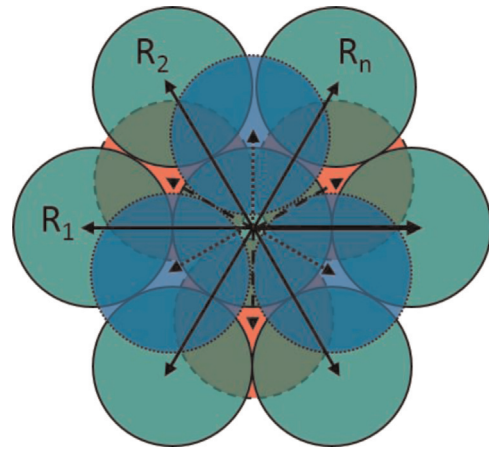

Fig. 14. ABC sequence of FCC {111} planes. 12 nearest neighbor atoms surrounding a center atom, with the 3 dashed atoms belonging in plane A (red), the 7 atoms belong in plane B (green) and the last 3 dotted atoms belong in plane C (blue).

- The identification of defects with this method is affected by elevated temperatures, as shown by Stukowski [99].

3.2.2. Common neighbor analysis (CNA) and parameter (CNP)

Albeit a higher computational cost compared to CSP, structure analysis algorithms that employ high-dimensional signatures to characterize atom arrangements are usually more efficient to discern between structures. The Common Neighbor Analysis (CNA) is one of these methods. Proposed by Honeycutt and Andersen [100] and later further developed by Faken and Jonsson [101] and Tsuzuki, Brancio, and Rino [102], the CNA computes a characteristic signature from the topology of bonds that connect an atom to its surrounding neighbors.

The neighborhood of an atom is defined by a cutoff distance so that all the atoms within that distance are said to be neighbors. Each neighbor is taken into account for in the calculation of three characteristic numbers that are computed, yielding a triplet that, when compared with a set of reference signatures, allows for the establishment of a structural type to the atom whose triplet is evaluated.

Unlike CSP, CNA can be used on non-centro-symmetrical structures such as HCP crystals. The latter are centrosymmetric only if the c/a ratio is ideal, 1.633 (the metal that comes closest to ideal HCP is magnesium). To see how one of the triplets is computed, a representative Common Neighborhood Parameter (CNP) can be defined as:

$$Q_i = \frac{1}{n_i} \sum_{j=1}^{n_i} \left| \sum_{k=1}^{n_{ij}} \left(R_{ik} + R_{jk} \right) \right|^2 \tag{22}$$

The index j evaluates the n_i nearest neighbors of atom i, and the

Fig. 13. Centro-Symmetry Parameter (CSP) distinguishes between plastically deformed regions of dislocations and stacking faults (asymmetry) from purely elastically deformed regions (which would have symmetry). Pairs of atoms diametrically opposed from a central atom are identified by the same color; (a) FCC, 6 pairs; (b) BCC, 7 pairs; (c) HCP, 6 pairs [102].
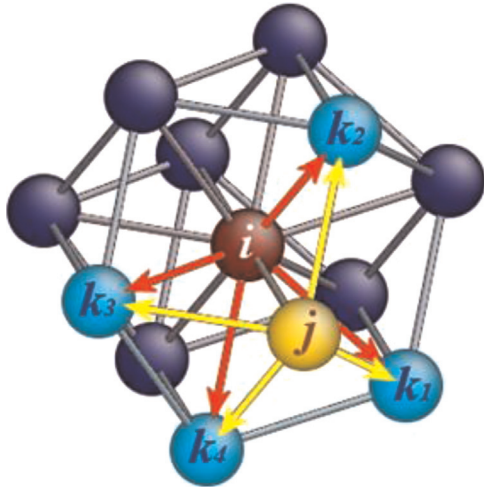
Fig. 17. Orientation imaging map using Euler angles as proposed by Rudd [109].

Fig. 15. Common Neighbor Analysis (CNA) provides a measure of degree of crystallinity and identification of crystal structures present. Analysis is derived based on the number of common neighbors (k) shared by an atom pair (i-j):k_1, k_2, k_3, and k_4[102].

index k evaluates n_{ij} common nearest neighbors of atom i and atom j. This is visually represented in Fig. 15 where k atoms are common neighbors to atom i and atom j.
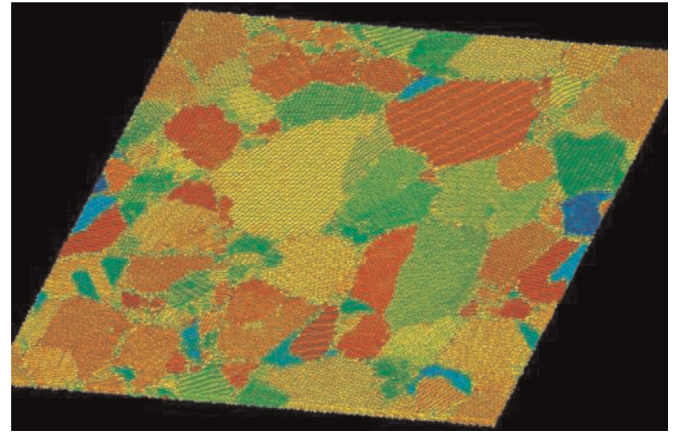
The Adaptive Common Neighbor Analysis (a-CNA), recently proposed by Stukowski [99] takes CNA as a basis, and is particularly suitable for multi-phase systems, adapting the cutoff distance of the standard CNA to each individual atom depending on a reference structure for comparison purposes. The reader is referred to the cited article for a thorough explanation and example of the methodology. We note that similar structures may not be adequately identified with respect to one another by methods utilizing characteristic signatures.

3.2.3. Bond angle analysis

Developed by Ackland and Jones [103] and with a computational cost in the order of the CNA, this method is able to distinguish FCC, BCC, and HCP structures effectively. The authors have made important efforts in showing the efficiency of this method for treatment of HCP structures and its comparison with the application of CNA to HCP structures is worth reading.

3.2.4. Dislocation extraction algorithm (DXA)

Detection of defects from crystalline structures is valuable, but the current state of the art is the distinction of one defect from another. Two new tools by have been developed by Stukowski [99,104,105]. The 'sharpness' of dislocations is seen in Fig. 16 in contrast with the CNA filtering. This enables a better determination of dislocation densities, since no dislocations are missed by superposition as shown by Ruestes et al. [106]. The voids from which these dislocations emanate are visible in DXA but cannot be distinguished by CNA.

3.2.5. Orientation imaging map (OIM)

Typical materials exhibit some degree of texture (non-random grain orientation distribution) imparted by processing or past deformation. Twinning is one such deformation mechanism that can impart texture by preferentially adjusting the orientation in soft grains.

The first integration of an orientation imaging map to atomistic simulations was accomplished by Rudd [107] and can be seen in Fig. 17. Ravelo et al. [108] also demonstrate an OIM mapping function in the application of the SPaSM code. The foundation of the method lies in a centro-symmetry-like formulation where nearest neighbors are located for each atom and is summarized below for the case of BCC structures:

(i) Find nearest 8 neighbors for each BCC atom and create opposing pairs to form the family of $<111>$ directions.
(ii) Take cross products, $\hat{e}_{0\bar{2}2} = \hat{e}_{111} \times \hat{e}_{\bar{1}11}/\left|\hat{e}_{111} \times \hat{e}_{\bar{1}11}\right|$ and $\hat{e}_{\bar{4}22} = \hat{e}_{0\bar{2}2} \times \hat{e}_{111}/|\hat{e}_{0\bar{2}2} \times \hat{e}_{111}|$.
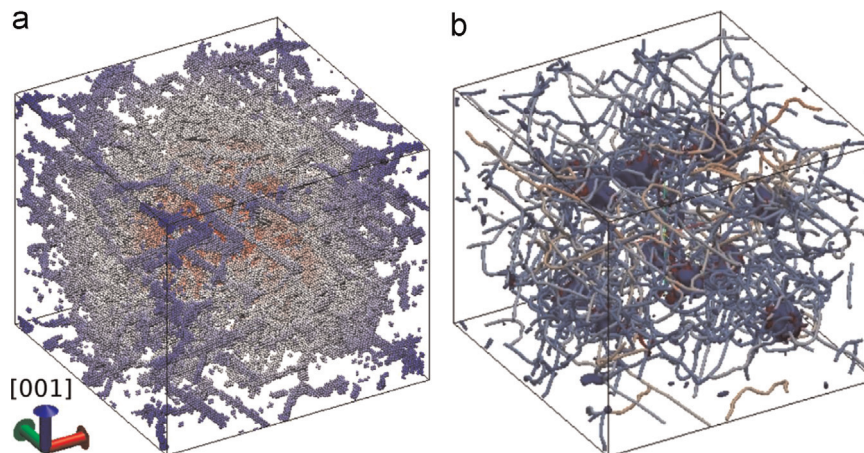
Fig. 16. Comparison of (a) a conventional atomistic visualization using CNA filtering in tantalum and (b) a geometric line visualization of the dislocations provided by the DXA. In addition to extracting the dislocation line network, the DXA analysis also produces a geometric representation of non-dislocation defects, such as void surfaces, visible in the center of box [106].
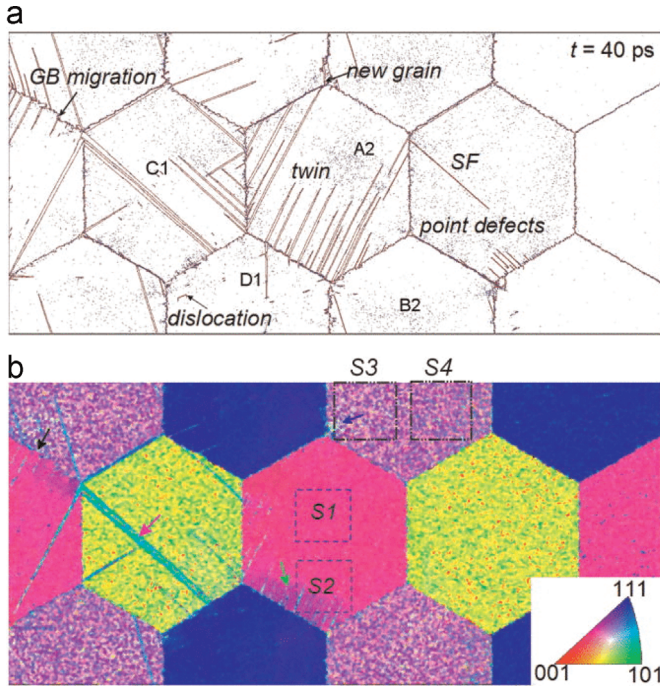
Fig. 18. Deformation of hexagonal nanocrystalline Al during shock compression (t=40 ps) showing various defects, and (b) the corresponding orientation map [110].

(iii) Three $<100>$ directions can be found by $\hat{e}_{100} = \frac{1}{\sqrt{3}}\hat{e}_{111} - \frac{2}{\sqrt{6}}\hat{e}_{\bar{4}22}$, $\hat{e}_{010} = \frac{1}{\sqrt{3}}\hat{e}_{111} - \frac{1}{\sqrt{2}}\hat{e}_{0\bar{2}2} + \frac{1}{\sqrt{6}}\hat{e}_{\bar{4}22}$, and and comprise a rotation matrix, R.

(iv) Accounting for symmetry, the Euler angles, $z(\varphi)$, $y(\theta)$, and $z(\psi)$ are then found by $\theta = cos^{-1}(R_{33})$; if $\theta = 0$, $\varphi = cos^{-1}(R_{11})$ and $\psi = 0$; if $\theta \neq 0$, $\varphi = sin^{-1}(R_{31}/sin\theta)$, and $\psi = sin^{-1}(R_{13}/sin\theta)$

(v) Quaternions can be determined as follows:

$$q_0 = cos\left(\frac{\theta}{2}\right)cos(\frac{\varphi + \psi}{2})$$

$$q_1 = sin\left(\frac{\theta}{2}\right)cos(\frac{\varphi - \psi}{2})$$

$$q_2 = sin\left(\frac{\theta}{2}\right)sin(\frac{\varphi - \psi}{2})$$

$$q_3 = cos\left(\frac{\theta}{2}\right)sin\left(\frac{\varphi + \psi}{2}\right)$$

(vi) The spatial components of the quaternion vector (q_1, q_2, q_3) can be intensity mapped to RGB color values in the normal way.

(vii) Rudd [109] offers an alternate color mapping function of the form: $[(\frac{1}{\sqrt{3}})sin\,\psi + \frac{1}{2}]\hat{n}_{111}$.

Wang et al. [110] also developed a methodology akin to electron backscattered diffraction in order to evaluate crystallographic orientation of neighboring grains. Fig. 18 shows a range of defects generated upon subjecting an ideal nanocrystalline metal (with identical hexagonal grains) to external tractions. Four different phenomena are observed: dislocations, stacking faults, twins, and grain-boundary migration. A new grain is being formed at a triple junction. The stacking faults and perfect dislocations are emitted from grain boundaries, which are also the nucleating sites for twins. Fig. 18b shows the defects in a simulated diffraction (orientation) map. The differences in color designated specific orientations. It is clear that grain orientation plays a major role in the

mechanical response of individual grains and their collective behavior.

3.3. Interatomic potentials

A significant advancement in the field of computational materials science was the development of the embedded atom model (EAM) by Daw & Baskes [111] for simulating metallic atoms. The foundation of the method is to include delocalized interactions in addition to nearest neighbor contributions. The EAM potential takes the following form:

$$E_{Tot} = \sum_i F_i(\rho_i(R_i)) + \frac{1}{2}\sum_{i,j} \varphi(R_{ij}) \tag{23}$$

The first term evaluates the contribution of electron density, ρ_i, at each site, R_i, through a functional, F. The second term considers a short-range pair potential, φ, for each atom pair, R_{ij}, where the "½" avoids double counting. The embedding term essentially takes into account the entire environment of the atom. As implemented, the embedding function is inherently spherical. This may be a drawback for many elements of increasing ionic or covalent nature, but is able to quickly and accurately capture the effect of delocalized electrons in a large number of metallic systems.

Further reading on the direct contributions of the embedded-atom method to material science and engineering can be found in a recent review article [112] and a historical comparison of its projected influence back in 1996 [113]. The EAM was also modified by Baskes [114] to account for directionally-dependent bonding structures and impurities.

Our understanding of simulating and understanding materials at the atomic scale has historically been semi-empirical. Parameters are drawn from experimental results and from quantum mechanics modeling (referred to as *ab initio* methods or with varying functionals representing spatially dependent electron density termed density functional theory (DFT)). Interatomic potentials are then fit to parameters that commonly include elastic constants, cohesive energy, defect energies, and other parameters of interest. Semi-empirical potentials principally allow for simulations that would be otherwise prohibitively costly in terms of computation time.

Interatomic potential development, specifically many-body potentials as applied to metals stems from our most basic understanding of how electrons and/or bonding operate in solids [115] and what the researchers aim to simulate. One ramification of spherically projected potential forms such as EAM is the difficulty of fitting to non-FCC metals [112]. For example, BCC is difficult to accurately fit to due to large contributions of d-shell electrons, and HCP is challenging due to a high degree of mechanical and structural anisotropy.

Computation complexity continues to grow and with increased complexity and number of interactions offers the possibility for increasing realism. This draws also draws on the difference between simulation and modeling. Typically a model is thought of as a simplification or the bare essence of a system where a true simulation would attempt to recreate the system in its entirety. A valuable way to look at complexity was visualized by Plimpton and Thompson [116] and reproduced here in Fig. 10. This illustration is similar to the familiar Moore's law expressed previously in the grain size "growth" of simulations. Table 1 lists the most common potentials used for the principal structures. For a digital compendium of applicable potentials readers are directed to the Interatomic Potentials Repository Project [117] and work by Sheng [118].

Table 1
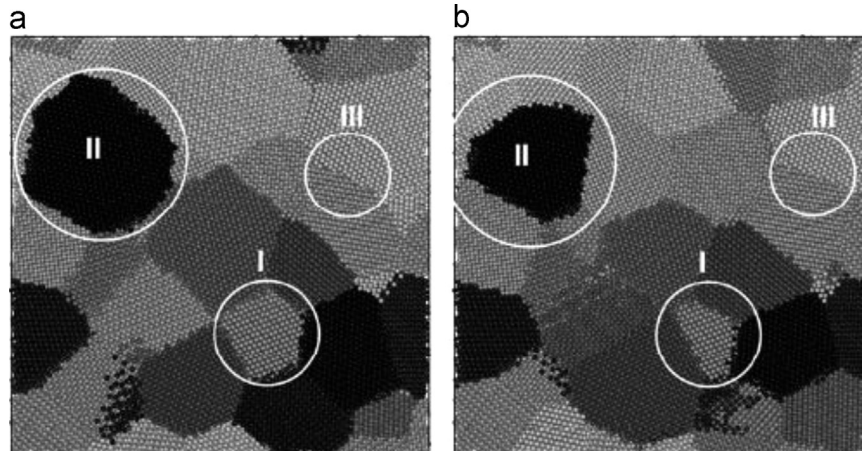Common Potentials for different Metals and Structures.

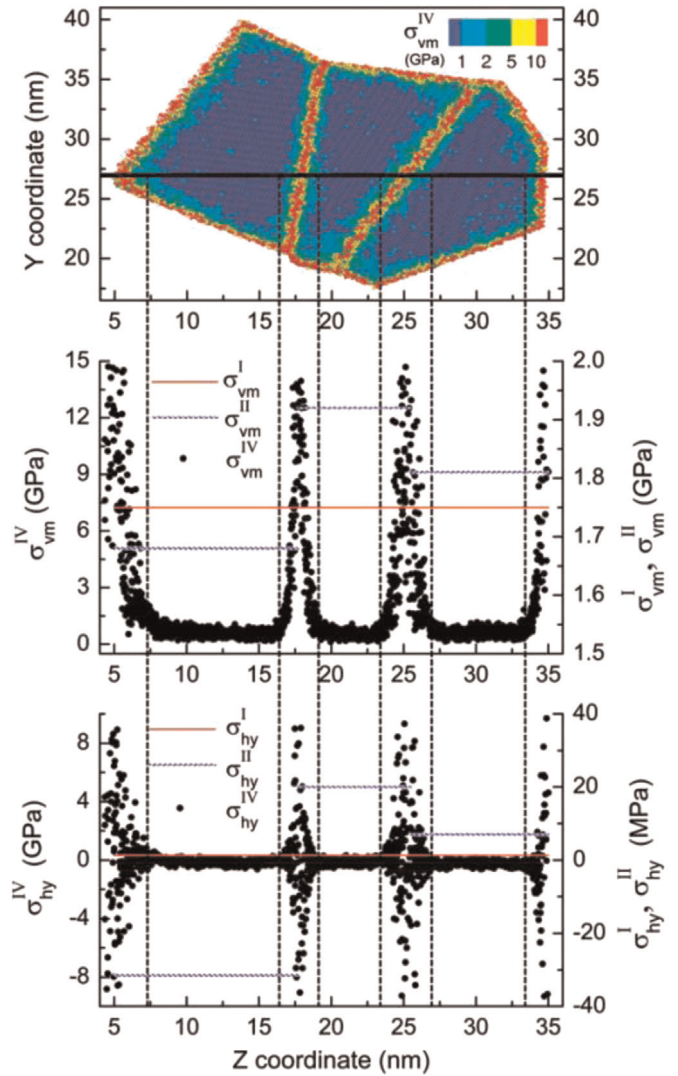| Structure	Element	Potential(s)	Ref.
FCC	Cu	EAM	[217]
	Al	EAM	[218]
	Ni	EAM	[218]
	Ag	EAM	[219]
	Pd	EAM	[220]
BCC	Ta	EAM	[108]
		MGPT	[221–224]
		qEAM	[225]
	Mo	EAM	[226]
		MEAM	[227]
	Nb	EAM	[226], [228]
	W	EAM	[226]
		FS	[229]
HCP	Mg	EAM/FS	[230]
	Ti	EAM	[231], [232]
		MEAM	[233], [234]
DC	Si	SW	[235]
		Tersoff	[236,237], [238], [239]
		EDIP	[240]
		ReaxFF	[241]
		MEAM	[242]
2D Hexagonal	C	Tersoff	[239]
		ReaxFF	[243]
		REBO	[244]
		AIREBO	[245]
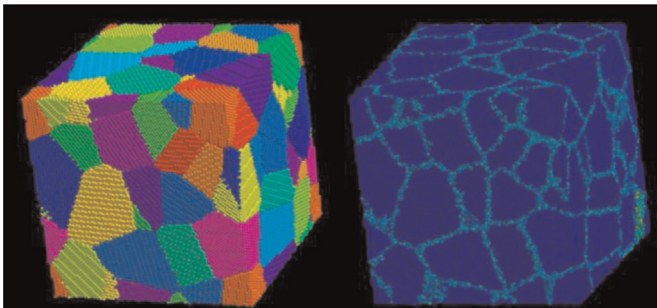
Fig. 19. (a) Different grains designated by different colors as generated by Voronoi tessellation, not the straight lines indicative of the geometric relation between grain centers. (b) Grain-boundary atoms in light blue identified by CSP after relaxation [255].

3.4. Polycrystalline sample construction

Fig. 19a shows a box containing approximately 100 grains, which are identified by different colors. This structural grain

Fig. 21. Snapshot of atomic scale stresses shown along the solid black line traversing multiple grains after Voronoi construction but before thermalization. (top) atoms colored by von Mises stress. One fourth of the residual stress averaged over the entire sample shown in red. Intergranular stresses averaged over each grain shown in blue. Middle pane shows distribution of von Mises stress and bottom pane shows hydrostatic stress distribution [120].

configuration was generated by Voronoi tessellation and the grain-boundary atoms, identified by CNA, are shown in light-blue in

Fig. 20. Vertex growth method (left) vs. Voronoi Tesselation (right). Refer to Wolf et al. [23] for alternatives to Voronoi tessellation.

Fig. 19b, whereas grain interiors are dark blue. One characteristic of the Voronoi tessellation is that all boundaries are flat surfaces. The differences between actual and simulated grain structures are still significant. For instance, annealing twins and other low energy boundaries (Σ3, Σ5, Σ7, Σ11, etc) that are prevalent in low stacking fault energy FCC metals, do not have their higher propensity well recreated in simulations because of how orientation distributions are prescribed. In Voronoi tessellation, the orientations of the generated grains are usually prescribed though a random distribution of orientation directions, then taking on a McKenzie distribution of misorientation as prescribed by crystal symmetry. This does not correspond to actual polycrystals, where the low-energy grain boundaries are more stable and orientation relationships between neighbors evolve accordingly.

Varying simulated fabrication methods for producing grain-boundary networks will manifest just as varying experimental manufacturing techniques, through processing dependent mechanical properties. Wolf et al. [23] provides a description of various *in silico* polycrystalline fabrication techniques such as the vertex growth method, Voronoi tessellation, and compaction of monocrystalline spheres by presuming assembly followed by heating. A comparison between the first two methods can be seen in Fig. 20. Nanocrystalline structures have also been fabricated by simulated laser irradiation [119]. Guo et al. [120] investigated internal stresses in polycrystals, namely the residual stress of as-fabricated nanocrystalline Cu.

The Voronoi tessellation creates internal stresses that are of a high magnitude, especially in nanocrystals below 25 nm grain sizes [120]. Fig. 21 shows the variation of von Mises and hydrostatic stresses along a horizontal line drawn across three grains. The average von Mises stress is 7 GPa and is indicated by the red line referred to the right hand side scale ($\sigma_{vm}^{'}$). The variation in the stress is given by the individual dots (.) that are labeled σ_{vm}^{iv}. These vary from 0 to 15 GPa (left-hand scale). The same can be seen for the hydrostatic stresses, except that they have positive (tension) as well as negative (compression) values. This shows that annealing (thermalization) of the Voronoi construction is essential before plastic deformation.

Xu and Li [121], and Li and Xu [122] investigated the appropriateness of Voronoi tessellation to represent physical materials
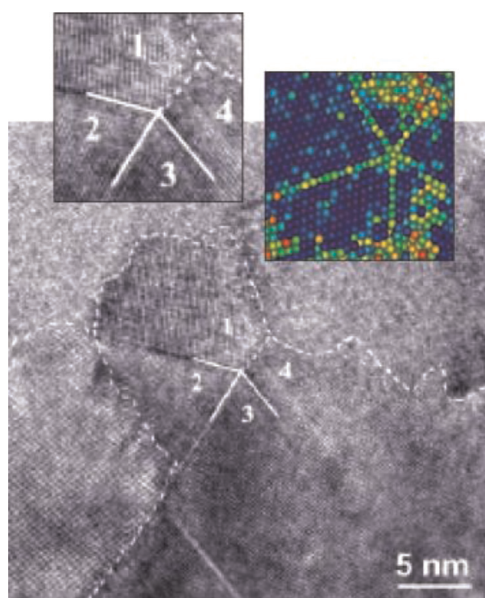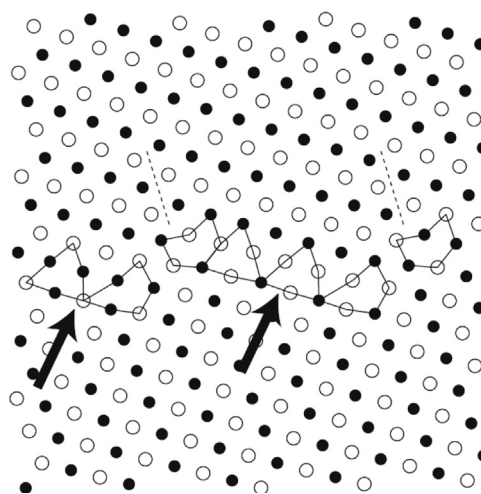

Fig. 23. Snapshot of atomic structure at an asymmetric grain boundary viewed along the tilt axis [110] The open and filled circles indicate atoms occupying alternating (220) planes. Arrows indicate faceting with (001)/(111) plane matching. The dashed lines indicate intrinsic stacking faults that originate from the junctions of the nanofacets [256].

such as polycrystalline aggregates[123]. Theirs is the principal work that investigates the statistical representation of grain size and structure distributions that does not draw as much attention as deformation mechanism research. Through directed Monte Carlo studies they were able to recreate realistic grain textures. The ability to identify and track triple junctions, grain boundary ledges, and faces is seen in Fig. 25. The triple junctions are imaged in red, the grain-boundary intersections are seen in yellow, and the grain boundaries in green. This work is due to Xu and Li [121], and Li and Xu [122]. With such information the authors have access to a complete picture of polycrystallinity including grain boundary shape, texture, and grain size (as well as its distribution). Readers are directed to their work for a description of accurate polycrystal construction and appropriate methodology.

It was recognized earlier that Voronoi constructions may not generate equilibrium structures and larger grain sizes were often generated through long annealing processes. Farkas et al. [124] reported three-dimensional simulations of grain growth beginning with 5 nm grain sizes and were able to generate larger grains and possibly more realistic distributions while also obtaining the activation energy for annealing-twins and grain-boundary motion. Fig. 22 shows fivefold twin formation during an annealing simulation of nanocrystalline Cu as directly compared to experimental evidence of such star shaped twins in nanocrystalline NiW [125] as well as earlier studies by Zhu et al. [126] that found fivefold twins formed in nanocrystalline Cu by high-pressure torsion.

After thermalization, the grain-boundary structure can become faceted as non-equilibrium grain boundaries reach lower energy configurations. This is a well-known fact and explains the facets

Fig. 22. High resolution transmission electron microscopy image of many-fold twin formation in nc NiW. Solid lines are twin boundaries and dashed lines are grain boundaries. A time sequence of formation during molecular dynamics simulation can be found in the original article by Bringa et al.[125].
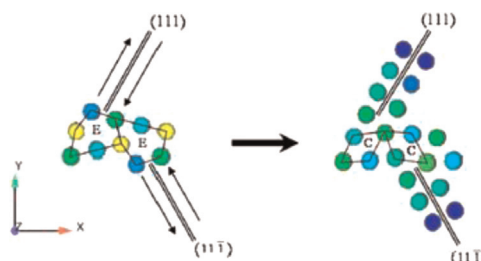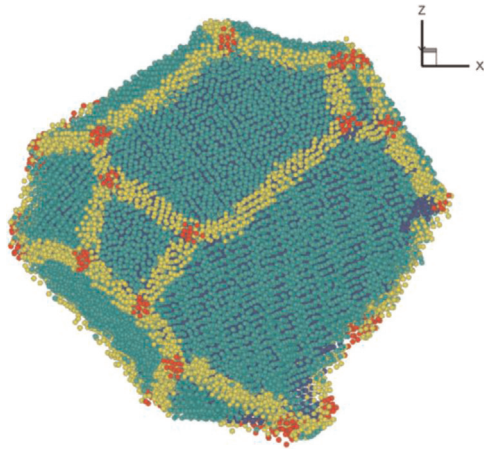

Fig. 24. Special grain boundary configuration indicated by the "E" structural unit and transition to the "C" structure after dislocation transmission [53].

Fig. 25. Visualization of a single grain showing tracking of triple junctions (in red), grain boundary ledges (in yellow), and faces (in green)[121,122].

commonly observed as non-coherent segments in coherent annealing twin boundaries. Thus, for the FCC superalloy Inconel 600 the majority of boundaries are Σ3, Σ7, and Σ13 [127]. For grain boundaries to reach a special configuration, both the grains and the boundary have to be properly oriented. Fig. 23 shows two grains that are at an orientation close to a special coincidence site lattice. The black and white circles designate atoms at two adjoining atomic planes. The faceting of the boundary is evident from the polygon sequences drawn along the boundary. The grain-boundary nature is important in the generation of dislocations. The figure shows two dashed lines which indicate stacking faults that were emitted from the nanofacet junctions. These are also referred, in the older literature, as ledges. Fig. 24 shows two slip systems in neighboring grains intersecting a boundary defined by a polygon sequence designated structural unit E. Upon transmitting from one grain to the other, a dislocation changes the local character of the grain boundary. This is seen by the change of polygonal structure from E to C and indicates that certain grain boundary structures are prone to dislocation transmission while others prevent dislocation motion.

It is clear that a diversity of grain-boundary configurations, or lack there-of, can alter the resulting mechanical properties [128] and the rapid development of realistic grain-boundary networks is critical for well-informed molecular dynamics simulations and continues to be a long-standing goal in the field. One such method to-be-developed is the direct reconstruction of atomistic samples from experimental imaging analogous to DREAM3D [129] for three-dimensional characterization of microstructural inputs

(principally grain-boundary distribution and texture) into continuum modeling frameworks. There is a direct and stated need, through both the Integrated Computational Materials Engineering and Materials Genome Initiative, for the ability to link the processing and internal structure history of a material to its mechanical properties.

4. Molecular dynamics simulations

We present in this section some salient molecular dynamics results emphasizing grain-boundary effects. By virtue of the small size of the simulation box, the results are limited to grains smaller than 50 nm. The three principal structures FCC, BCC, and HCP are presented sequentially with emphasis on the defects responsible for plastic deformation and grain-size effects, and in particular the inverse Hall-Petch relationship.

4.1. Face-centered cubic metals

Early work by Van Swygenhoven et al. [63,130,131] detailed nucleation, transmission, and absorption of a partial dislocation as shown in Fig. 26. The sequence shows the emission of partial dislocations (at the upper left-hand corner) and their progression through the grain and eventual annihilation on the bottom grain boundary. The stacking-fault between leading and partial dislocations is indicated in red (darker gray in printed version). More recent MD simulations have shown that dislocations are emitted from grain-boundary ledges at a lower stress than from planar grain boundary regions [26]. Direct evidence of intragranular deformation mechanisms was observed by TEM [132,133] and Fig. 27 shows that partial dislocations are preferred to full dislocations below a specific grain size [78]. Van Swygenhoven and co-workers [79] also identified varying grain boundary structures of "typical" grain boundaries and quantified sliding mechanisms. Haslam, Wolf, Philpot, Gleiter and other coworkers [134] identified the role of grain rotation as contributing to plasticity and grain growth via grain coalescence during deformation. Fig. 32 details a visualization of grain coalescence by mapping the grain dependent [011] direction of adjacent grains during deformation [135]. This shows the first simulated evidence of grain rotation and coalescence. The degree of relative misorientation is indicated by solid black line; the grain-boundary motion rotates each grain to orient with the other. Thus, a larger grain is formed by the joining of two grains. Simulation results by Trautt and Mishin [136] verified predictions made by Cahn and Taylor [137] regarding dynamics of grain boundary motion. Their results indicate that grain-boundary
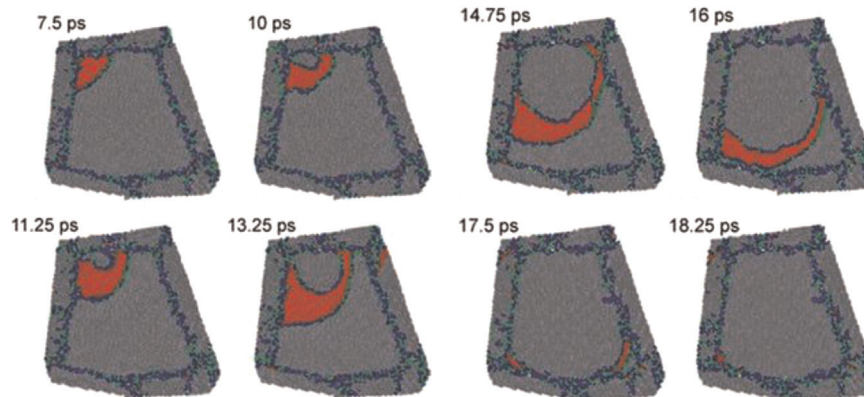
Fig. 26. Early work by Swygenhoven et al. detailing nucleation, transmission, and absorption of a partial dislocation [257]. Leading partial emitted from top left-handed corner propagating towards bottom right hand corner, followed by trailing partial dislocation. Stacking fault between them in red.
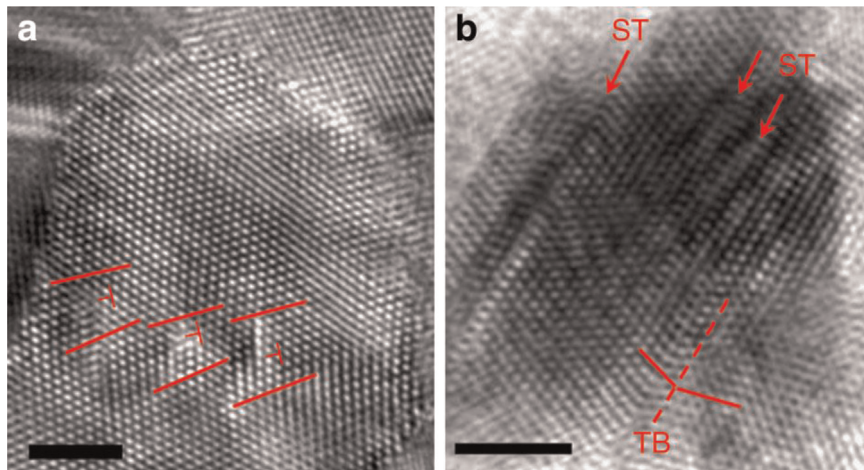
Fig. 27. (a) Full dislocations (marked with 'T') in an ~11- nm-sized grain. (b) Partial dislocations resulting in stacking faults (as noted by the arrows) in a ~7- nm-sized grain. Scale bars, 2 nm. TB indicates a twin boundary. From Wang et al. [78].
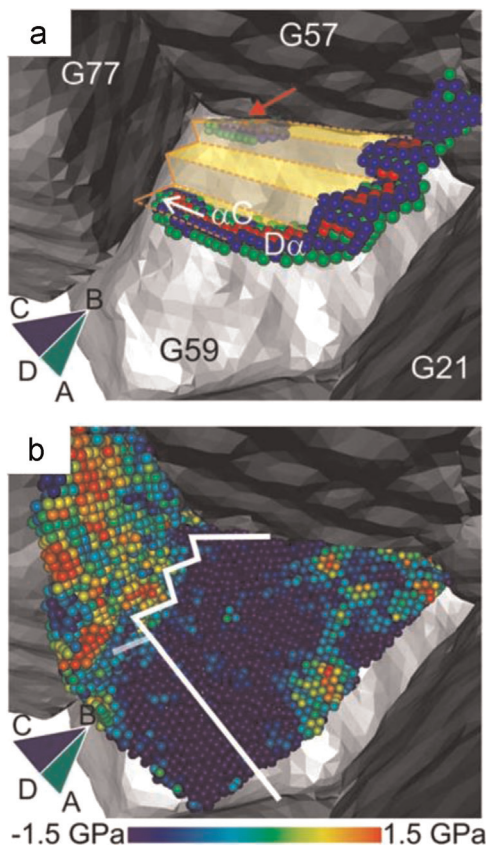
Fig. 28. Snapshots colored according to local hydrostatic pressure. (a) Dislocation propagation by several cross-slip events. Only the dislocation atoms are shown to illustrate the dislocation core. (b) Grain boundary atoms onto which the dislocation was deposited leaving a trace (white line) of the cross-slip events [139].

motion is not perfectly coupled. Simulations indicate that grain-boundary motion will always involve a proportion of sliding. A ramification of this is that, again, grain boundaries continually change and thus grain boundary dislocations content waxes and wanes. A related result indicates that shear boundary motion and sliding each have their own critical stress [138].

Bitztek et al. [139] details the driving force to cross slip in order to decrease compressive stresses in a neighboring grain. This is significant because cross slip is known to reduce strain hardening and thus presents a strong argument for the lack of observed

strain hardening in nanocrystalline simulations. The influence of cross slip within grains can also be seen in Fig. 28 as the morphology of the grain-boundary layer adjusts to allow the adsorption of the moving partial. However, cross-slip requires the collapse of the partials into a screw dislocation.
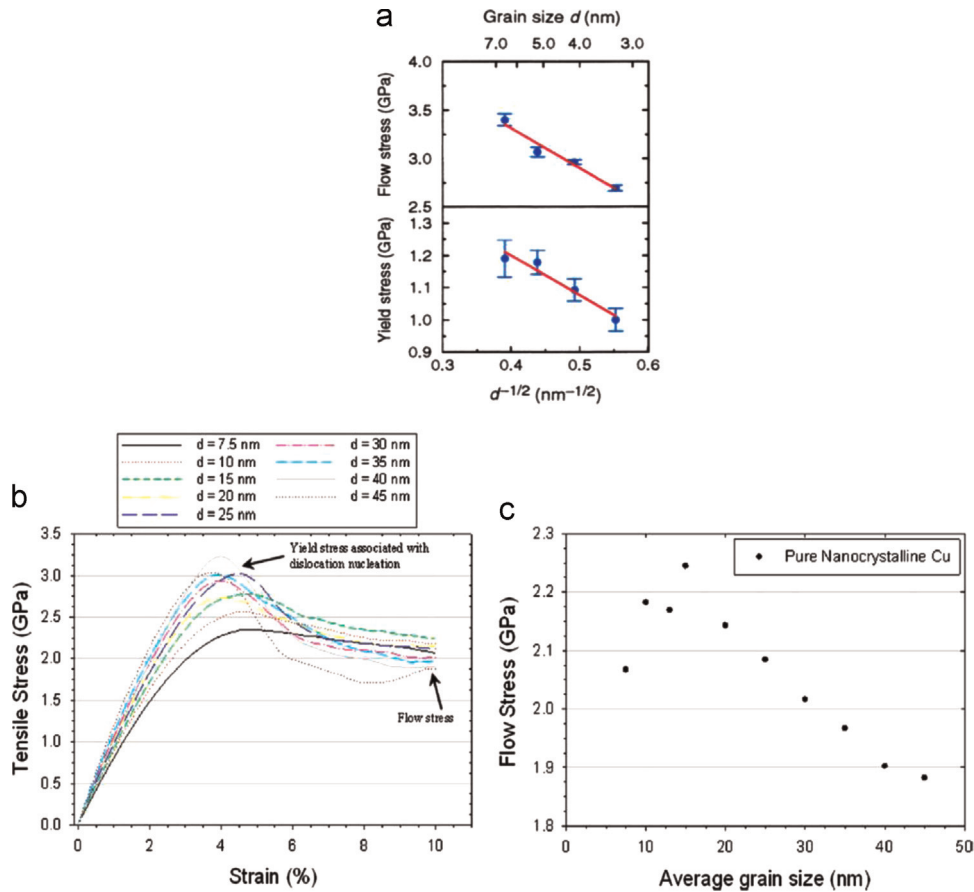
Fig. 29 shows MD simulations of flow and yield stress versus strain for four different grain sizes in Cu. The inverse HP relationship is shown in the simulations of Fig. 29a while Fig. 29b shows the entire curves and the 'Strongest Size' is shown in Fig. 29c.

The near absence of strain hardening in nanocrystalline metals is observed both experimentally and computationally. This is especially visible in Fig. 29b, where the stress-strain curves go through a maximum at a strain of ~4%. Work (or strain) hardening is inherently connected with the increase in dislocation density and all theories are based on this premise, starting from Taylor in 1934 [140] to current mechanisms that incorporate greater complexity in the structure evolution and mechanical response. (e.g., Seeger [141], Hirsch [142,143], Kuhlmann-Wilsdorf [144]). The classic Taylor prediction is:

$$\tau \propto \rho^{1/2} \tag{24}$$

In nanocrystalline metals, the closeness of sources and sinks (approximately equal to d) has a pronounced effect on dislocation interaction, which is significantly decreased. Plastic deformation proceeds primarily by the emission of dislocations and their annihilation at the opposite boundary. In tension, this leads to early necking while in compression there is a virtual absence of work hardening, after a critical strain. Both are undesirable qualities. Lu et al.[145] were able to synthesize, through pulsed electro-deposition, nanocrystalline copper where the majority of boundaries are coherent twins, resulting in much improved tensile ductility. This is connected to the ability of dislocations to cross these boundaries, that nevertheless exert a significant resistance.

Cross-slip is also one of the many properties shown to be strain-rate dependent [146]. This is also a ramification of the delayed onset of dislocation propagation at high strain rates. MD simulations consistently predict the increase in flow stress with strain rate in the 10^7-10^9 s^{-1} interval. The elastic-plastic limit for nucleating dislocations is highest at the highest strain rate of 10^9 s^{-1}. This means that at higher strain rates and large strains, more dislocations are required to mediate plastic flow. The number of cross-slip events decreases with increasing strain rate. Vo et al. [147] demonstrated that Young's modulus is independent of strain rate, but that flow stress is markedly dependent with a large effect at 10^{10} s^{-1}.

Fig. 29. (a) MD simulations of flow and yield stress versus strain for four different grain sizes in Cu. Each data point is the average of seven simulations. The yield stress decreases with decreasing grain size, resulting in an inverse Hall–Petch effect. The maximal flow stress is taken as the stress at the flat part of the stress–strain curves; the yield stress is defined as the stress where the strain departs 0.2% from linearity.) [216] (b) stress-strain curves for grain sizes from d=7.5 to 45 nm in nanocrystalline copper; (c) flow stresses as a function of grain size showing inverse HP region[53].
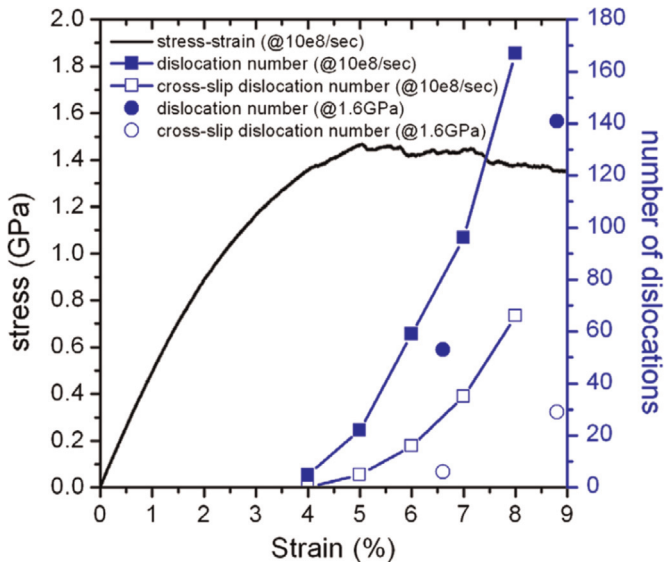
Fig. 30. Plot of stress-strain and dislocation count-strain for two uniaxial tensile tests under different conditions. Squares correspond to constant strain rate of $10^8 s^{-1}$. Circles correspond to a constant pressure (1.6 GPa). Total number of dislocations in blue and number of cross-slipping dislocations shown by white [139].

Below a critical grain size, deformation twinning becomes important. These twins are formed primarily by three mechanisms, according to Wolf et al. [23].

- Stacking faults overlapping in the grain interiors.
- Coordinated nucleation of partial dislocations at the grain boundaries, forming twins.
- Grain-boundary splitting.

Liao et al.[148,149] discuss this twinning mechanism as well as the increasing separation of partials below a critical grain size. These mechanisms are distinct from twin formation in large, micrometer-sized grains, that were reviewed by Meyers, Vöhringer, and Lubarda [150].

Fig. 30 shows the stress-strain and dislocation count-strain for two uniaxial tensile tests under different conditions. Squares correspond to constant strain rate of $10^8 s^{-1}$. Circles correspond to a constant pressure (1.6 GPa). Total number of dislocations in blue and number of cross-slipping dislocations shown by white [139]. It can be seen that the mode of application of stress affects the dislocation density. Fig. 31 shows stress-strain curves for three strain rates, $10^7 s^{-1}$, $10^8 s^{-1}$, and $10^9 s^{-1}$. As the strain rate is increased the resistance of the metal to plastic deformation predictably increases. The dislocation density does not seem to be affected in a systematic way. Dislocations per 1% strain as a function of strain rate for all three strain rates are shown in Fig. 31b. The cumulative count of cross-slip events normalized by the number of grains is shown in Fig. 31c. [146]. The number of cross-slip events, which increases with strain, decreases with increasing strain rate. This greater planarity enhances the tendency for twinning.

Molecular dynamics also shows how grain rotation can lead to coalescence. Successive snapshots illustrating the atomic scale mechanism of a rotation-coalescence event are shown in Fig. 32.
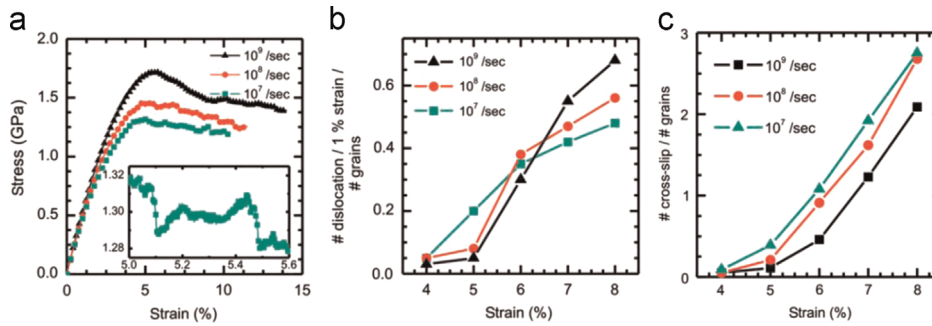
Fig. 31. Stress-strain curves for three strain rates, 10^7 s^{-1}, 10^8 s^{-1}, and 10^9 s^{-1}. Inset in (a) shows discrete dislocation stress drops associated with individual dislocation propagation within grains at 10^7 s^{-1}. (b) Dislocations per 1% strain as a function of strain rate for all three strain rates. (c) Cumulative count of cross-slip events normalized by the number of grains [146].

The initial misorientation between grains 8 and 14 is 18. At increasing time steps the angle of misorientation decreases from 18° to 11°, 9°, and 4°. The decreasing areas of grains 8 and 16 indicate that rotation-coalescence and grain boundary migration mechanisms are coupled to one another [135]. Fig. 33 shows experimental in situ TEM imaging of grain rotation and grain boundary annihilation of ∼5-7 nm grains [78]. The white arrow in b indicates the loading axis. In (a), grain 1 is surrounded by high-angle GBs. With straining the grain rotates and the boundaries between grains 1-3 and 1-4 transition to small angle grain boundaries. With increasing strain the grain boundary is annihilated and grains 1 and 3 coalesce into a single grain.

Coupled grain boundary motion as detailed by Schäfer et al. [151] can be seen in Fig. 34 where compatibility between grains

dictates that motion of the boundary occurs according to the cooperative displacement. This coupled motion has also been seen in asymmetrical tilt grain boundaries [152]. It was also shown by Brandl et al. [153] that grain boundaries are not necessarily the static structures that we think them to be, especially under dynamic loading. Frolov and co-workers [154] showed that grain boundary structure was critical in determining such coupling factors and the motion of such boundaries. This work builds upon a recent investigation that uncovered first grain-boundary structural phase transitions in metallic grain boundaries [155].

The main impediment to previous observation of such phase transitions in atomic simulations was the lack of variation in atomic density within a given boundary. As temperature increases, the grain boundary thickness increases as seen in Fig. 35. This
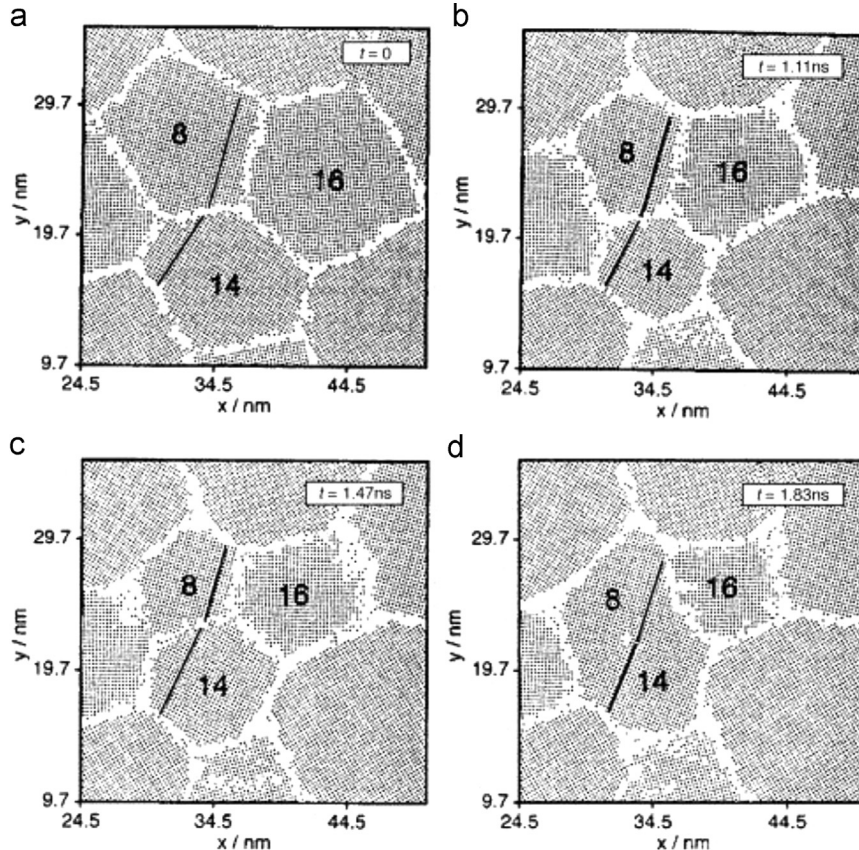
Fig. 32. Successive snapshots illustrating the atomic scale mechanism of a rotation-coalescence event. Solid black lines indicate < 110 > direction and the initial misorientation between grains 8 and 14 is 18°. At timesteps b-d the angle of misorientation decreases to 11°, 9°, and 4 °respectively. The decreasing areas of grains 8 and 16 indicate that rotation-coalescence and grain boundary migration mechanisms are coupled to one another [135].
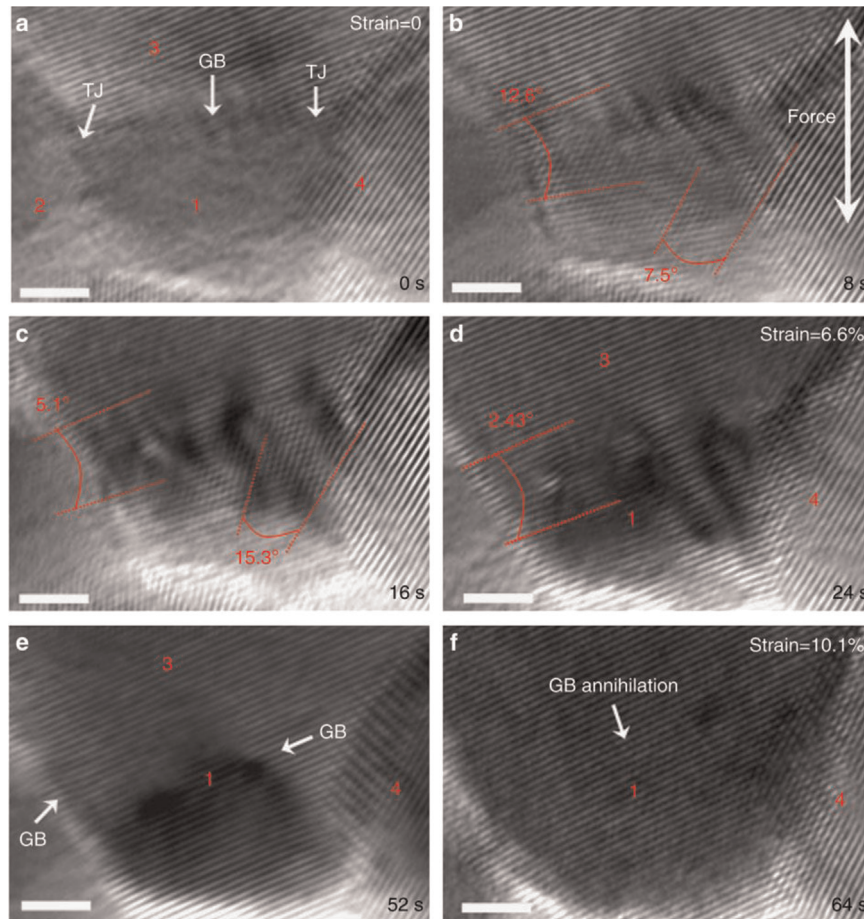
Fig. 33. Experimental in situ imaging of grain rotation and grain boundary annihilation of ~5-7 nm grains. The white arrow in b indicates the loading axis. In a, grain 1 is surrounded by high-angle GBs. With straining the grain rotates and the boundaries between grains 1-3 and 1-4 transition to small angle grain boundaries. With increasing strain the grain boundary is annihilated and grains 1 and 3 coalesce into a single grain. Scale bars, 2 nm. From Wang et al. [78].

thickening would have an effect on strength derived from the ratio of grain boundaries to grain interiors as introduced earlier based on work by Argon and Yip [36]. This serves as a reminder of the importance of residual "porosity" within grain boundaries and reemphasizes the need for imparting increasing degrees of realism into simulations.

The limited work hardening ability of nanocrystalline metals is the direct result of the availability of sinks (the grain boundaries). Thus, specimens tend to undergo necking right after plastic flow. This is corroborated by MD simulations. The decrease is ductility with increasing strength is a characteristic of all metals, and the search for increased ductility has been a challenge for researchers worldwide. The development of TRIP steels which use a martensitic transformation the decreases the stress concentrations at the crack tip, represents a significant advance. Steels subjected to the treatment are shown in Fig. 36a as an 'island.' The DPD nanocrystalline copper have a better performance than the TRIP (TRansformation Induced Plasticity) steels. In nanocrystalline metals, several developments are worth mentioning:

- The use of pulsed electroplating to generate a nano-scaled structure consisting primarily of coherent annealing twins. This work has been spearheaded by Lu and coworkers [156] at IMR, Shenyang, China.
- Gradient structures in which the surface is nanocrystalline and the interior is polycrystalline are effective in retarding necking [157–159].

The combination of strength and ductility translates into toughness, and this is shown in Fig. 36.

In Fig. 36a, DPD (Dynamic Plastic Deformation) is a treatment by which a nanocrystalline structure with high twin density is produced [156]. SMAT (surface mechanical attrition treatment) is a technique by which the surface is hardened through the formation of a nanocrystalline layer, while the interior has a conventional polycrystalline structure [157–159]. Both processes push the tensile strength-elongation envelope to the right, increasing the ductility at a fixed level of strength. Fig. 36b shows that some nanocrystalline structures can have a combination of strength and ductility that place them significantly to the right of the blue region, with higher toughness. Special processing procedures can access this region. Shifting towards the right is also shown in Fig. 36c, in which the combination of polycrystalline and nanocrystalline structures leads to enhanced ductility, at a specified strength level. The gradient structure has both a high strength and the ductility due to the polycrystalline core.

In tensile deformation, grain-boundary void formation is a prevalent mechanism and perhaps a peculiarity of the high-strain rates imparted by MD simulations. The opening of voids at the grain boundaries is accompanied by profuse emission of partial dislocations, which transform a sharp separation into a broader void. The simulation sequences are shown in Figs. 37 and 38, for uniaxial strain tension and hydrostatic tension respectively. The arrows indicate places in the grain boundaries where void initiation takes place. The light-blue lines are either grain boundaries or stacking faults. The simulation views
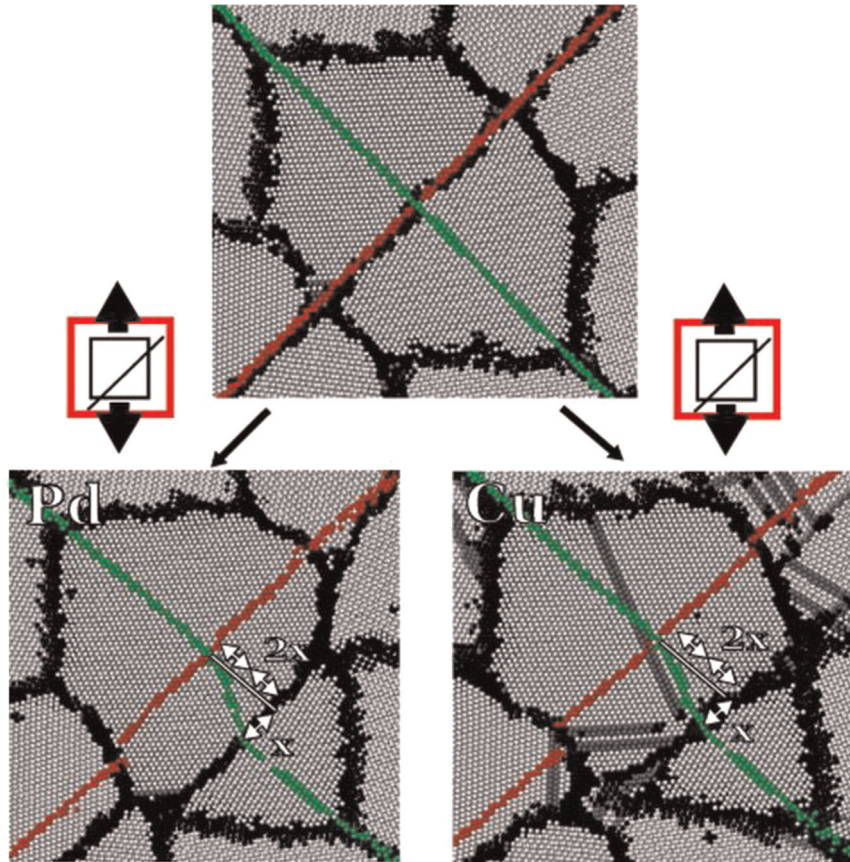
Fig. 34. Coupled grain boundary motion in Pd and Cu crystals occurring at a grain boundary of misorientation of about 33 °between grains. Top snapshot shows initial configuration with marker atoms in red (aligned with mesoscopic slide plane) and green (perpendicular to mesoscopic slide plane), grain boundary atoms in black, and fcc atoms in light gray. The evolution of the marker lines during loading determines an estimated coupling factor of 0.5 [151].
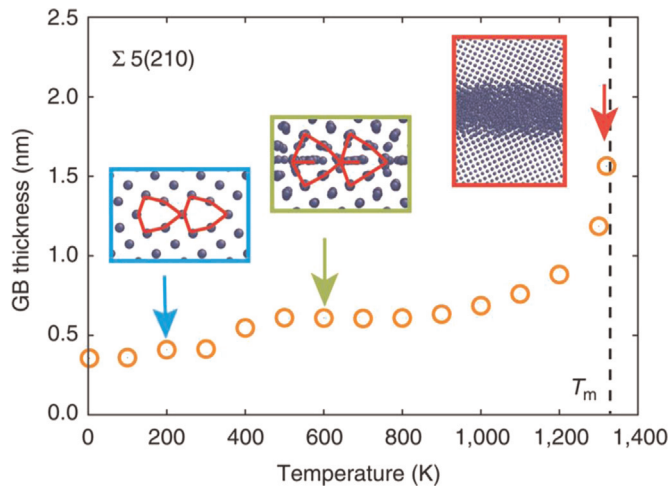

Fig. 35. The thickness of Σ5(310) GB increases and undergoes phase change at increasing temperature. The Σ5(310) GB undergoes a transformation at 400 K before pre-melting near T_m. From Frolov et al. [155].
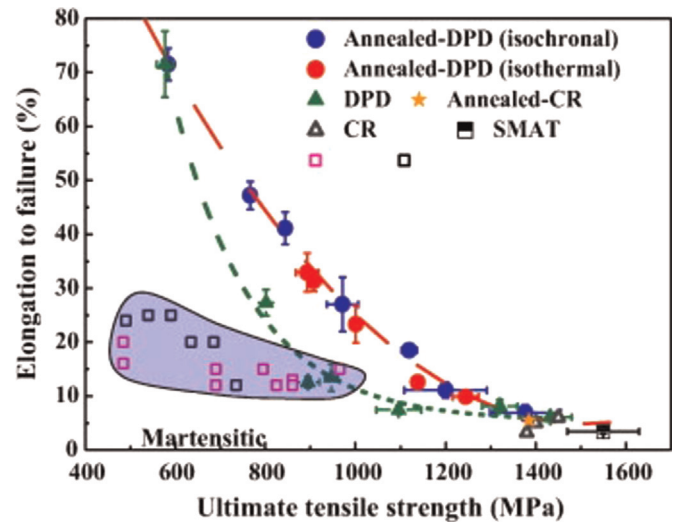

Fig. 36a. Correlations of tensile strength and ductility. Purple squares are from Washko and Aggen [258], black square from Truman [259], black and white box from Chen et al. [260], black triangle from Ucok et al. [261], Stars from Eskandari et al. [262] and original data from Yan et al. [156]. DPD: dynamic plastic deformation; CR: cold rolling; SMAT: surface mechanical attrition treatment.

represent slices with thickness equal to a_0. The process of tensile failure is one of nucleation, namely of voids at the grain boundaries, and their subsequent growth and coalescence. Interestingly, copper (and other metals) fail in the same intergranular ductile mode under tensile pulses created by reflected shock waves, whereas quasistatic failure occurs by the nucleation of voids inside the grains.

4.2. Body-centered cubic metals

Among simulations of metals, body-centered cubic structures are the second most commonly studied. Of BCC metals, iron is the most studied for its obvious industrial applications. Fig. 39 shows
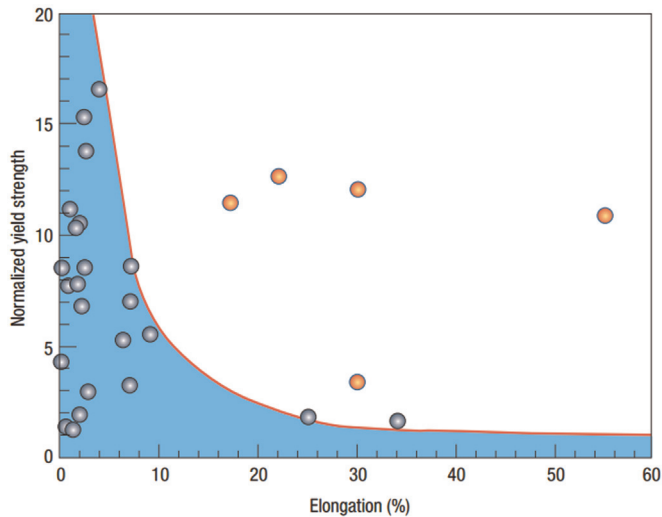
Fig. 36b. Normalized yield strength versus elongation for nanostructured metals. Measured yield strength has been normalized by dividing it by the yield strength its coarse-grained counterpart. The blue region represents the strength-ductility tradeoff for most nanostructured metals. The red points outside of this region represent several nanostructured copper samples that exhibit high strength and good ductility. Figure from Y. Zhu [267]. Data is from Kocks [268].
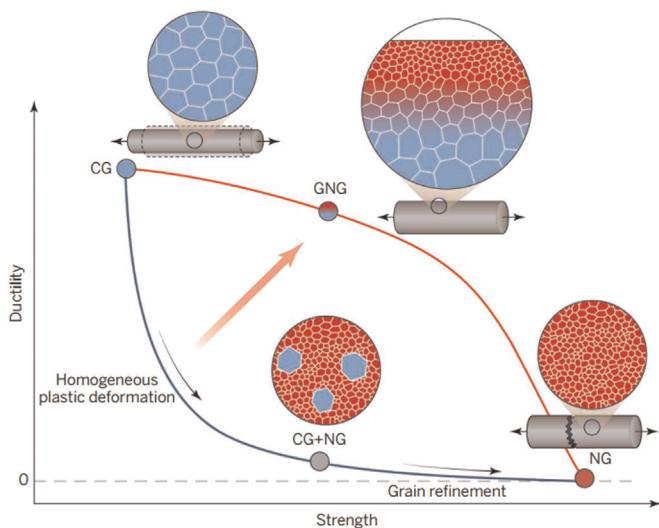
Fig. 36c. Strength-ductility synergy is achieved with gradient nanograined (GNG) structures (red line). From Lu et al. [269].

snapshots of nanocrystalline iron where grain sizes less than 5 nm are devoid of dislocations and ∼20 nm grains have minimal dislocation activity [160]. Accurately capturing a full suite of polymorphism and plasticity mechanisms leads researchers to compare potential-dependent deformation in nanocrystalline iron [161,162]. The inverse Hall-Petch relationship for nc-Fe of peak stress is shown up to a size of 19.7 nm, but the flow stresses show return to normal HP behavior above 14.7 nm for 0-4% inelastic deformation and 9.25 nm for 4-15% inelastic deformation [160]. Thus, there are differences in the evolution of plasticity in these grain sizes. Recent studies Gunkelmann and co-workers [161,162] have focused on the shock response of nanocrystalline Fe. Both plasticity and phase change (bcc phase to the high-pressure hcp phase) were observed in large, 8-million atom nanocrystalline Fe samples. Their findings show that phase transformation is preceded by dislocation generation at grain boundaries and that plasticity occurs primarily by dislocation loop generation. Loops

travel across individual grains and leave behind residual screw dislocations. Due to the interplay between plasticity and phase change, research into purely BCC mechanical behavior has shifted partly to archetypal BCC elements. Simulations by Kadau et al. [163] calculated extended x-ray absorption fine structure directly from atomic configurations and show consistency with experimental data indicating the BCC to close-packed phase change. Fig. 40 shows snapshots of dislocation activity in nanocrystalline bcc Fe for varying potentials colored by structure as determined by CNA: yellow (bcc), blue (other, i.e. grain boundaries, defects, and non-bcc close-packed structures). From top to bottom the potentials are: Mendelev, MEAM-p, Ackland, Voter. Compressive strains increase as indicated from left to right [161]. The differences are clear.

Tantalum serves as a prime candidate material for studying plasticity in BCC metals owing to its high phase stability (lack of polymorphism and high melting temperature/pressure). Pan et al. [164] simulated nanocrystalline Ta up to 13 nm and observed an inverse Hall-Petch response. They also found a strain-rate sensitivity of 0.14 as compared to closer to 0.04 for coarse-grained BCC metals [165]. This was attributed to a reduction in activation volume to $\sim b^3$ indicative of atomic shuffling events. Larger grain sizes were simulated by Tang et al.[166]. The grains, varying from 3 to 30 nm, were produced by Voronoi tessellation; the size of the samples was $(66\ nm)^3$ and the strain rates applied were $10^8\ s^{-1}$ in tension and $10^9\ s^{-1}$ in compression. The behavior in tension was radically different from the one in compression. In tension, grain-boundary separation occurs with a minimum of plastic deformation and occasional twinning. This is in contrast with FCC copper (see Figs. 37 and 38), where tension initiated voids at the grain boundaries, from which large numbers of dislocations were emitted. This is probably related to the much greater strain-rate sensitivity of BCC metals because of the larger Peierls-Nabarro stress. Thus, the stress for grain-boundary decohesion is lower than the flow stress at the particular strain rate. Fig. 41a-d shows the sequence of failure by grain-boundary separation and a schematic Fig. 41 shows the presumed mechanism of grain-boundary separation. In Fig. 41e-f the interaction of a propagating interfacial crack and twin is shown.

The presence of a twin helps to open the crack. By comparing Fig. 37, Fig. 38, and Fig. 41, the difference between BCC and FCC is clear.

In compression, on the other hand, cracks do not open at the grain boundaries and plastic deformation takes place. Fig. 42 shows the von Mises stress increasing with increasing grain size; it seems to reach a plateau at 30 nm, although beyond this point was not simulated due to computational limitations.

At $d=5$ nm there is considerable grain rotation and shear as evidenced by the arrows which indicate the direction and magnitude of in-plane atomic movement (Fig. 43). This was also shown earlier by Pan et al. [164] for 6.5 nm grains using an earlier EAM potential developed for several bcc metals [167]. The dislocation densities were estimated using the DXA algorithm and found to be constant for different grain sizes, at equivalent strains. As expected, the dislocation density increased with increasing plastic strain. This behavior is indeed interesting and shows that grain-boundary shear is prevalent at the smaller sizes, as will be shown below. Tang et al. [166] considered the total strain γ_T composed of the sum of elastic strain γ_E, dislocation strain γ_D, and grain-boundary strain γ_{Gb}:

$$\gamma_T = \gamma_E + \gamma_D + \gamma_{Gb} \qquad (17)$$

At a constant total strain the sum $\gamma_{D+\gamma_{Gb}}$ is a constant. The Orowan equation is now applied:

$$\gamma_D = M\rho bl \qquad (18)$$
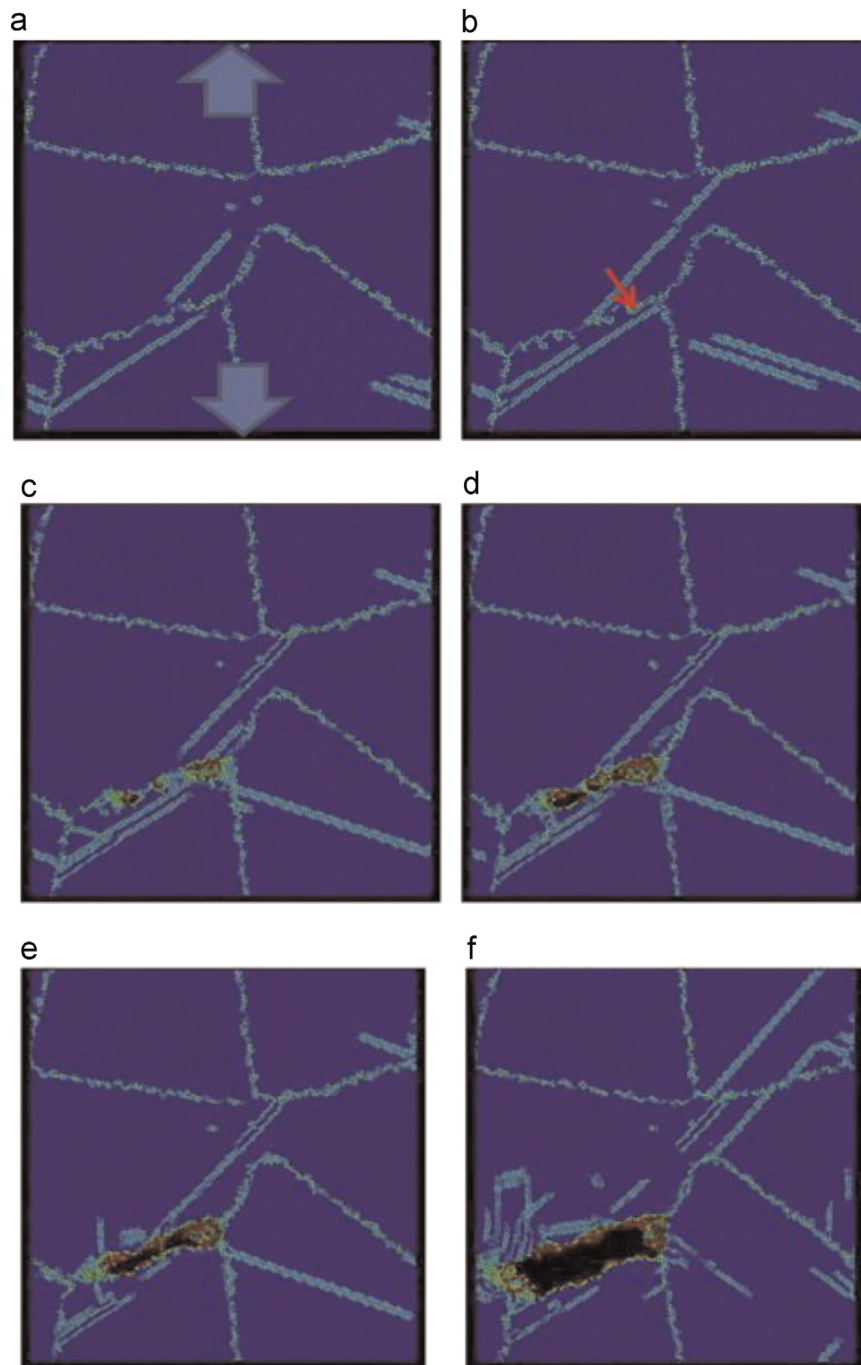
Fig. 37. Slices (a_0 thick) of the nanocrystalline copper with d$\sim$ 20 nm subjected to uniaxial tension. Strains are: 6%, 6.5%, 7%, 7.2%, 7.3% and 8%. Lattice atoms: blue; void surface atoms: red/green; stacking faults, partial dislocations and twin boundary atoms: light blue. Stacking faults show as two planes of atoms while twin boundaries show as a single atomic plane. (a) Emission of partial dislocations from GBs; (b) void nucleation (marked by an arrow); (c) three voids nucleated at a grain boundary; (d) coalescence of voids; (e and f) void opening by continued dislocation emission at its extremities. A few twin boundaries are seen in frames (c) and (d). From Bringa et al. [263].

Setting l, the mean free path, equal to d and assuming that the grain boundary contribution is zero, one arrives at:

$$\rho = \frac{\gamma_T - \gamma_E}{Mbd} \qquad (25)$$

The results of the MD simulation and Equation 25 are shown in Fig. 44 for a strain of 0.18; they demonstrate that, for d < 30 nm, the Orowan equation overestimates the dislocation density. The difference in density is accommodated by grain-boundary shear. This corroborates the results attributing the deformation in the inverse Hall-Petch region to grain-boundary shear. From both Orowan equation and from MD predictions in uniaxial compressive strain Orowan-based densities for accommodation of plastic strains $\gamma_t - \gamma_e$ are nearly proportional to grain size $1/d$; the role of grain-boundary shear decreases with increasing grain size d.

Work by Rudd [107,109] indicates that both dislocations and twinning are observed in tantalum during high strain-rate deformation. Pan et al. [164,168] observed twins in small grain sizes and dislocations in larger grains. Zhang et al. [169] simulated < 110 > columnar grains of molybdenum, identifying primarily twin deformation, which agrees well with work by Tramontina et al. [170] showing an increased propensity to deform by
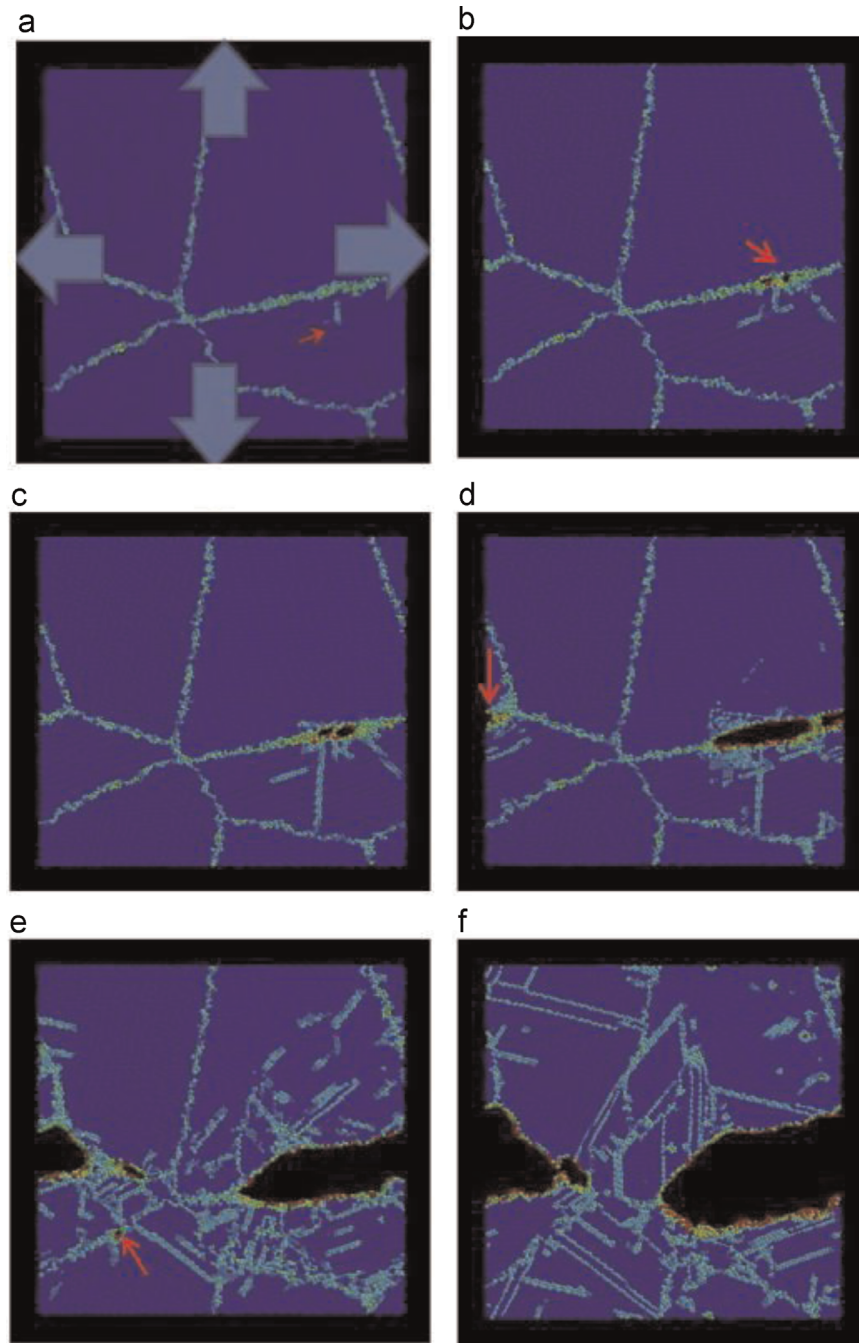
Fig. 38. Slices (a_0 thick) of the nanocrystalline copper with d $\sim$ 20 nm subjected to hydrostatic tension. Same color scheme as in Fig. 37. Void nucleation and associated dislocation strucutres are much more drastic than uniaxial tension. From Bringa et al. [263].

twinning in $<110>$ single crystals of Ta. Earlier simulations of nanocrystalline molybdenum by Frederiksen et al. [171] show a propensity for both twinning and grain boundary sliding at high strain rates. Simulations agree well with nanoindentation of 10-30 nm nanocrystalline tantalum by Wang et al. [172].

Smith et al. [173] simulated thin films of nanocrystalline tantalum achieving strain rates as low as 10^5 s^{-1}. At low strains and low strain-rates dislocations are the primary means of deformation, but above 5% strain and strain rates of 10^6 s^{-1} twinning was shown to play a significant role, especially at strain rates above 10^8 s^{-1} where twinning is the initial deformation mechanism. They found the strain rate sensitivity to increase markedly above 10^7 s^{-1}. Analysis of grain boundary sliding

showed that there is little dependence of sliding on strain rate.

Fig. 45 shows peak and average flow stresses as a function of grain size for nanocrystalline Fe [160]. The maximum occurs, at 4% strain for d $\sim$ 15 nm. This is consistent with other metals, as shown in Table 2. The curves show a maximum at $\sim$15% and then drop demonstrating that work softening follows work hardening in nanocrystalline Fe.

4.3. Hexagonal close-packed metals

Hexagonal close-packed metals continue to be the least investigated of the principal crystal systems despite the technological importance of magnesium, titanium, zirconium, and cobalt.
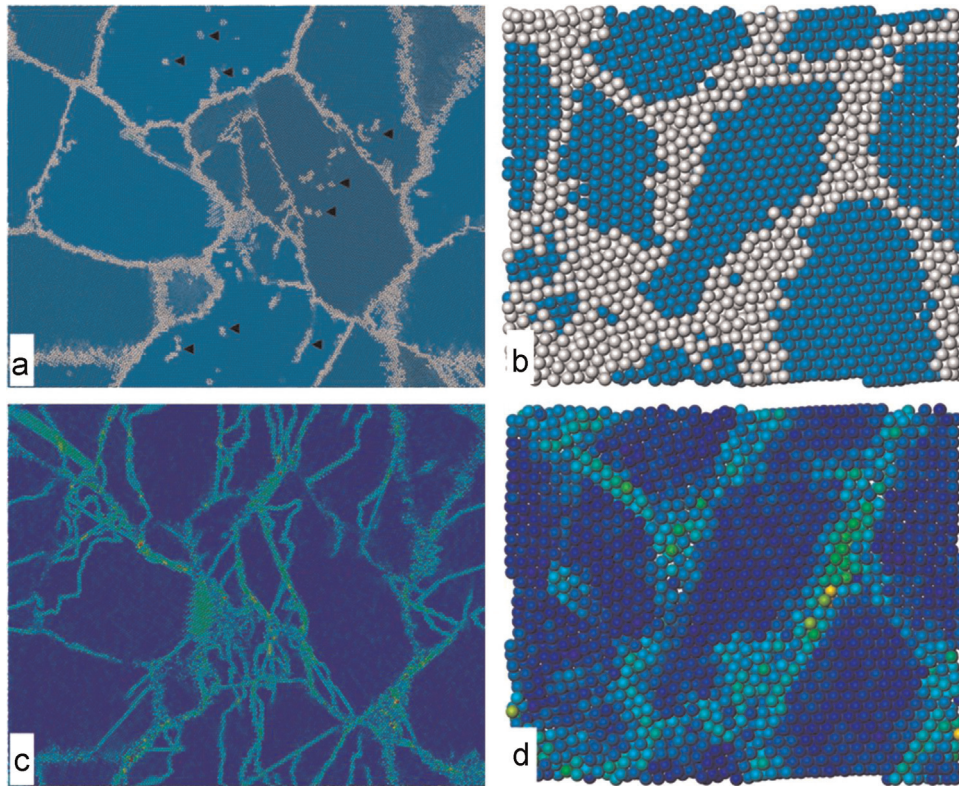
Fig. 39. Snapshots of nanocrystalline Fe colored by structure (a,b) and strain (c,d) with white corresponding to non-bcc atoms and green corresponding to highly strained atoms. Grain sizes are 19.7 nm and 3.7 nm and each are deformed to 15% strain. Dislocations are white clusters in the grain interiors marked by black triangles and are absent in the small grain size [160].

The relative quantity of studies is owed to a deficiency in interatomic potentials for use in molecular dynamics simulations. Zheng et al. [174] were among the first groups to investigate nanocrystalline cobalt of 10 nm grain size as fabricated by a kinetic Potts model through Monte Carlo simulation. In contrast to nanocrystalline FCC metals, both partial and dissociated dislocations were observed. Dissociated dislocations were shown to emit from both grain boundaries and from intragranular defects arising from interaction of stacking faults and disordered atom segments. Interaction of dislocations with disordered atom segments are shown in Fig. 6. Interaction between these two defects cause a split of the stacking fault with opposite leading partial dislocations [174]. Of further interest is the lack of twinning even at high stresses and the deformation-induced allotropic phase transformation to FCC Fig. 46.

In 2012, Song and Li [175] were the first to explore the effect of grain size on deformation of nanocrystalline HCP magnesium by using columnar grains. The turnover was found to be 22 nm for low temperatures and increased to approximately 30 nm for room temperature deformation. Fig. 47 shows the effect of grain size on the flow stress of magnesium, which has a c/a of 1.624 near to the theoretical value of 1.633. The inversion in the slope of the Hall-Petch slope is clear.

Following on this work, the IHP relationship was also shown in nanocrystalline zirconium by Ruestes et al. [176] for zirconium (c/a=1.593). MD simulations were carried out in the nanocrystalline region with columnar grains oriented in such a manner as to avoid twinning, which would bring another deformation mechanism. Thus, prismatic slip was activated in the system $< 11\text{-}20 > \{1\text{-}100\}$. The simulations were conducted at 5×10^8 s^{-1} and show an apex in strength at 30 nm. This confirmed experimental results by Wang et al.[177] which showed an inverse Hall-Petch relationship for a grain size below 30 nm. The flow stresses at 10 and 300 K are given in Fig. 48.

Fig. 49 shows snapshots at 300 K, 10% strain, strain rate 5×10^8 s^{-1}, hcp Zr for: (a) d=13 nm, (b) d=53 nm, (c) d=131 nm. The critical diameter for transition to an inverse Hall-Petch relationship is d_c=20 nm. Grayscale atoms are indicative of atomic displacements due to dislocation motion and reveal dislocation paths. Circular insets illustrate grain boundary sliding through the use of purple marker atoms (originally lying in a straight line in the undeformed state) and blue grain boundary atoms [176].

4.4. Extreme deformation of nanocrystalline metals

The response of nanocrystalline metals to laser shock has been investigated by our group and the findings are well matched by MD simulations because both the strain rate and grain sizes are comparable. The MD simulations are limited in time (picoseconds, while laser shock experiments are on the order of 1-3 ns. The strain rates in both experiments and simulations cover similar ranges: 10^7–10^9 s^{-1}. The grain sizes of the experimental nanocrystals (50–150 nm) are slightly larger than the simulated ones.

Two metals, Ni and Ta, representative of FCC and BCC structures respectively, were investigated. One of the outcomes of the work was to establish the effect of grain size on the pressure required to initiate twinning. A constitutive analysis developed by Meyers et al. [150] was applied to the slip-twinning transition. The basic assumption is that slip and twinning are competing mechanisms and that the shear stress for slip, τ_s equals the shear stress for twinning τ_T at the transition:

$$\tau_s = \tau_T \tag{26}$$

Converting into normal stresses:

$$\sigma_T \leq \sigma_s \tag{27}$$
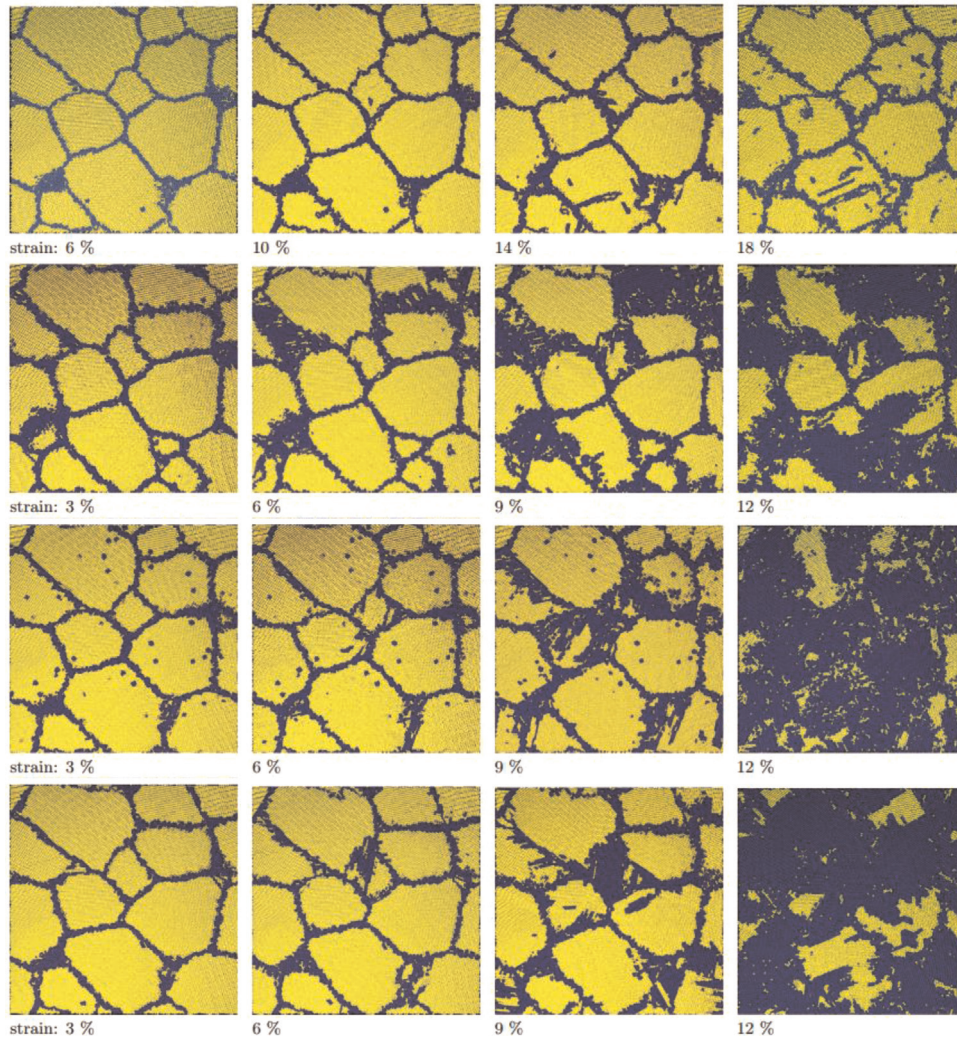
Fig. 40. Snapshots showing dislocation activity in nanocrystalline bcc Fe for varying potentials colored by structure as determined by CNA: yellow (bcc), blue (other, i.e. grain boundaries, defects, and non-bcc close-packed structures). From top to bottom the potentials are: Mendelev, MEAM-p, Ackland, Voter. Compressive strains increase as indicated from left to right [161].
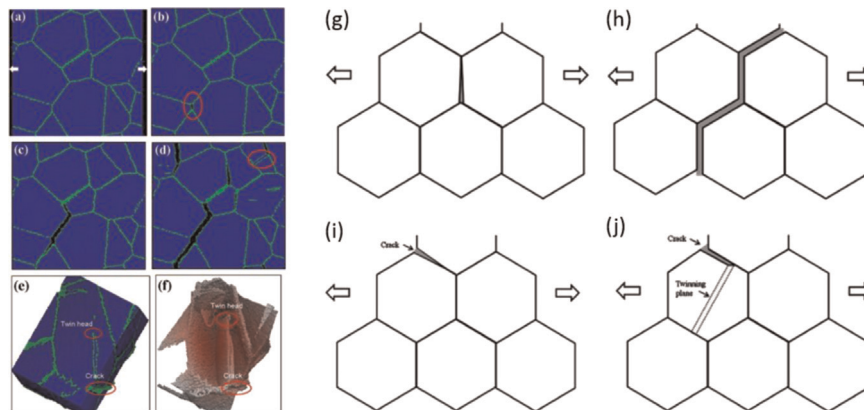
Fig. 41. (a-d) Evolution of failure in nanocrystalline BCC Ta. (e,f) Twin head and crack. (f) Only defective atoms are represented, showing a twin associated with crack opening. (g,h) Schematic of grain boundary separation and linkage of facet cracks. (i,j) Schematic of crack twin interaction. From Tang et al. [166].

There are many constitutive equations for slip, the best known being the Zerilli-Armstrong (ZA) [178,179], which has different forms for FCC and BCC structures. A Hall-Petch term was incorporated to represent the entire range of grain sizes, with a prefactor k_s. These equations were modified and applied by our group. For the FCC equation, a term was added to represent the strengthening due to the solid solution addition of W to Ni.

$$\sigma_{slip\ NiW13\%} = \sigma_G + \left(\sum_i K_i^{1/m} C_i \right)^m + C_2 \varepsilon^n \exp(-C_3 T + C_4 T \ln \dot{\varepsilon})$$
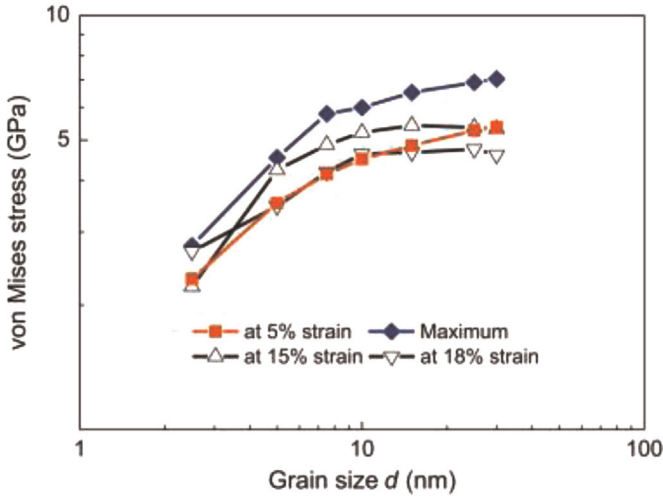$$+ k_S d^{-1/2} \tag{28}$$

Fig. 42. Maximum, 5%, 15% and 18% von Mises stress as a function of grain size d under uniaxial compressive strain (inverse Hall–Petch behavior); note decrease in slope as d increases (strain rate of $10^9 \, s^{-1}$). From Tang et al. [166].

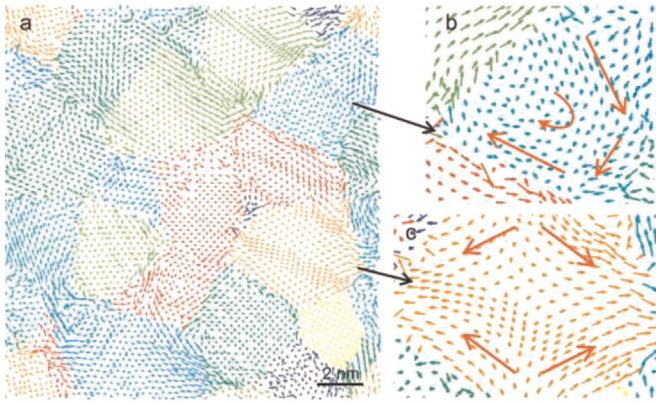**Fig. 43.** (a) Residual displacement field for bcc Ta; (b) grain rotation; (c) grain elongation [166].
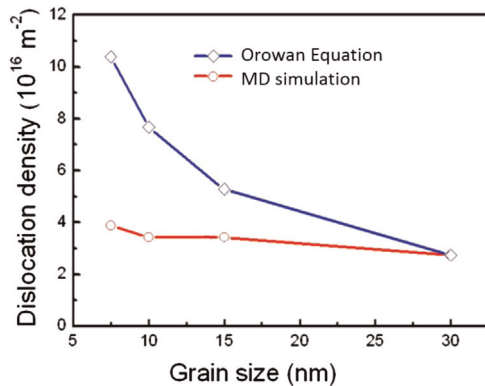

Fig. 44. Dislocation density (at a uniaxial strain of 0.18) as a function of grain size for tantalum predicted from Orowan equation and from MD simulation. Gap between the two consists of contribution from grain-boundary sliding [166].

The ZA equation has a number of parameters: C_2, n, C_3, C_4. The athermal component of stress in a monocrystal is σ_G. The contribution from solid solution strengthening by i solutes with concentration C_i each is represented by the second term in Equation 28.

For the BCC structure, Equation 29 was used. A pressure compensated term G/G_0 was added and the regime of drag controlled slip was added to the ZA equation. This was done according to the
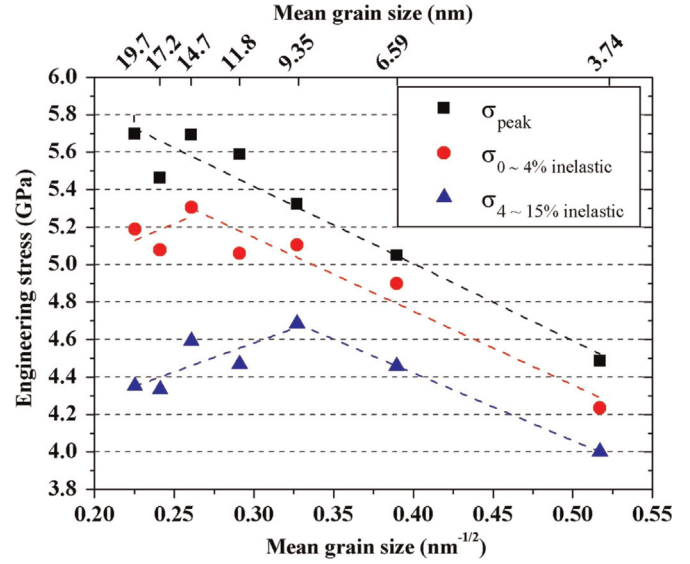

Fig. 45. Peak and average flow stresses as a function of grain size for nanocrystalline Fe.. Dashed lines are linear regression for each stress state [160].

Table 2
Strongest Grain Size from MD simulations and experimental results.

Metal	Apex (nm)	Ref.
Cu (FCC)	16	[53]
	20[a]	[13]
	15	[82]
Ni (FCC)	10	[246]
Mg (HCP)	30[b] 22[c]	[175]
Zr (HCP)	16[b]	[176]
	25[c]	
Zn (HCP)	11	[247]
Ta (BCC)	30	[166]
Fe (BCC)	15	[160]
WC (hex.)	15[a]	[248]

  [a] experimental result.
  [b] T = 300 K.
  [c] T = 10 K

Preston-Tonks-Wallace [180] constitutive equation.

$$\sigma_S = \max\left\{ \left(\sigma_S^* + C_2 e^{-C_3 T} \dot{\varepsilon}^{C_4 T} + k_S d^{-1/2}\right)\frac{G(\rho, T)}{G_0(\rho)}, \hat{\tau}_{drag}\right\} \qquad (29)$$

In order to predict the twinning stress, an athermal expression is often used, assuming that it is strain rate and temperature independent. The grain size dependence is introduced through a Hall-Petch term. The twinning stress is significantly affected by the stacking-fault energy γ_{SF} in FCC metals, and a term is added to the twinning equation:

$$\sigma_T = k_2\left(\frac{\gamma_{sfNiW-13\%}}{Gb}\right)^{1/2} + K_{T_{NiW}} d^{-1/2} \qquad (30)$$

where k_2 is a stacking fault energy parameter and k_T is the HP twinning prefactor.

Alternatively, Armstrong and Worthington [181] proposed an equation for twinning of the form:

$$\sigma_T = \sigma_0 + m\left[\frac{G(P, T)b}{C_1}\right]^{1/2}\left(\frac{U^*}{RT}\ln\frac{\dot{\varepsilon}}{\dot{\varepsilon}_0}\right)^{1/q} d^{-1/2} \qquad (31)$$

C_1, m, and q are parameters and U^* is an activation energy term. The parameter q is quite large, 5, and consequently the strain rate and temperature dependence of the twinning stress are low.
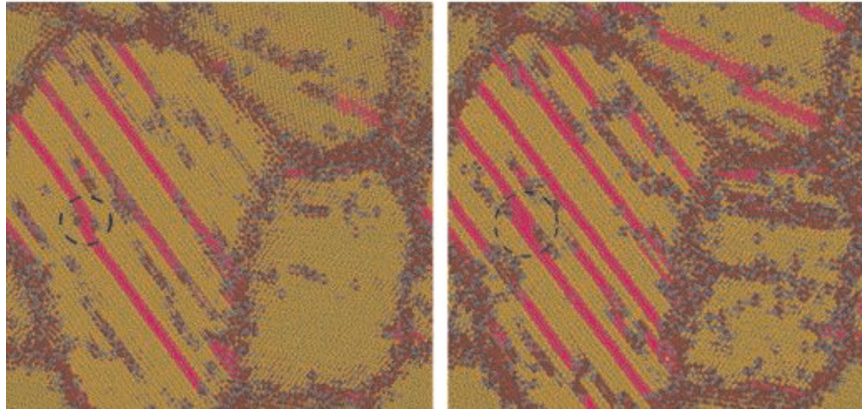
Fig. 46. Snapshot of nanocrystalline cobalt viewed in the (1210) plane at 9.2% and 11% strain. Atoms are colored according to structure type: hcp atoms (yellow); fcc atoms (pink); disordered atoms (red); other 12-coordinated atoms (grey). Interactions between disordered atom segments and stacking faults are circled. Interaction between these two defects cause a split of the stacking fault with opposite leading partial dislocations [174].
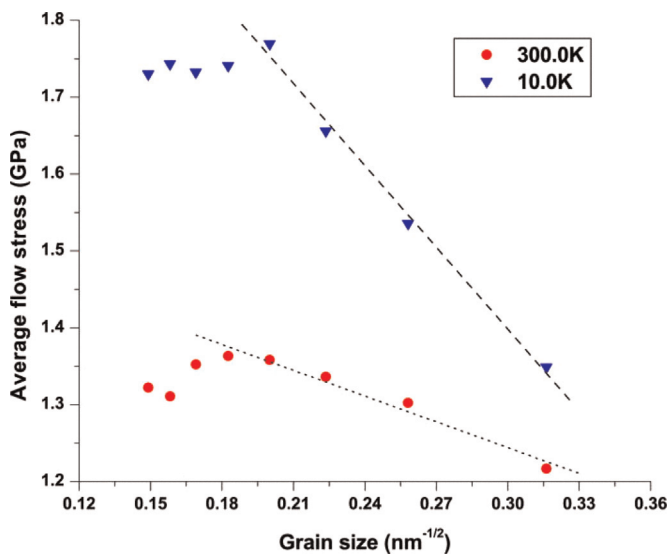

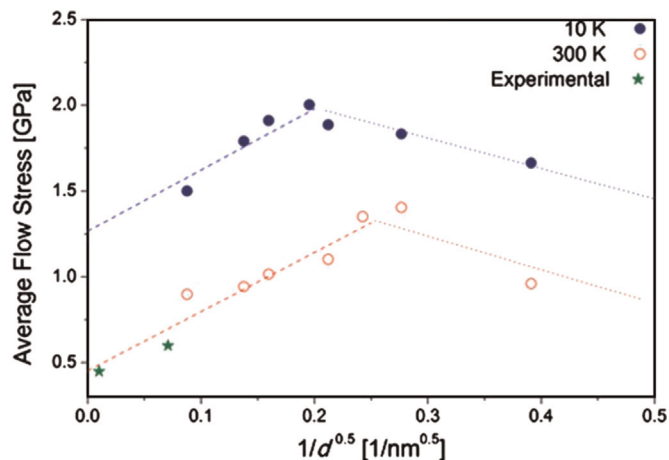**Fig. 47.** Average flow stress vs grain size (d$^{-1/2}$) for nanocrystalline Mg at 10 and 300 K [175].

Fig. 48. Average flow stresses as a function of d$^{-1/2}$ at 10 K and 300 K for six grain samples of HCP Zr [176]. Two green points represent experimental results.

An essential link in shock compression is provided by the Swegle–Grady [182] equation which relates the strain rate to the pressure. This equation is given below:

$$\frac{d\varepsilon}{dt} = k_{SG}P^4. \tag{31}$$

Application of Equations 28 and 30 to nanocrystalline Ni and Ni-13%W alloy leads to the predicted transition pressures shown in Fig. 50a,b, respectively. TEM observations confirm that, at 40 GPa, Ni does not twin but Ni13%W does. The lowering of the transition pressure for the alloy is the result of the decreased stacking fault energy, which decreases the twinning stress, and increased slip stress that results from solid solution strengthening. Consequently, the transition pressure is decreased from 78 to 15 GPa.

For tantalum, a model material for the BCC structure, similar calculations were performed for monocrystalline and nanocrystalline conditions, using Equations 29 and 31. The results shown in Fig. 51(a,b) show is a clear fashion that the twinning transition is highly dependent on grain size, being on the order of 150 GPa for the specimen with grain size of approximately 70 nm and equal to 24 GPa for the monocrystalline specimen. Accordingly, TEM observations, Fig. 51(c,d), show profuse twinning for the monocrystal and no twinning for the nanocrystalline condition. Fig. 52 summarizes the results of the calculations and illustrates the significant effect of grain size on the critical stress for twinning.

This is a direct result of the higher Hall-Petch slope for twinning than for slip. However, there are reports of observations of twins at very small grain sizes in aluminum (Ma and coworkers [148,158,183]). This is not predicted by the constitutive description presented here and can be the result of a separate regime. MD simulations also predict twinning at a grain size of 6.5 nm in tantalum [164], especially in grains of < 110 > orientation [170]. These twins are very thin, a few atomic layers and can result from peculiar nucleation sequences at the grain boundaries. Twins are also observed in the simulations reported by Yamakov et al. [184] and have been thoroughly reviewed by Zhu et al. [185].

4.5. On other technologically relevant materials

4.5.1. Diamond cubic silicon

Investigations of grain size effects in nanocrystalline silicon by Keblinski et al. [186] show that the Coble equation is validated. Demkowicz et al. [187] concluded that plasticity in nanocrystalline silicon occurs exclusively in intergranular regions characterized as amorphous silicon. This builds upon previous simulations of nanocrystalline silicon suggesting that the grain boundary character is amorphous-like [188]. Coordination in excess of 4 in
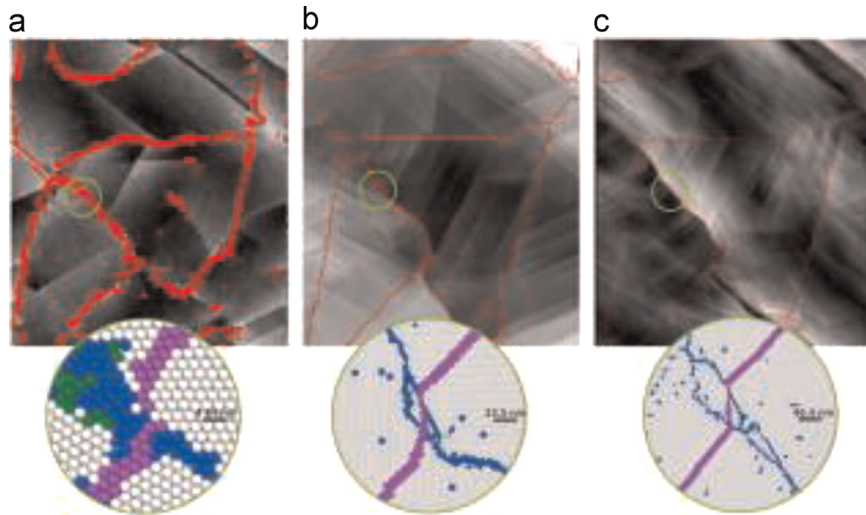
Fig. 49. Snapshots at 300 K, 10% strain, strain rate 5×10^8 s^{-1}, hcp Zr for: (a) d=13 nm, (b) d=53 nm, (c) d=131 nm. The critical diameter for transition to an inverse Hall-Petch relationship is d_c=20 nm. Grayscale atoms are indicative of atomi- displacements due to dislocation motion and reveal dislocation paths. Circular insets illustrate grain boundary sliding through the use of purple marker atoms (originally lying in a straight line in the undeformed state) and blue grain boundary atoms. [176].

diamond-cubic structures is analogous to liquid-like structures and have a more metallic like behavior. Fig. 53a shows nanocrystalline silicon at a strain of 0.08 indicating localization of plastic deformation along grain boundaries. Fig. 53b shows the deformation at a strain of 0.25 and black lines indicate channels of easy plastic flow. This plastic flow reaches a steady state where displacement occurs at a steady rate. The flow mediates grain rotation and deformation-induced formation of new grains.

4.5.2. Hexagonal carbon graphene

Practical applications of graphene sheets, or two dimensional hexagonal carbon, inherently introduce polycrystallinity during fabrication [189–191]. An understanding of how defects and grain boundaries operate within the graphene structure is of predominate importance considering that graphene is one of the strongest materials, if not the strongest known material [192]. Song et al. [193] identified a pseudo Hall-Petch effect in
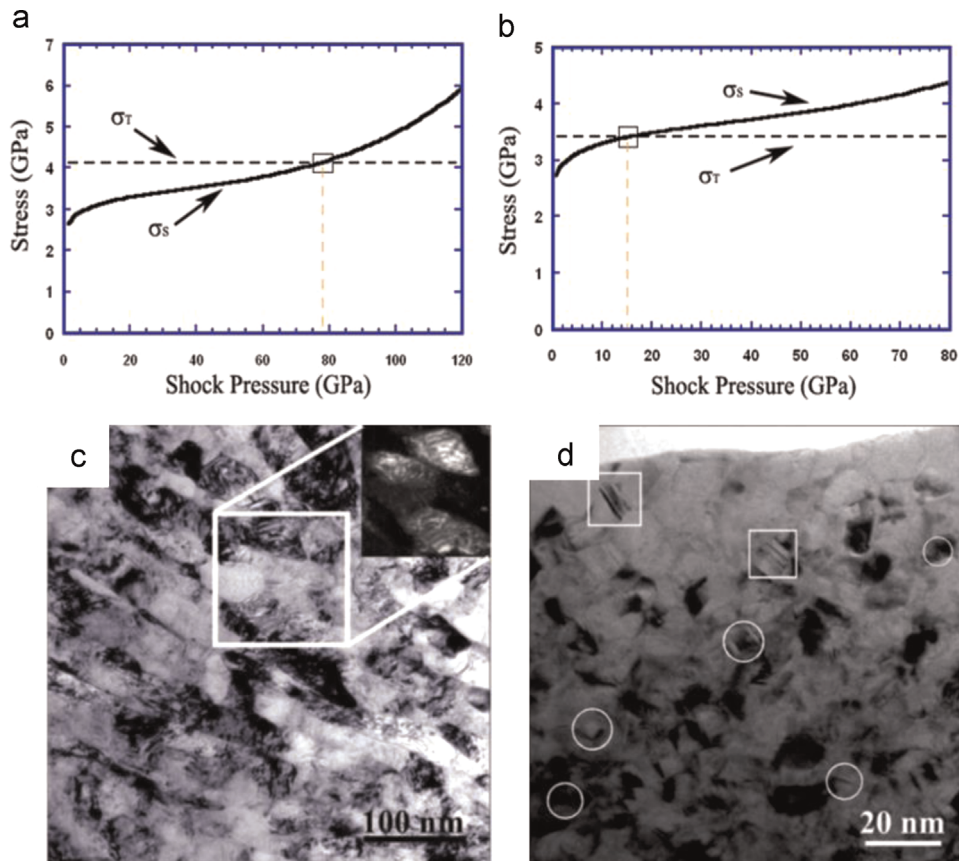
Fig. 50. Stresses for slip (σ_S) and twinning (σ_T) as a function of shock pressure for (a) Ni (d=50 nm) and (b) Ni-13%W (d=10 nm); (c) TEM showing dislocations in grains after 40 GPa pressure in Ni (d=30 nm); TEM showing twins (circled) after 40 GPa pressure in Ni-13% W (d=10 nm). (a, b from Jarmakani et al. [83]; c,d from Wang et al. [264]).
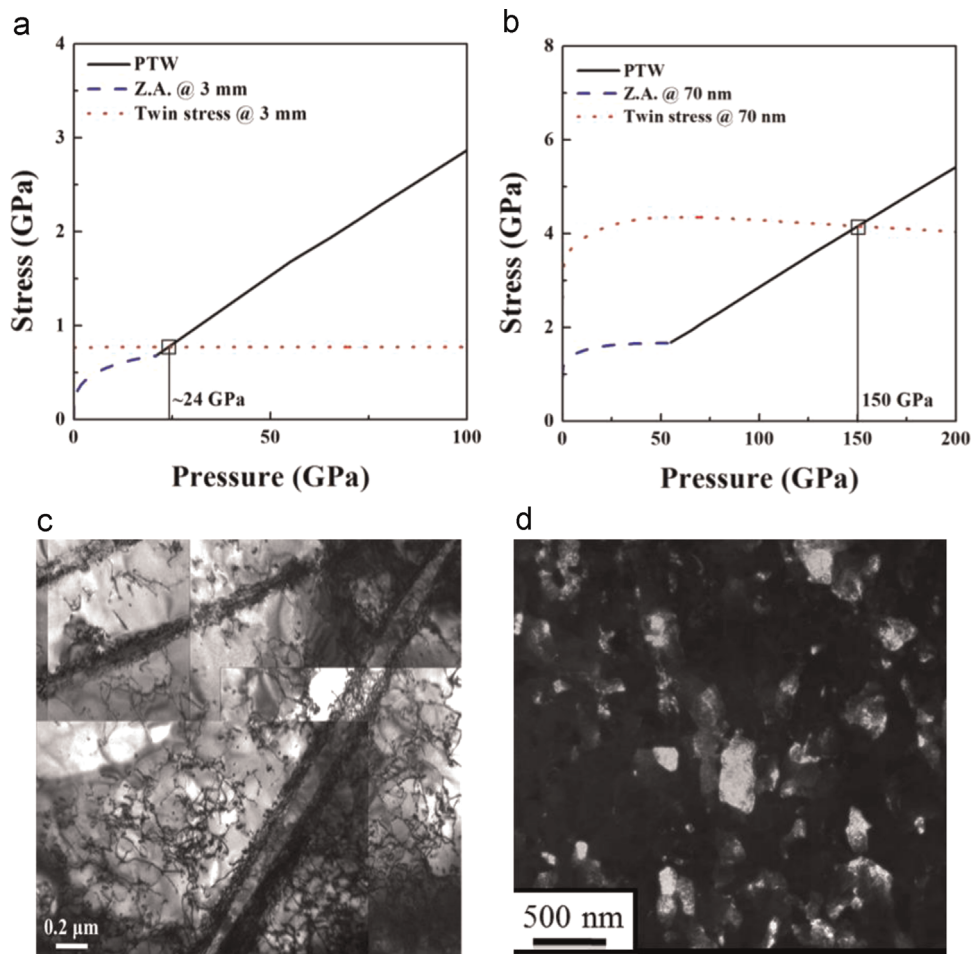
Fig. 51. Stresses for slip and twinning as a function of pressure for (a) monocrystalline (3 mm) and (b) ultrafine g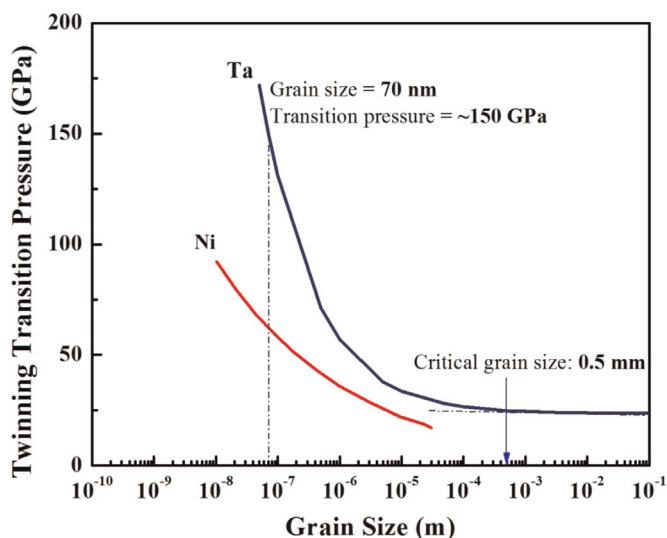rained tantalum (d=70 nm); (c) twins in monocrystalline Ta shocked at P= 40 GPa; (d) absence of twins in UFG Ta shocked at 40 GPa by lasers. From Lu et al. [265,266].


Fig. 52. Effect of grain size on the threshold pressure for twinning in shock compression. From Lu at al. [265].

polycrystalline graphene and shows this effect for the smallest grain sizes, but this work was recently called into question due to the "perfect" nature of the grain boundaries simulated. This effect is related to an investigation by Wei et al. [194], concluding that it is not the density of defects, nor the degree of GB tilt, that determine strength, but that the strength of tilt GBs increases as the square of tilt only if pentagon-heptagon defects are evenly spaced-in all other cases the trend fails. This is due to a build-up of stresses akin to dislocation pile-up.

Grantab et al. [195] showed that graphene sheets containing large-angle grain boundaries are stronger than those containing low-angle gain boundaries and, surprisingly, equivalent in strength to pristine graphene. This was quickly corroborated by Rasool et al. [196]. Other studies have introduced varying defects including Stone-Wales defects [197,198], hydrogenation [199,200] and notches [201]. Many seemingly concurrent research efforts were published on grain size dependent strength of graphene. An inverse type relation was first shown by Sha et al. [202] where the fracture strength was shown to be directly proportional to the density of grain boundary junctions for grain sizes up to 11 nm. Subsequent to Sha et al. [202], Mortazavi and Cuniverti [203] reported work detailing an inverse relationship of strength with grain size up to 10 nm. During the same time period, Li et al. [200] detailed an inverse strength relationship with grain size as well. Li et al. [200] also notably explored the role of hydrogenation identifying a drastic reduction in strength with increasingly hydrogenated grain boundary atoms. Fig. 54 shows a 2D Voronoi tessellation, hydrogenated grain boundary, characteristic out of plane buckling, and reduction of strength with increasing hydrogen percent.

Some extent of hydrogenation is expected during chemical vapor deposition growth. Chen et al. [204] published on grain size, temperature, and strain-rate effects indicating a larger strain rate effect at higher temperatures. Song et al. [193] showed that elastic modulus increased with grain size as was confirmed by others
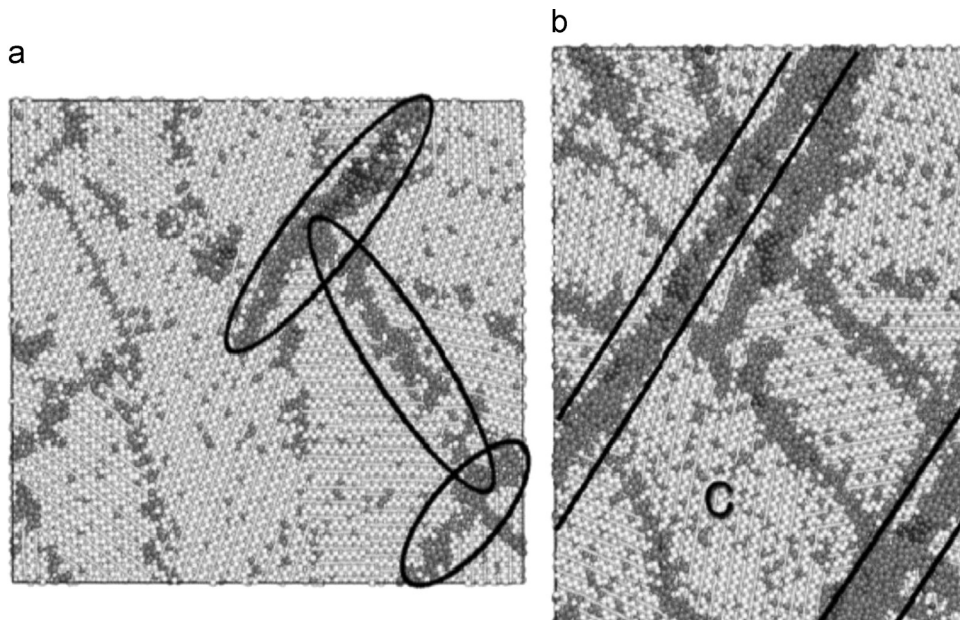
Fig. 53. Nanocrystalline silicon structure at deviatoric strains of (a) 0.08 and (b) 0.25. Dark atoms signify inelastic transformations, while light atoms are those that are purely elastic. Ellipses indicate intergranular regions of localized plastic deformation. Solid lines in (b) indicate fully developed plastic flow. "C" marks a grain that undergoes rotation during deformation. From Demkowicz et al. [187].

[202–204]. Li et al. [200] showed that Young's modulus decreased linearly with increasing hydrogen coverage.

## 5. Other computational tools

5.1. Finite element method

The Finite Element Method (FEM) is limited in its ability to interrogate the response of materials at the atomic/molecular scale. Nevertheless, the effect of grain size has been investigated by introducing an artificial length scale. A short review of composite methods is presented by Mishnaevsky and Levashov [205]. Importantly, FEM predicts correctly the internal stresses due to compatibility requirements. As early as 1980, Meyers and Ashworth [9] juxtaposed two grains with different orientations by transforming the stiffness matrix into equivalent elastic moduli. This was done for three orientations:[100], [110], and [111]. Later analysis by Fu et al. [206] on a polycrystalline aggregate, also using FEM, produced the results shown in Fig. 55. These results are analogous to the ones obtained by MD and shown in Fig. 21. In

order to produce a grain size dependence of flow stress, Fu et al. [206] considered grains as composed of two regions: grain interiors and grain-boundary layers. As the grain size was varied, the volume fractions of the two regions changed and the mechanical response was altered, resulting in a Hall-Petch response but with a decreasing slope as the size decreased. This was later changed into a gradient of strains, which is size dependent.

5.2. Quasi-continuum methods

Quasi-continuum (QC) methods are methods of mixed atomistic (namely MD) and continuum (namely FEM) approaches where fully-atomistic techniques are implemented in areas of direct interest and remote areas are modeled using less costly continuum mechanics. Tadmor and Miller [207] provide a thorough description of QC techniques in their recent book (in addition to continuum mechanics, quantum mechanics, atomistic simulations, and multi-scale techniques). This method is particularly appropriate for the representation of polycrystalline materials where full atomistic resolution is too costly and continuum methods do not
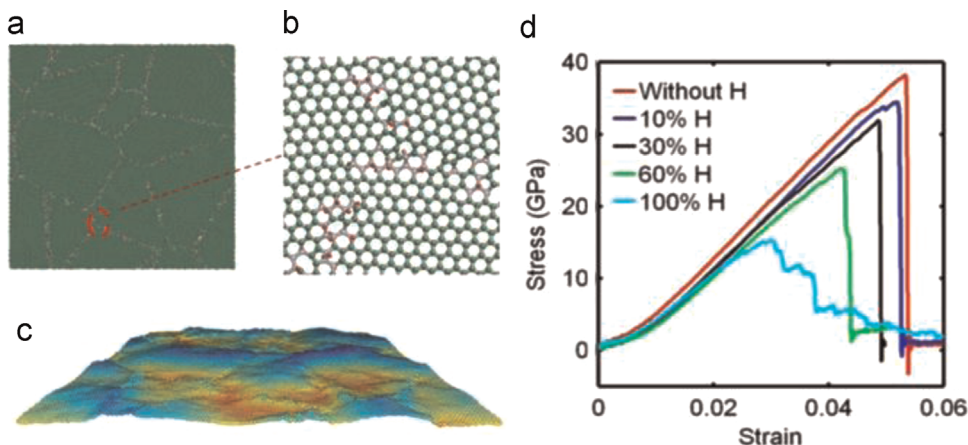
Fig. 54. (a) 2D Voronoi tessellation of graphene with 30% hydrogen grain boundary coverage indicated by red atoms in (b). (c) Represents characteristic out of plane buckling colored by out of plane displacement. (d) Effect of hydrogen content on failure strength. From Li et al. [200].
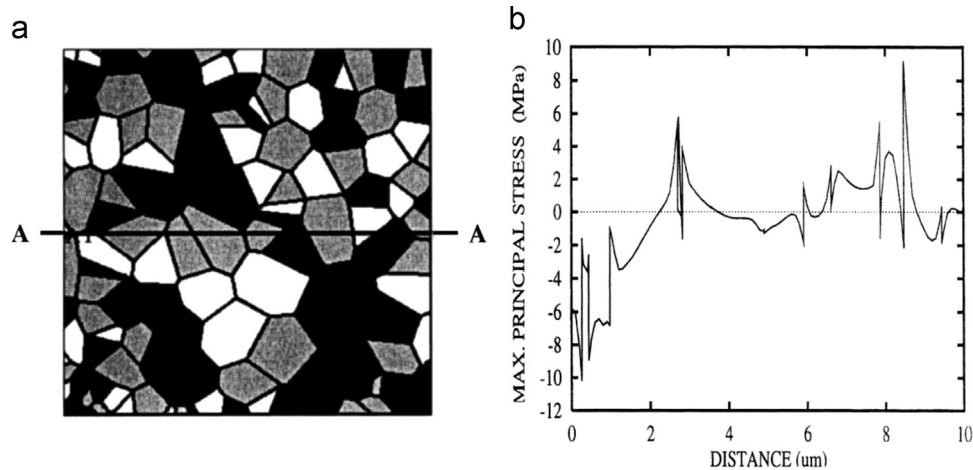
Fig. 55. Stresses in polycrystalline copper loaded elastically; (a) grain configuration; three grain orientations: white [100], gray [110], and black [111]; (b) maximum principal stress (σ_1). From Fu et al.[206].

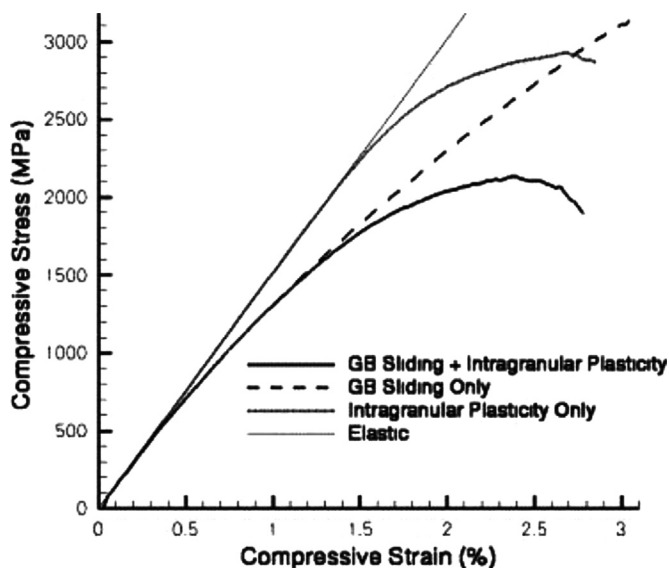**Fig. 56.** Quasi-continuum modeling predicting stress–strain response of 10 nm nanocrystalline copper with different deformation mechanisms. The combination of grain-boundary sliding and intra grain plasticity provides the lowest curve. From Warner et al. [212].

accurately describe the intricacies of grain boundary phenomenon. The outstanding challenge has been by what means these two methodologies are directly coupled. This has seen difficulty in complexity and cost to implement as well as a sacrifice in accuracy at the "boundary" between methods arising from errors in equating compatibility. The preeminent solution has been a gradual coarse graining method by which representative atoms transition from including 1 atom to many. This type of formalism can be seen in the work of [208] based on the framework of Knap and Ortiz [209]. The fallback of this type of methodology is the time of implementation to new scenarios and synthetic selection of areas of importance.

A few coarse-grained simulations of grain-boundary dependent strength stand out, namely work by Sansoz and Molinari [210,211] and Warner et al. [212] (implementing an approach where coarse-grain simulations inform FEM). Their method does not simply use two distinct "phases", owing to the fact that crystallinity of nanometer sized grains is maintained completely up to the grain boundary, and is instead similar to simulations by Wei and Anand [213] whom use cohesive elements to describe the grain boundary. The results from their calculation are shown in Fig. 56. By tuning

deformation mechanisms they were able to observe the correct behavior (solid black line) by the combination of grain boundary sliding and intergranular plasticity.

Much of the advancements in applicability of coarse graining molecular dynamics arise from the ability to adjust the degree of coarse-graining on the fly. This technique is referred to as adaptive coarse-graining and has recently been implemented by Amelang and Kochmann [214] (using previously defined fully-nonlocal energy based QC methods [215]) for evaluating nanostructures where free surfaces contribute significantly to mechanical behavior. One key aspect of adaptivity is the ability to reduce full atomistic resolution to only where it is required. It is expected that this technique will transition well to nanocrystalline materials and expedite arrival of larger and larger grain sizes by simulation.

6. Summary and conclusions

1. The grain sizes of metals are classified into three regions: conventional or microcrystalline (greater than 1 μm); ultrafine grained (between 1 μm and 100 nm) and nanocrystalline (smaller than 100 nm)[10].
2. As the grain size is reduced from the microcrystalline to the ultrafine grained and nanocrystalline size the slope of the Hall-Petch equation decreases, as was pointed out in 1982 by Meyers and Ashworth [9].
3. There is a critical grain size, termed the 'strongest size', at which the hall-Petch slope turns over and becomes negative [36].
4. This negative Hall-Petch relationship was discovered by Chokshi et al. [12] in 1989 and the effect was attributed to Coble creep.
5. Analytical models by Conrad and Narayan [34] in 2000 and Argon and Yip [36] in 2006 address the two regimes of plastic deformation, grain-boundary shear and dislocation movement, and correctly predict the 'strongest size' at which the two responses intersect.
6. Molecular dynamics (MD) simulations are a powerful tool for understanding the mechanical response of metals in the nanocrystalline region.
7. The current upper limit of grain sized tractable as polycrystals in MD simulations is ~50 nm (box size of ~200 nm). However, increased computational capability is expanding this region, with the limitation that computational time increases (at least) with the cube of grain size.

8. MD simulations enable the observation of dislocation and twinning evolution by filtering techniques that retain only the atoms in defective regions for visualization. Many techniques have been developed and methods such as common neighbor analysis and the dislocation extraction algorithm have greatly enhanced our ability to diagnose nanoscale systems.

9. MD simulation relies heavily on the potentials used to represent the interatomic forces. For FCC structures, the simpler potentials are more robust owing to nearly-spherical electron shells. In BCC structures, d and f orbitals cause non-symmetric effects that often require more complex potentials.

10. One limitation of MD simulations is that the time scale is extremely small, since they have to track the movement of atoms at their natural frequencies of 10^{13} s^{-1}. The lowest strain rates achievable for a respectable simulation size are on the order of 10^{6}s^{-1}, corresponding to 10^7 vibrations. In conventional deformation, on the other hand, the strain rates are in the 10^{-4}-10^{-1} s^{-1} range.

11. In the nanocrystalline region, Swygenhoven et al. [131] first demonstrated in 2006 that dislocations are generated in a grain boundary, travel across the grain as separate leading and trailing partials linked by a stacking fault, and penetrate into the opposing grain boundary, being annihilated in the process.

12. As the grain size is decreased below 20 nm, MD simulations by Schiotz et al. [216] in 2003 first showed that a maximum in strength is reached, followed by a decrease in flow stress. This was attributed to grain-boundary shear and was later shown by Wolf et al. [16] to be a combined contribution of grain-boundary slip and Coble creep, reconciling the two proposals.

13. Although other computational techniques have been used to simulate the nanocrystalline regime (such as Finite Element and quasi-continuum methods) they are limited. FEM does not have a length scale, which has to be artificially introduced. This was successfully done by Fu et al. [206] considering a strain gradient term. The FEM and QC methods are limited in their ability to predict and visualize dislocation densities and incorporate strain rate and thermal effects.

14. The next frontier in simulations is multi-scale modeling intelligently compiled and implemented into parallel computer architectures. This starts with ab-initio calculations, and proceeds with molecular dynamics and its expanded capability by adaptive coarse-graining. Phase field and dislocation dynamics calculations occur at a larger temporal scales. At larger temporal and spatial scales continuum-scale models with physically-based constitutive equations provide the representation. These approaches will incorporate deformation processes and features including solute atoms, precipitates, phase transitions, and multi-phase structures. This poses formidable computational and conceptual challenges.

Acknowledgements

References

[1] E.O. Hall, Proc. Phys.. Soc. Sect. B 64 (1951) 747.
[2] N.J. Petch, J. Iron Steel Inst. 174 (1953) 25.
[3] R.W. Armstrong, Mater. Trans. 55 (2014) 2.
[4] J.C.M. Li, Mechanical Properties of Nanocrystalline Materials, CRC Press, 2011.
[5] J.D. Embury, R.M. Fisher, Acta Metall. 14 (1966) 147.
[6] J.S.C. Jang, C.C. Koch, Scr. Metall. Mater. 24 (1990) 1599.
[7] E. Abrahamson, Surfaces and Interfaces II, Syracuse University Press, Syracuse (1968), p. 262.
[8] T.R. Malow, C.C. Koch, Acta Mater. 46 (1998) 6459.
[9] M.A. Meyers, E. Ashworth, Philos. Mag. A 46 (1982) 737.
[10] H. Gleiter, Prog. Mater. Sci. 33 (1989) 223.
[11] H. Gleiter, Deformation of Polycrystals: Mechanisms and Microstructures, 1981.
[12] A.H. Chokshi, A. Rosen, J. Karch, H. Gleiter, Scr. Metall. 23 (1989) 1679.
[13] M.A. Meyers, A. Mishra, D.J. Benson, Prog. Mater. Sci. 51 (2006) 427.
[14] C.C.Koch, J.Narayan, in:, SymposiumB – Structure and Mechanical Properties of Nanophase Materials – Theory and Computational Simulations vs Experiment, 2000.
[15] T.G. Nieh, J. Wadsworth, Scr. Metall. Mater. 25 (1991) 955.
[16] D. Wolf, V. Yamakov, S.R. Phillpot, A.K. Mukherjee, Z. Für Met. 94 (2003) 1091.
[17] M.A. Tschopp, H.A. Murdoch, L.J. Kecskes, K.A. Darling, J. Miner., Met. Mater. 66 (2014) 1000.
[18] K. Lu, Mater. Sci. Eng. R. Rep. 16 (1996) 161.
[19] C. Suryanarayana, Prog. Mater. Sci. 46 (2001) 1.
[20] R. Valiev, Nat. Mater. 3 (2004) 511.
[21] Y. Estrin, A. Vinogradov, Acta Mater. 61 (2013) 782.
[22] U. Erb, Nanostruct. Mater. 6 (1995) 533.
[23] D. Wolf, V. Yamakov, S.R. Phillpot, A. Mukherjee, H. Gleiter, Acta Mater. 53 (2005) 1.
[24] N.R. Barton, J.V. Bernier, R. Becker, A. Arsenlis, R. Cavallo, J. Marian, M. Rhee, H.-S. Park, B.A. Remington, R.T. Olson, J. Appl. Phys. 109 (2011) 073501.
[25] S. Benkassem, L. Capolungo, M. Cherkaoui, Acta Mater. 55 (2007) 3563.
[26] L. Capolungo, D.E. Spearot, M. Cherkaoui, D.L. McDowell, J. Qu, K.I. Jacob, J. Mech. Phys. Solids 55 (2007) 2300.
[27] J. Hafner, Acta Mater. 48 (2000) 71.
[28] T.E. Karakasidis, C.A. Charitidis, Mater. Sci. Eng. C 27 (2007) 1082.
[29] V. Péron-Lührs, A. Jérusalem, F. Sansoz, L. Stainier, L. Noels, J. Mech. Phys. Solids 61 (2013) 1895.
[30] Handbook of Materials Modeling, in: S. Yip (Ed.), Springer, Netherlands, Dordrecht, 2005.
[31] A.M. Cuitiño, L. Stainier, G. Wang, A. Strachan, T. Çağin, W.A.G. Iii, M. Ortiz, J. Comput. – Aided Mater. Des. 8 (2001) 127.
[32] G. Gottstein (Ed.), Integral Materials Modeling, Wiley-VCH Verlag GmbH & Co. KGaA, 2007.
[33] T.M. Pollock, R. LeSar, Curr. Opin. Solid State Mater. Sci. 17 (2013) 10.
[34] H. Conrad, J. Narayan, Scr. Mater. 42 (2000) 1025.
[35] H. Conrad, J. Narayan, Appl. Phys. Lett. 81 (2002) 2241.
[36] A.S. Argon, S. Yip, Philos. Mag. Lett. 86 (2006) 713.
[37] R.J. Asaro, S. Suresh, Acta Mater. 53 (2005) 3369.
[38] M.F. Ashby, Philos. Mag. 21 (1970) 399.
[39] S.K. Bhattacharya, S. Tanaka, Y. Shiihara, M. Kohyama, J. Phys. Condens. Matter 25 (2013) 135004.
[40] D. Terentyev, X. He, A. Serra, J. Kuriplach, Comput. Mater. Sci. 49 (2010) 419.
[41] G. Gottstein, L.S. Shvindlerman, Grain Boundary Migration in Metals: Thermodynamics, Kinetics, Applications, CRC Press, 1999.
[42] D.E. Spearot, M.A. Tschopp, K.I. Jacob, D.L. McDowell, Acta Mater. 55 (2007) 705.
[43] M. Koiwa, H. Seyazaki, T. Ogura, Acta Metall. 32 (1984) 171.
[44] A.P. Sutton, V. Vitek, Philos. Trans. R. Soc. Lond. Ser. Math. Phys. Sci. 309 (1983) 1.
[45] A.P. Sutton, R.W. Balluffi, Philos. Mag. Lett. 61 (1990) 91.
[46] S.J. Fensin, E.K. Cerreta, G.T.G. Iii, S.M. Valone, Sci. Rep. 4 (2014).
[47] S.J. Fensin, S.M. Valone, E.K. Cerreta, J.P. Escobedo-Diaz, G.T.G. Iii, K. Kang, J. Wang, Model. Simul. Mater. Sci. Eng. 21 (2013) 015011.
[48] S.J. Fensin, C. Brandl, E.K. Cerreta, G.T. Gray, T.C. Germann, S.M. Valone, J. Miner., Met. Mater. 65 (2013) 410.
[49] J. Bian, X. Niu, H. Zhang, G. Wang, Nanoscale Res. Lett. 9 (2014) 1.
[50] S.J. Fensin, S.M. Valone, E.K. Cerreta, G.T.G. Iii, J. Appl. Phys. 112 (2012) 083529.
[51] S.-N. Luo, T.C. Germann, D.L. Tonks, Q. An, J. Appl. Phys. 108 (2010) 093526.
[52] D.E. Spearot, K.I. Jacob, D.L. McDowell, Acta Mater. 53 (2005) 3579.
[53] D.E. Spearot, D.L. McDowell, J. Eng. Mater. Technol. 131 (2009) 041204.
[54] D.L. Zheng, S.D. Chen, A.K. Soh, Y. Ma, Comput. Mater. Sci. 48 (2010) 551.
[55] A. Hasnaoui, P.M. Derlet, H. Van Swygenhoven, Acta Mater. 52 (2004) 2251.
[56] J.D. Eshelby, F.C. Frank, F.R.N. Nabarro, Lond., Edinb. Dublin Philos. Mag. J. Sci. 42 (1951) 351.
[57] V.A. Lubarda, J.A. Blume, A. Needleman, Acta Metall. Mater. 41 (1993) 625.
[58] J. Schiøtz, Scr. Mater. 51 (2004) 837.
[59] G. Szegš, Orthogonal Polynomials, American Mathematical Soc., 1939.
[60] A.H. Cottrell, Lond., Edinb. Dublin Philos. Mag. J. Sci 44 (1953) 829.
[61] J.C. Li, Trans. Metall. Soc. AIME 227 (1963) 239.
[62] L.E. Murr, Metall. Trans. A 6 (1975) 505.

[63] H. Van Swygenhoven, M. Spaczer, A. Caro, D. Farkas, Phys. Rev. B 60 (1999) 22.
[64] V. Yamakov, D. Wolf, M. Salazar, S.R. Phillpot, H. Gleiter, Acta Mater. 49 (2001) 2713.
[65] D.E. Spearot, K.I. Jacob, D.L. McDowell, Int. J. Plast. 23 (2007) 143.
[66] C.D. Barrett, H. El Kadiri, Acta Mater. 63 (2014) 1.
[67] W.M. Baldwin Jr., Acta Metall. 6 (1958) 139.
[68] D.J. Dunstan, A.J. Bushby, Int. J. Plast. 53 (2014) 56.
[69] M.A. Meyers, K.K. Chawla, Mechanical Behavior of Materials, Cambridge University Press, 2009.
[70] M.A. Tschopp, G.J. Tucker, D.L. McDowell, Acta Mater. 55 (2007) 3959.
[71] G.J. Tucker, M.A. Tschopp, D.L. McDowell, Acta Mater. 58 (2010) 6464.
[72] E.-M. Steyskal, B. Oberdorfer, W. Sprengel, M. Zehetbauer, R. Pippan, R. Würschum, Phys. Rev. Lett. 108 (2012) 055504.
[73] B. Oberdorfer, D. Setman, E.-M. Steyskal, A. Hohenwarter, W. Sprengel, M. Zehetbauer, R. Pippan, R. Würschum, Acta Mater. 68 (2014) 189.
[74] P.G. Sanders, J.A. Eastman, J.R. Weertman, Acta Mater. 45 (1997) 4019.
[75] J.C.M. Li, Appl. Phys. Lett. 90 (2007) 041912.
[76] C.E. Carlton, P.J. Ferreira, Acta Mater. 55 (2007) 3749.
[77] X.L. Wu, Y.T. Zhu, Y.G. Wei, Q. Wei, Phys. Rev. Lett. 103 (2009) 205504.
[78] L. Wang, J. Teng, P. Liu, A. Hirata, E. Ma, Z. Zhang, M. Chen, X. Han, Nat. Commun. 5 (2014).
[79] H. Van Swygenhoven, P.M. Derlet, Phys. Rev. B 64 (2001) 224105.
[80] H. Conrad, Mater. Sci. Eng. A 341 (2003) 216.
[81] L. Kubin, Dislocations, Mesoscale Simulations and Plastic Flow, OUP, Oxford, 2013.
[82] J. Schiøtz, K.W. Jacobsen, Science 301 (2003) 1357.
[83] H.N. Jarmakani, E.M. Bringa, P. Erhart, B.A. Remington, Y.M. Wang, N.Q. Vo, M. A. Meyers, Acta Mater. 56 (2008) 5584.
[84] D. Farkas, Curr. Opin. Solid State Mater. Sci. 17 (2013) 284.
[85] T.C. GERMANN, K. KADAU, Int. J. Mod. Phys. C 19 (2008) 1315.
[86] J. Milhans, J.E. Hammerberg, R. Ravelo, T.C. Germann, B.L. Holian, APS Meet. Abstr. (2012) 26006.
[87] M.P. Allen, D.J. Tildesley, Computer Simulation of Liquids, Oxford University Press, 1989.
[88] D.C. Rapaport, The Art of Molecular Dynamics Simulation, Cambridge University Press, 2004.
[89] J. Hirth, J. Lothe, Theory of Dislocations, John Wiley & Sons, 1982.
[90] D. Hull, D.J. Bacon, Introduction to Dislocations, Elsevier, 2011.
[91] P. m Derlet, P. Gumbsch, R. Hoagland, J. Li, D. l McDowell, H. Van Swygenhoven, J. Wang, MRS Bull. 34 (2009) 184.
[92] Hirth Swygenhoven, Dislocations in Solids: A Tribute to F.R.N. Nabarro, Elsevier, 2011.
[93] V. Bulatov, W. Cai, Computer Simulations of Dislocations, Oxford University Press, 2006.
[94] S.J. Plimpton, J.D. Gale, Curr. Opin. Solid State Mater. Sci. 17 (2013) 271.
[95] S. Plimpton, J. Comput. Phys. 117 (1995) 1.
[96] A. Stukowski, J. Miner. Met. Mater. 66 (2013) 399.
[97] C.L. Kelchner, S.J. Plimpton, J.C. Hamilton, Phys. Rev. B 58 (1998) 11085.
[98] S. Plimpton, A.P. Thompson, P. Crozier, A. Kohlmeyer, LAMMPS Molecular Dynamics Simulator, n.d. (Computer Program), http://lammps.sandia.gov/.
[99] A. Stukowski, Model. Simul. Mater. Sci. 20 (2012) 045021.
[100] J.D. Honeycutt, H.C. Andersen, J. Phys. Chem. 91 (1987) 4950.
[101] D. Faken, H. Jónsson, Comput. Mater. Sci. 2 (1994) 279.
[102] H. Tsuzuki, P.S. Branicio, J.P. Rino, Comput. Phys. Commun. 177 (2007) 518.
[103] G.J. Ackland, A.P. Jones, Phys. Rev. B 73 (2006) 054104.
[104] K. Albe Alexander, Model. Simul. Mater. Sci. Eng. 18 (2010) 025016.
[105] A. Stukowski, Model. Simul. Mater. Sci. Eng. 18 (2010) 015012.
[106] C.J. Ruestes, E.M. Bringa, A. Stukowski, J.F. Rodríguez Nieva, Y. Tang, M. A. Meyers, Comput. Mater. Sci. 88 (2014) 92.
[107] R.E. Rudd, Mater. Sci. Forum 633–634 (2009) 3.
[108] R. Ravelo, T.C. Germann, O. Guerrero, Q. An, B.L. Holian, Phys. Rev. B 88 (2013) 134101.
[109] R.E. Rudd, Plasticity and Failure in Nanocrystalline BCC Metals via Molecular Dynamics Simulation, Lawrence Livermore National Lab., Livermore, CA (United States), Funding organisation: US Department of Energy (United States), 2010.
[110] L. Wang, J.C. E, Y. Cai, F. Zhao, D. Fan, S.N. Luo, J. Appl. Phys., 117, (2015) 084301.
[111] M.S. Daw, M.I. Baskes, Phys. Rev. B 29 (1984) 6443.
[112] S.M. Foiles, M.I. Baskes, MRS Bull. 37 (2012) 485.
[113] S.M. Foiles, MRS Bull. 21 (1996) 24.
[114] M.I. Baskes, Phys. Rev. B 46 (1992) 2727.
[115] M. w Finnis, MRS Bull. 37 (2012) 477.
[116] S.J. Plimpton, A.P. Thompson, MRS Bull. 37 (2012) 513.
[117] N.US Department of Commerce, n.d..
[118] H.W. Sheng, M.J. Kramer, A. Cadien, T. Fujita, M.W. Chen, Phys. Rev. B 83 (2011) 134118.
[119] D.S. Ivanov, Z. Lin, B. Rethfeld, G.M. O'Connor, T.J. Glynn, L.V. Zhigilei, J. Appl. Phys. 107 (2010) 013519.
[120] Y.-B. Guo, T. Xu, M. Li, Philos. Mag. 92 (2012) 3064.
[121] T. Xu, M. Li, Philos. Mag. 90 (2010) 2191.
[122] M. Li, T. Xu, Prog. Mater. Sci. 56 (2011) 864.
[123] S. Jolles, J. Für Reine, Angew. Math. 134 (1908) 1.
[124] D. Farkas, E. Bringa, A. Caro, Phys. Rev. B 75 (2007) 184111.
[125] E.M. Bringa, D. Farkas, A. Caro, Y.M. Wang, J. McNaney, R. Smith, Scr. Mater. 59 (2008) 1267.
[126] Y.T. Zhu, X.Z. Liao, R.Z. Valiev, Appl. Phys. Lett. 86 (2005) 103112.
[127] Y. Pan, B.L. Adams, Scr. Metall. Mater. 30 (1994) 1055.
[128] A.G. Frøseth, H. Van Swygenhoven, P.M. Derlet, Acta Mater. 53 (2005) 4847.
[129] M.A. Groeber, M.A. Jackson, Integr. Mater. Manuf. Innov. 3 (2014) 5.
[130] H. Van Swygenhoven, M. Spaczer, A. Caro, Acta Mater. 47 (1999) 3117.
[131] H. Van Swygenhoven, P.M. Derlet, A.G. Derlet, A.G. Frøseth, Acta Mater. 54 (2006) 1975.
[132] M. Chen, E. Ma, K.J. Hemker, H. Sheng, Y. Wang, X. Cheng, Science 300 (2003) 1275.
[133] X.Z. Liao, Y.H. Zhao, S.G. Srinivasan, Y.T. Zhu, R.Z. Valiev, D.V. Gunderov, Appl. Phys. Lett. 84 (2004) 592.
[134] D. Moldovan, D. Wolf, S.R. Phillpot, A.J. Haslam, Acta Mater. 50 (2002) 3397.
[135] A.J. Haslam, D. Moldovan, S.R. Phillpot, D. Wolf, H. Gleiter, Comput. Mater. Sci. 23 (2002) 15.
[136] Z.T. Trautt, Y. Mishin, Acta Mater. 60 (2012) 2407.
[137] J.W. Cahn, J.E. Taylor, Acta Mater. 52 (2004) 4887.
[138] H. Zhang, D. Du, D.J. Srolovitz, Philos. Mag. 88 (2008) 243.
[139] E. Bitzek, C. Brandl, P.M. Derlet, H. Van Swygenhoven, Phys. Rev. Lett. 100 (2008) 235501.
[140] G.I. Taylor, R. Proc., Soc. Lond. Ser. Contain. Pap. Math. Phys. Character 146 (1934) 501.
[141] A. Seeger, Lond Edinb, Dublin Philos. Mag. J. Sci. 45 (1954) 771.
[142] P. Hirsch, Discuss Faraday Soc. 38 (1964) 111.
[143] P.B. Hirsch, R.W. Horne, M.J. Whelan, Philos. Mag. 1 (1956) 677.
[144] D. Kuhlmann-Wilsdorf, Mater. Sci. Eng. A 113 (1989) 1.
[145] K. Lu, L. Lu, S. Suresh, Science 324 (2009) 349.
[146] C. Brandl, P.M. Derlet, H. Van Swygenhoven, Philos. Mag. 89 (2009) 3465.
[147] N.Q. Vo, R.S. Averback, P. Bellon, S. Odunuga, A. Caro, Phys. Rev. B 77 (2008) 134108.
[148] X.Z. Liao, F. Zhou, E.J. Lavernia, D.W. He, Y.T. Zhu, Appl. Phys. Lett. 83 (2003) 5062.
[149] X.Z. Liao, F. Zhou, E.J. Lavernia, S.G. Srinivasan, M.I. Baskes, D.W. He, Y.T. Zhu, Appl. Phys. Lett. 83 (2003) 632.
[150] M.A. Meyers, O. Vöhringer, V.A. Lubarda, Acta Mater. 49 (2001) 4025.
[151] J. Schäfer, K. Albe, Acta Mater. 60 (2012) 6076.
[152] Z.T. Trautt, A. Adland, A. Karma, Y. Mishin, Acta Mater. 60 (2012) 6528.
[153] C. Brandl, T.C. Germann, A.G. Perez-Bergquist, E.K. Cerreta, Mater. Res. Lett. 1 (2013) 220.
[154] T. Frolov, Appl. Phys. Lett. 104 (2014) 211905.
[155] T. Frolov, D.L. Olmsted, M. Asta, Y. Mishin, Nat. Commun. 4 (2013) 1899.
[156] F.K. Yan, G.Z. Liu, N.R. Tao, K. Lu, Acta Mater. 60 (2012) 1059.
[157] X. Wu, P. Jiang, L. Chen, F. Yuan, Y.T. Zhu, Proc. Natl. Acad. Sci. 111 (2014) 7197.
[158] Y. Wang, M. Chen, F. Zhou, E. Ma, Nature 419 (2002) 912.
[159] T.H. Fang, W.L. Li, N.R. Tao, K. Lu, Science 331 (2011) 1587.
[160] J.B. Jeon, B.-J. Lee, Y.W. Chang, Scr. Mater. 64 (2011) 494.
[161] N. Gunkelmann, E.M. Bringa, K. Kang, G.J. Ackland, C.J. Ruestes, H. M. Urbassek, Phys. Rev. B 86 (2012).
[162] N. Gunkelmann, E.M. Bringa, D.R. Tramontina, C.J. Ruestes, M.J. Suggit, A. Higginbotham, J.S. Wark, H.M. Urbassek, Phys. Rev. B 89 (2014) 140102.
[163] K. Kadau, T. Germann, P. Lomdahl, R. Albers, J. Wark, A. Higginbotham, B. Holian, Phys. Rev. Lett. 98 (2007) 135701.
[164] Z. Pan, Y. Li, Q. Wei, Acta Mater. 56 (2008) 3470.
[165] H. Conrad, High Strength Materials, vol. 436, John Wiley Sons, N.Y., 1964.
[166] Y. Tang, E.M. Bringa, M.A. Meyers, Mater. Sci. Eng. A 580 (2013) 414.
[167] A.M. Guellil, J.B. Adams, J. Mater. Res. 7 (1992) 639.
[168] Z.L. Pan, Y.L. Li, Q.M. Wei, Solid State Phenom. 139 (2008) 83.
[169] Y. Zhang, P.C. Millett, M. Tonks, B. Biner, Scr. Mater. 66 (2012) 117.
[170] D. Tramontina, P. Erhart, T. Germann, J. Hawreliak, A. Higginbotham, N. Park, R. Ravelo, A. Stukowski, M. Suggit, Y. Tang, J. Wark, E. Bringa, High Energy Density Phys. 10 (2014) 9.
[171] S.L. Frederiksen, K.W. Jacobsen, J. Schiøtz, Acta Mater. 52 (2004) 5019.
[172] Y.M. Wang, A.M. Hodge, J. Biener, A.V. Hamza, D.E. Barnes, K. Liu, T.G. Nieh, Appl. Phys. Lett. 86 (2005) 101915.
[173] L. Smith, J.A. Zimmerman, L.M. Hale, D. Farkas, Model. Simul. Mater. Sci. Eng. 22 (2014) 045010.
[174] G.P. Zheng, Y.M. Wang, M. Li, Acta Mater. 53 (2005) 3893.
[175] H.Y. Song, Y.L. Li, J. Appl. Phys. 111 (2012) 044322.
[176] C.J. Ruestes, G. Bertolino, M. Ruda, D. Farkas, E.M. Bringa, Scr. Mater. 71 (2014) 9.
[177] Y.-J. Wang, Grain Growth and Mechanical Properties of Nanocrystalline Mo and Zr Thin Films, National Sun Yat-sen University, 2010.
[178] F.J. Zerilli, R.W. Armstrong, J. Appl. Phys. 61 (1987) 1816.
[179] F.J. Zerilli, R.W. Armstrong, J. Appl. Phys. 68 (1990) 1580.
[180] D.L. Preston, D.L. Tonks, D.C. Wallace, J. Appl. Phys. 93 (2003) 211.
[181] R.W. Armstrong, P.J. Worthington, in: R.W. Rohde, B.M. Butcher, J.R. Holland, C.H. Karnes (Eds.), Metallurgical Effects at High Strain Rates, Springer, US, 1973, pp. 401–414.
[182] J. Swegle, D. Grad, Y. Gupta, in: Y.M. Gupta (Ed.), Shock Waves in Condensed Matter, Plenum, N.Y., 1986.
[183] E. Ma, Y.M. Wang, Q.H. Lu, M.L. Sui, L. Lu, K. Lu, Appl. Phys. Lett. 85 (2004) 4932.
[184] V. Yamakov, D. Wolf, S.R. Phillpot, H. Gleiter, Acta Mater. 50 (2002) 5005.
[185] Y.T. Zhu, X.Z. Liao, X.L. Wu, Prog. Mater. Sci. 57 (2012) 1.
[186] P. Keblinski, D. Wolf, F. Cleri, S. r Phillpot, H. Gleiter, MRS Bull. 23 (1998) 36.
[187] M.J. Demkowicz, A.S. Argon, D. Farkas, M. Frary, Philos. Mag. 87 (2007) 4253.

[188] P. Keblinski, S.R. Phillpot, D. Wolf, H. Gleiter, Acta Mater. 45 (1997) 987.
[189] P.Y. Huang, C.S. Ruiz-Vargas, A.M. van der Zande, W.S. Whitney, M. P. Levendorf, J.W. Kevek, S. Garg, J.S. Alden, C.J. Hustedt, Y. Zhu, J. Park, P. L. McEuen, D.A. Muller, Nature 469 (2011) 389.
[190] K. Kim, Z. Lee, W. Regan, C. Kisielowski, M.F. Crommie, A. Zettl, ACS Nano 5 (2011) 2142.
[191] J. An, E. Voelkl, J.W. Suk, X. Li, C.W. Magnuson, L. Fu, P. Tiemeijer, M. Bischoff, B. Freitag, E. Popova, R.S. Ruoff, ACS Nano 5 (2011) 2433.
[192] C. Lee, X. Wei, J.W. Kysar, J. Hone, Science 321 (2008) 385.
[193] Z. Song, V.I. Artyukhov, B.I. Yakobson, Z. Xu, Nano Lett. 13 (2013) 1829.
[194] Y. Wei, J. Wu, H. Yin, X. Shi, R. Yang, M. Dresselhaus, Nat. Mater. 11 (2012) 759.
[195] R. Grantab, V.B. Shenoy, R.S. Ruoff, Science 330 (2010) 946.
[196] H.I. Rasool, C. Ophus, W.S. Klug, A. Zettl, J.K. Gimzewski, Nat. Commun. 4 (2013).
[197] J.R. Xiao, J. Staniszewski, J.W. Gillespie Jr., Mater. Sci. Eng. A 527 (2010) 715.
[198] J. Zhang, J. Zhao, J. Lu, ACS Nano 6 (2012) 2704.
[199] Y. Li, D. Datta, Z. Li, Carbon 90 (2015) 234.
[200] N.-N. Li, Z.-D. Sha, Q.-X. Pei, Y.-W. Zhang, J. Phys. Chem. C 118 (2014) 13769.
[201] Z.D. Sha, Q.X. Pei, Z.S. Liu, V.B. Shenoy, Y.W. Zhang, Carbon 72 (2014) 200.
[202] Z.D. Sha, S.S. Quek, Q.X. Pei, Z.S. Liu, T.J. Wang, V.B. Shenoy, Y.W. Zhang, Sci. Rep. 4 (2014).
[203] B. Mortazavi, G. Cuniberti, Nanotechnology 25 (2014) 215704.
[204] M.Q. Chen, S.S. Quek, Z.D. Sha, C.H. Chiu, Q.X. Pei, Y.W. Zhang, Carbon 85 (2015) 135.
[205] L. Mishnaevsky Jr., E. Levashov, Comput. Mater. Sci. 96 (2015) 365 , Part A.
[206] H.-H. Fu, D.J. Benson, M.A. Meyers, Acta Mater. 49 (2001) 2567.
[207] E.B. Tadmor, R.E. Miller, Modeling Materials: Continuum, Atomistic and Multiscale Techniques, Cambridge University Press, 2011.
[208] B. Eidel, A. Stukowski, J. Mech. Phys. Solids 57 (2009) 87.
[209] J. Knap, M. Ortiz, J. Mech. Phys. Solids 49 (2001) 1899.
[210] F. Sansoz, J.F. Molinari, Scr. Mater. 50 (2004) 1283.
[211] F. Sansoz, J.F. Molinari, Acta Mater. 53 (2005) 1931.
[212] D.H. Warner, F. Sansoz, J.F. Molinari, Int. J. Plast. 22 (2006) 754.
[213] Y.J. Wei, L. Anand, J. Mech. Phys. Solids 52 (2004) 2587.
[214] J. S. Amelang and D. M. Kochmann, "Surface effects in nanoscale structures investigated by a fully-nonlocal energy-based quasicontinuum method," Mechanics of Materials.
[215] J. S. Amelang, G. N. Venturini, and D. M. Kochmann, "Summation rules for a fully nonlocal energy-based quasicontinuum method," Journal of the Mechanics and Physics of Solids.
[216] J. Schiøtz, F.D. Di Tolla, K.W. Jacobsen, Nature 391 (1998) 561.
[217] Y. Mishin, M.J. Mehl, D.A. Papaconstantopoulos, A.F. Voter, J.D. Kress, Phys. Rev. B 63 (2001) 224106.
[218] Y. Mishin, D. Farkas, M.J. Mehl, D.A. Papaconstantopoulos, Phys. Rev. B 59 (1999) 3393.
[219] G.J. Ackland, G. Tichy, V. Vitek, M.W. Finnis, Philos. Mag. A 56 (1987) 735.
[220] S.M. Foiles, M.I. Baskes, M.S. Daw, Phys. Rev. B 33 (1986) 7983.
[221] J.A. Moriarty, Phys. Rev. B 16 (1977) 2537.
[222] J.A. Moriarty, Phys. Rev. B 26 (1982) 1754.
[223] J.A. Moriarty, Phys. Rev. B 38 (1988) 3199.
[224] J.A. Moriarty, L.X. Benedict, J.N. Glosli, R.Q. Hood, D.A. Orlikowski, M.V. Patel, P. Söderlind, F.H. Streitz, M. Tang, L.H. Yang, J. Mater. Res. 21 (2006) 563.
[225] A. Strachan, T. Çağin, O. Gülseren, S. Mukherjee, R.E. Cohen, W.A. GoddardIII, Model. Simul. Mater. Sci. Eng. 12 (2004) S445.
[226] G.J. Ackland, R. Thetford, Philos. Mag. A 56 (1987) 15.
[227] H. Park, M.R. Fellinger, T.J. Lenosky, W.W. Tipton, D.R. Trinkle, S.P. Rudin, C. Woodward, J.W. Wilkins, R.G. Hennig, Phys. Rev. B 85 (2012) 214121.
[228] M.R. Fellinger, H. Park, J.W. Wilkins, Phys. Rev. B 81 (2010) 144119.
[229] J. Wang, Y.L. Zhou, M. Li, Q. Hou, Model. Simul. Mater. Sci. Eng. 22 (2014) 015004.
[230] D.Y. Sun, M.I. Mendelev, C.A. Becker, K. Kudin, T. Haxhimali, M. Asta, J.J. Hoyt, A. Karma, D.J. Srolovitz, Phys. Rev. B 73 (2006) 024116.
[231] G.J. Ackland, Philos. Mag. A 66 (1992) 917.
[232] R.R. Zope, Y. Mishin, Phys. Rev. B 68 (2003) 024102.
[233] R.G. Hennig, T.J. Lenosky, D.R. Trinkle, S.P. Rudin, J.W. Wilkins, Phys. Rev. B 78 (2008) 054121.
[234] Y.-M. Kim, B.-J. Lee, Acta Mater. 56 (2008) 3481.
[235] F.H. Stillinger, T.A. Weber, Phys. Rev. B 31 (1985) 5262.
[236] J. Tersoff, Phys. Rev. B 38 (1988) 9902.
[237] J. Tersoff, Phys. Rev. B 39 (1989) 5566.
[238] T. Kumagai, S. Izumi, S. Hara, S. Sakai, Comput. Mater. Sci. 39 (2007) 457.
[239] P. Erhart, K. Albe, Phys. Rev. B 71 (2005) 035211.
[240] M.Z. Bazant, E. Kaxiras, J.F. Justo, Phys. Rev. B 56 (1997) 8542.
[241] D. Sen, A. Cohen, A.P. Thompson, A. Van Duin, W.A. GoddardIII, M.J. Buehler, in: Symposium on KKLLNNOOPP – Integr. Miniaturized Mater.- Self-Assem. Device Integr., 2010.
[242] B. Jelinek, S. Groh, M.F. Horstemeyer, J. Houze, S.G. Kim, G.J. Wagner, A. Moitra, M.I. Baskes, Phys. Rev. B 85 (2012) 245102.
[243] K. Chenoweth, A.C.T. van Duin, W.A. Goddard, J. Phys. Chem. A 112 (2008) 1040.
[244] D.W. Brenner, O.A. Shenderova, J.A. Harrison, S.J. Stuart, B. Ni, S.B. Sinnott, J. Phys. Condens. Matter 14 (2002) 783.
[245] S.J. Stuart, A.B. Tutein, J.A. Harrison, J. Chem. Phys. 112 (2000) 6472.
[246] A.V. Sergueeva, V.V. Stolyarov, R.Z. Valiev, A.K. Mukherjee, Scr. Mater. 45 (2001) 747.
[247] J. Narayan, C.C. Koch, X. Zhang, R. Venkatesan, n.d. (Unpublished Work).
[248] H. Conrad, J. Narayan, Mech. Prop. Nanocryst. Mater. (2011) 1.
[249] H. Gleiter, Acta Mater. 48 (2000) 1.
[250] H. Van Swygenhoven, D. Farkas, A. Caro, Phys. Rev. B 62 (2000) 831.
[251] B.A. Bilby, A.R. Entwisle, Acta Metall. 4 (1956) 257.
[252] J.E. Hammerberg, 2015 (Private Communication).
[253] T.C. Germann, 2014 (Private Communication).
[254] T. Frolov, K.A. Darling, L.J. Kecskes, Y. Mishin, Acta Mater. 60 (2012) 2158.
[255] S. Traiviratana, A Molecular Dynamics Study of Void Initiation and Growth in Monocrystalline and Nanocrystalline Copper, 2008.
[256] Y. Mishin, M. Asta, J. Li, Acta Mater. 58 (2010) 1117.
[257] K.S. Kumar, H. Van Swygenhoven, S. Suresh, Acta Mater. 51 (2003) 5743.
[258] S. Washko, G. Aggen, ASM Int. Met. Handb. Tenth Ed. 1 (1990) 841.
[259] J. Truman, in: F.B. Pick. (Ed.), Mater. Sci. Technol., 7, 1993, p. 527.
[260] X.H. Chen, J. Lu, L. Lu, K. Lu, Scr. Mater. 52 (2005) 1039.
[261] İ. Üçok, T. Ando, N.J. Grant, in: H.F. SAVAGE (Ed.), Rapidly Quenched Mater, Elsevier, Oxford, 1991, pp. 284–287.
[262] M. Eskandari, A. Najafizadeh, A. Kermanpur, Mater. Sci. Eng. A 519 (2009) 46.
[263] E.M. Bringa, S. Traiviratana, M.A. Meyers, Acta Mater. 58 (2010) 4458.
[264] Y.M. Wang, E.M. Bringa, J.M. McNaney, M. Victoria, A. Caro, A.M. Hodge, R. Smith, B. Torralva, B.A. Remington, C.A. Schuh, H. Jamarkani, M.A. Meyers, Appl. Phys. Lett. 88 (2006) 061917.
[265] C.H. Lu, B.A. Remington, B.R. Maddox, B. Kad, H.S. Park, M. Kawasaki, T. G. Langdon, M.A. Meyers, Acta Mater. 61 (2013) 7767.
[266] C.H. Lu, B.A. Remington, B.R. Maddox, B. Kad, H.S. Park, S.T. Prisbrey, M. A. Meyers, Acta Mater. 60 (2012) 6601.
[267] Y.T. Zhu, X. Liao, Nat Mater 3 (2004) 351.
[268] C. Koch, Scripta Materialia 49 (2003) 657.
[269] K. Lu, Science 345 (2014) 1455.

Marc André Meyers, Distinguished Professor of Nanoengineering, and Mechanical and Aerospace Engineering, University of California, San Diego, has published thirty-five papers in Materials Science and Engineering A (and its predecessor MSE) and was Associate Editor for Brazil (1976-1980); currently, he is on the Editorial Board. His research in mechanical behavior of materials has focused on dynamic behavior of materials; nanocrystalline materials; and biological materials. He has authored/co-authored four books (Mechanical Metallurgy; with K, K. Chawla, Dynamic Behavior of Materials, Mechanical Behavior of Materials, with K. K. Chawla, Biological and Bioinspired Materials, with P. Y. Chen, and ~ 400 papers (10,000 citations and ISI 51 H-index). He has held visiting professorships at University of Karlsruhe (Institute of Technology), University of Metz, and Cambridge University (Life Member, Clare Hall) and Chinese Academy of Sciences. He is Fellow of TMS, APS, and ASM International and recipient of 2010 Acta Materialia Materials and Society Award; Humboldt Society Senior Scientist Award; J. S. Rinehart Award from EURODYMAT Association; Lee Hsun Lecture Award from Institute of Metals Research in China; SMD/TMS Distinguished Scientist and Distinguished Service Awards; ASM International Albert Sauveur and Albert White Awards; JOM/TMS 2010 best paper award (co-recipient) in structural materials and 2012 TMS Educator Award; 2015 Morris Cohen Award; 2014 Heyn Medal, DGM.